

**Pump induced tilt and pore pressure variations at  
Fuhrberg, north of Hanover  
and their modeling in layered half space**

**Von der Naturwissenschaftlichen Fakultät  
der Gottfried Wilhelm Leibniz Universität Hannover  
zur Erlangung des Grades einer  
DOKTORIN DER NATURWISSENSCHAFTEN**

**Dr. rer. nat.  
genehmigte Dissertation**

**von**

**M. Sc. Hsiao-Chih Chen  
geboren am 31. 12. 1978 in Taipei**

2008

Referent: Prof. Dr. Hans-Joachim Kümpel

Korreferentin: Prof. Dr. Jutta Winsemann

Tag der Promotion: 12. 12. 2008

## Abstract

Large amounts of ground water withdrawn by pump wells can cause considerable ground deformation. In practice, the mechanism and behavior of the ground movements are interpreted by the poroelasticity theory. Long-term monitoring of such processes yields observations that can be used to estimate subsequent changes in pore pressure gradients and tilt movement responses.

A groundwater production facility at Fuhrberger Feld, north of the city of Hanover, Lower Saxony has a relatively complicated structure. It has two pumps in a central pit connected to an asterisk arrangement of eight horizontal wells. The horizontal wells are composed of two parts: screen sections (outwards) and transport sections (inwards). Sufficient rainfall is obtained in this forest region. The underlying ground formations present a rather uniform lithology. A mostly steady and unconfined aquifer is maintained in sandy layer. This study deals with the function of the central pit and the screen sections of the horizontal wells. In particular, to what extent do they contribute to ground deformations induced by pumping? Therefore, 12 tiltmeters and 5 pressure transducers were installed to monitor the vertical ground inclinations and variations of water table, respectively.

The azimuths of the responding tilt signals to forcing pump sources generally deviate by some  $10^\circ$  and in some cases by more than  $20^\circ$ . The average amplitude ranges from 0.33 to 0.5  $\mu\text{rad}$  in response to a change in pumping rate of  $100 \text{ m}^3/\text{h}$ . The pump induced tilt signals basically point towards the central pit, approximately parallel to the orientation of the horizontal wells. Decreasing azimuths and amplitudes are associated with an increasing radial distance to the central pit or screen section. The pump induced pore pressure gradients build up in a concentric flow system as observed by water table monitoring.

Possible existence of inhomogeneities in the sediments at near-surface is observed in the tilt results. Additional geophysical measurements, pump tests of individual screen sections and numerical analysis supported this conclusion. Four models were constructed to distinguish the forcing sources between the central pit and the screen sections. The continuous points model is a suitable representation of the in-situ conditions

Keywords: Ground deformation; Tiltmeter; Poroelasticity

## Kurzfassung

Die dem Grundwasser durch Förderbrunnen entzogenen, häufig großen Wassermengen können erhebliche Boden-Deformationen verursachen. Der Mechanismus und das Verhalten der Bodenbewegung können mit Hilfe der Poroelastizitäts-Theorie beschrieben werden. Die durch Langzeitüberwachung, etwa mittels oberflächennaher Neigungsmesser gewonnenen Beobachtungen eines solchen Prozesses erlauben bei Kenntnis der verursachenden Porendruckgradienten Rückschlüsse auf das poroelastische Verformungsverhalten des Untergrundes und bei Abweichungen von der Modellsituation auf lokale Heterogenitäten im Untergrund.

Einer der Hauptversorgungsbrunnen des Wasserwerks Hannover (Niedersachsen), ungefähr 30 km nordwestlich der Stadt im Fuhrberger Feld, besitzt eine relativ komplexe Struktur:

Zwei Pumpen sind in einem vertikalen Brunnenschacht installiert, von dem in 25 m Tiefe acht horizontale Filterstränge sternförmig abgehen. Die Filterstränge sind untergliedert in einen Vollrohrbereich direkt am Schacht (innen) und einen Filterbereich (außen). Das Gebiet wird ausreichend mit Regenwasser versorgt. Die Untergrundformationen bestehen im Wesentlichen aus Sanden über Ton. Dadurch ist ein weitestgehend beständiger Grundwasserhorizont in einem ungespannten, sandigen Aquifer gegeben.

Die im Rahmen dieser Arbeit durchgeführten Untersuchungen beschäftigen sich mit den Auswirkungen dieses Horizontalbohrbrunnens im zentralen Bereich und an den einzelnen Filterstrecken. Die konkrete Fragestellung ist dabei, in welchem Maße dessen Wasserförderung zu Bodendeformationen beiträgt. Um die Verformung des Untergrundes in Zusammenhang mit der Grundwasserspiegeländerung erfassen zu können, wurden auf dem Gebiet 12 Neigungssensoren und 5 Wasserstandssensoren installiert. Die minutenweise über mehrere Jahre aufgezeichneten Messwerte, ergänzt durch die vom Wasserwerk halbstündig zusammengefassten Pumpraten, lieferten eine brauchbare Datenbasis.

Die durch das Pumpen verursachten Signale der Neigungssensoren weisen grundsätzlich zum Zentrum der Brunnenanordnung, annähernd parallel zu den einzelnen Filtersträngen. Die aus den Neigungsmesswerten ermittelte Abweichung des Azimuts im Vergleich zu der Richtung der einwirkenden Quelle ist meistens kleiner als  $10^\circ$ , in einigen Fällen überschreitet sie  $20^\circ$ . Die durchschnittlichen Neigungswerte liegen bei einer Veränderung der Pumprate um  $100\text{m}^3/\text{h}$  zwischen  $0,33$  und  $0,5$   $\mu\text{rad}$ . Mit zunehmender radialer Entfernung zum Zentralschacht verringern sich die Azimutabweichungen und Neigungsamplituden. Das Gleiche gilt für die Distanz senkrecht zu den Filtersträngen.

Vier numerische Modellkonfigurationen wurden entwickelt, um die Einflüsse der Filterstränge und des Zentralschachtes zu unterscheiden. Das „kontinuierliche Punkt-Modell“ liefert eine passende quantitative Darstellung der in-situ-Bedingungen. Die Verteilung der Porendruckgradienten kann auf Grund der Wasserspiegelmessungen in einem konzentrischen Fließ-System dargestellt werden. Die Neigungsergebnisse weisen zudem auf die mögliche Existenz von Inhomogenitäten in den oberflächennahen Sedimenten hin. Zusätzliche geophysikalische Messungen, Pumptests an einzelnen Filtersträngen und numerische Analysen unterstützen diese Schlussfolgerung.

Stichwörter: Boden-Deformationen; Neigungsmesser; Poroelastizität

<b><u>TABLE OF CONTENTS</u></b>		<b><u>Page</u></b>
	Abstract	i
	Table of Contents	iii
	List of Figures	v
	List of Tables	vii
	Abbreviations	viii
<b>1</b>	<b>Introduction</b>	1
<b>2</b>	<b>Fundamentals</b>	4
2.1	Geology and hydrology	4
2.2	Poroelasticity	6
2.3	Instruments	9
	2.3.1 Tiltmeter	10
	2.3.2 Pressure transducer	14
<b>3</b>	<b>Observations</b>	17
3.1	Geometric distribution	17
3.2	Tiltmeter campaign	18
3.3	Water table measurement	22
3.4	Other geophysical surveys	25
	3.4.1 Seismics method	26
	3.4.2 DC Resistivity method	29
	3.4.3 GPR method	32
<b>4</b>	<b>Data processing</b>	34
4.1	Tilt signal	34
4.2	Water table variation	41
4.3	Pump event	46
<b>5</b>	<b>Model calculation</b>	56
5.1	Parameters	56

5.2	Central source models	62
5.2.1	Single point source	62
5.2.2	Wide single source	65
5.2.3	Depth-redial distance comparison	67
5.3	Peripheral source models	70
5.3.1	Disk-like source	71
5.3.2	Continuous points source	73
5.3.3	Comparison of screen section and boundary area	77
<b>6</b>	<b>Discussion</b>	<b>81</b>
6.1	In-situ measurements evaluation	81
6.1.1	Instrumental effects	81
6.1.2	Vegetation effects	84
6.1.3	Topographic effects	85
6.2	Model evaluation and application	87
6.2.1	Validation of modeling results	87
6.2.2	Additional pump test of individual screen sections	89
<b>7</b>	<b>Conclusion</b>	<b>93</b>
	<b>Bibliography</b>	<b>96</b>
	<b>Appendices</b>	<b>105</b>
	Appendix A: Events from monitoring schedule	105
	Appendix B: GPS coordinates of locations	108
	Appendix C: Additional P-wave seismic survey	111
	Appendix D: General migrating signals and hodograms at locations along the NE flank	112
	Appendix E: Water table level after April 2008	113
	Appendix F: When the central pit is not considered for model (d)	115

<b><u>LIST OF FIGURES</u></b>		<b><u>Page</u></b>
2.1	The geological map of the research area	5
2.2	Selected borehole data from the surroundings of the research area	5
2.3	Sketches of the sensors from different types of tiltmeters	11
2.4	The installation of the tiltmeter and its data recording system	12
2.5	The sketch of the measuring concept and illustrated vectors of tilt motion	13
2.6	The installation of a pressure transducer for water table measurements	15
3.1	The well location and the profile of the central pit	18
3.2	Locations of all monitoring positions of tiltmeters	19
3.3	Comparison between different factors with influence on tilt signals	22
3.4	Results and refinement of water table measurements	24
3.5	Elevation display along the profile for additional geophysical measurements	25
3.6	Results of additional geophysical surveys along A-A' transect	28
3.7	The result of DC resistivity on B-B' transect	31
4.1	Monthly general migration signals in different seasons	35
4.2	Long-term variations of general migration signals	37
4.3	General migration signals with and without the temperature effect at F4	38
4.4	Hodograms of general migration signals	40
4.5	Variations in the water table height of the 5 monitoring observation wells	43
4.6	Water table variations compared with the pump rate in different seasons	44
4.7	Variations of general drawdown situations in different seasons	46
4.8	A selected example of tilt signals at location F9 induced by a pump event	48
4.9	Tilt azimuths and amplitudes induced by pump events	50
4.10	Tiltmetr arrays and their corresponding signal distribution	51
4.11	The water table changes induced by pump rate changes	53
5.1	Four types of pump source	58
5.2	The analyzed vectors along the screen section and along the boundary area	60
5.3	Simulated results of pump induced changes for single point source	64
5.4	Simulated results of pump induced changes for wide single source	66
5.5	Analyses of pore pressure and radial tilt variations for models (a) and (b) at 4 selected depths	68
5.6	Simulated results of pump induced changes for disk-like source	72
5.7	Simulated results of pump induced changes for continuous points source on the screen section	74
5.8	Simulated results of pump induced changes for continuous points source on the boundary area	75
5.9	Integrated results from the screen section and the boundary area in 2-D and 3-D illustration	79
6.1	The tilt signals of the instrument interchanges in X-axis at F8, F9, F12, F13	82
6.2	Amplitude differences due to interchanging of instruments	83
6.3	The distribution of surrounding trees for the tiltmetes along the W flank	84
6.4	Comparison between the topography and tilt results.	86
6.5	Without the central pit influence, the simulated results in models (c) and (d)	89
6.6	Pump test results of P1 to P8	90
6.7	The monitoring results at the NE flank after reactivation of regular pumping	92

C.1	The seismogram of P-wave reflection survey	112
D.1	The general migrating tilt signals (X-, Y-axis and instrument temperature) at F1, F6, F24, and F34-F42	113
D.2	The tilt hodograms for locations F1, F6, F24, and F34-F42	114
E.1	Changes in water table level from 5 observation wells for period 1 April till 13 August 2008	114
F.1	Computational results of (a) pore pressure and (b) tilt from the screen sections and boundary area (at depth $z = 10$ m and 3600 s after onset of pumping) on X-Y and X-Z planes without considering the influence of the central pit	115



<b><u>LIST OF TABLES</u></b>		<b><u>Page</u></b>
2.1	The tiltmeter standards for different types and their adjustment parameters	13
3.1	Positions, instrumental types and monitoring durations for tiltmeter array	20
3.2	Parameters of five observation wells	23
3.3	Specific parameters for shear wave reflection survey	27
3.4	Processing flow for seismic data	27
3.5	Resistivities of selected common geologic materials	31
3.6	Specific parameters for GPR measurement	32
4.1	The optimal temperature factor for each location	39
4.2	Total amounts of pumping events at different monitoring locations	47
5.1	The formation parameters for modeling	57
5.2	The settings for 4 types of forcing source	59
5.3	Comparison of max. tilt between the two formations of models (a) and (b)	67
5.4	The increments of contours for all times and depths in Fig 5.9	79
5.5	Maximum tilt values in two formations of models (c) and (d)	80
6.1	Distributions of trees and their distances to nearby tiltmeter locations	84
A.1	Events related to instrument adjustments and other operations within the monitoring schedule	105
B.1	Tiltmeter locations along 4 screen sections and observation wells	108
B.2	Coordinates of profile points along transects A-A' and B-B' of additional geophysical surveys	109
C.1	Specific parameters for P-wave reflection survey	111
C.2	Processing flow for P-wave data	112

**ABBREVIATIONS**

An	AGI model of tiltmeter (n = 1, 2)
ASL	Above Sea Level
B	Skempton ratio
°	degree(s)
°C	degree Celsius
d	day(s)
D	hydraulic diffusivity
DC	direct current
E	East
EG	electric contact gauge
EQ	earthquake
Fn	tiltmeter location in Fuhrberg (n = 1 - 42)
Gn	GGA model of tiltmeter (n = 1, 2, 3, 4)
GPa	Giga-Pascal(s)
GPR	Ground Penetrating Radar
GPS	Global Positioning System
h	hour(s)
Hz	hertz(s)
kg	kilogram(s)
Ln	Lippmann model of tiltmeter (n = 1, 3, 4, 5, 6, 8)
m	meter(s)
$\mu$	shear modulus
$\mu\text{rad}$	micro-rad(s)
M	magnitude
ns	nanosecond(s)
N	North
P	pore pressure
PV <sub>n</sub>	pump head (n = 1, 2)
PR	pump rate
S	South
T	temperature
Tr	induced tilt
TT	temperature of tiltmeter
TX	X-axis of tiltmeter
TY	Y-axis of tiltmeter
$\nu$	Poisson's ratio
V	volt(s)
W	West
W <sub>n</sub>	observation well number (n = 1 - 5)
WT	water table
Z	depth

# Chapter 1

## Introduction

This research is conducted at Fuhrberg area, north of Hanover, Germany. The neighborhood is covered with forests and receives ample rainfall. A relatively steady aquifer is maintained so that withdrawal of large amounts of groundwater is feasible. To optimize the efficiency of water collection, a radial collector well was built in 1960s. The well consists of a central pit connected to eight horizontal arms in a radial form. Several studies have focused on the hydraulic flow analysis: linear flow estimation, multilayer simulations and productions associated with similar type of horizontal wells (Boettcher et al., 1985; Ball and Herbert, 1992; Bakker et al., 2005; Kawecki and Al-Subaikhy, 2005). Other studies using single vertical wells indicate that a symmetric subsidence or uplift of ground deformation may occur due to the variation of pore pressure gradients induced by water withdrawing (Holzhausen et al., 1980; Vasco et al., 2002). However, so far no study has focused on the near-surface movements caused by the influences of such horizontal well. This study aims to address this question.

Unlike previous studies, the most novel aspect of this research concerns the examination of the influences from both the central pit and its horizontal arms. These are then used to determine the dominant mechanisms and factors contributing to ground deformation. Further, the form and progress of the movements are also illustrated (Kümpel, 1982). From the pump activities and monitoring data derived from this research, more local hydraulic and subsurface parameters can be identified. Consequently, better strategies can be formulated for related research in future. The data derived can even provide useful information for further improvement of the pump construction and appropriate urban planning for better land use (Herbert and Ball, 1992; Pesti et al., 1994). Moreover, an analytic solution is applied to validate if mathematical modeling can be used to simulate realistic conditions. This is especially beneficial when field measurements are not easy or impossible to perform.

Poroelasticity theory describes the mechanism and response of ground deformation induced pore pressure changes e.g. by pump operations from the wells in the vicinity. This theory has been substantiated by many reported studies, under

saturated conditions. The variations in ground tilt may correspond to the changes in pore pressure gradients. The variables of the deformation can be revealed through decomposing its components from lateral and vertical displacements (Kümpel et al., 1996; Karasaki et al., 2000). By applying numerical methods with in-situ boundary conditions, the chronological and spatial developments of pore pressure and tilt can be reasonably estimated. The assessments for the deformed quantity and the varying process can be done in a relatively practical way (Harrison, 1976b; Evans and Holzhausen, 1983; Fabian and Kümpel, 2003).

Tiltmeters are extensively applied on the measurements of induced poroelastic deformation, although diverse types of instruments are likewise capable of doing so. Their advantages lie in their high sensitivity and accuracy (up to a nano-radian range of resolution) attainable for measuring tilt deformation (Mentes, 2004; d'Oreye and Zürn, 2005). The stability of the instrument is highly reliable such that sudden pump injections do not disturb its ability to constantly monitor (Evans, 1983). The versatility of tiltmeters allow them to be applied in many other fields, such as in oceanography, engineering, or seismology where they are used to monitor thermoelasticity, earth tide, precipitation cause in hydraulic flow, or micro seismicity due to external forces in the surroundings (Gazonas et al., 1988; Okada, 1992; Kümpel et al., 1998; Kümpel and Fabian, 2003; Lecampion et al., 2005; Roeloffs, 2006; Takemoto et al., 2006; Fabian and Villinger, 2007).

Some prerequisites must be met regarding the installation to obtain the best signal-to-noise ratio for data recording. To minimize influences from local topography and vegetation obstruction, a relatively flat and spacious surface or a borehole position are the generally preferred arrangements for the tiltmeter installation (Harrison, 1976a; Kümpel, 2001). Consequently the tiltmeters employed in this study are positioned in boreholes. They are allocated along horizontal arms of the well, to continuously monitor the variation of hydraulic flow and its induced ground deformation.

More knowledge concerning the research backgrounds, such as the regional geology, the governing concept of the poroelasticity theory and the numerical modeling and the applications of the available instruments are described in Chapter 2.

Chapter 3 illustrates the central pit and its eight horizontal wells, the configurations of instruments, some observed characteristic signals in the primary recordings, and application of three other types of geophysical measurements to assist finding subsurface structures.

Chapter 4 shows the chronological recordings for the tilt and hydraulic variations, and the specific results of pump induced signals, which can be compared with the computed results through numerical analysis in Chapter 5. Different types of well sources are hypothesized to match a realistic best-fit solution. The differences between the real monitoring situation and the analytic estimation are seen.

Chapter 6 discusses the possible causes or reasonable doubts for the variation of pore pressure gradients, the mechanism of the ground deformation, and some dominating factors of anomalous situations. Chapter 7 concludes a general frame of the studied process, varying quantities and expectable solutions for the near-surface movements induced by a collector well with horizontal arms.

## **Chapter 2**

# **Fundamentals**

This chapter contains some background knowledge relevant to this research. It includes the regional geology and hydrology to illustrate the sedimentary environment, the theoretical basis of poroelasticity, and basic facts about the instruments applied in the study.

### **2.1 Geology and hydrology**

The research area is located near Lindwedel, 30 km to the north of Hanover, belonging to the territory of Fuhrberg waterworks. It is classified as Aller lowland area. The river Aller runs through its northern region and is confluent with its tributary Wietze in the East (Lang, 1981). The glacial and fluvioglacial sediments are deposited during the late Quaternary. The sediments consist mainly of gravel, sand, and till; their thickness varies from 30 m to 80 m. The region is rather flat. Figure 2.1 shows the predominately sand with some remnants of sand-drifting dunes existing in its superficial layer.

The land is widely used for growing widespread coniferous forest. The annual rainfall is about 630 mm and the elevation of the water table is generally around 30 m above sea level (Rai and Hoffmann, 1989; Van Berk and Hansen, 2006). The aquifer is unconfined and in a relatively steady condition. It provides sufficient amount of water that can be drawn for use.

Some neighboring borehole data from LBEG (Landesamt für Bergbau, Energie und Geologie - Local Geological Survey) Database System is known that the near-surface formations are mostly formed of sandy materials with various grain sizes (Fig. 2.2). The overall thickness of the sand formation observed in the boreholes differs from 35 m to 70 m. It is intersected by several thin layers, less than 10 m of gravel, silt or till formations, and some organic deposits. Locally massive gravel layers are observed (boreholes C). Some deep boreholes reach Pre-Quaternary soft rock, such as gypsum or compacted clay in the basement (boreholes A, B and D). No significant inclinations of layers or intense tectonic structures and movements are evident in the Quaternary sediments in this area.

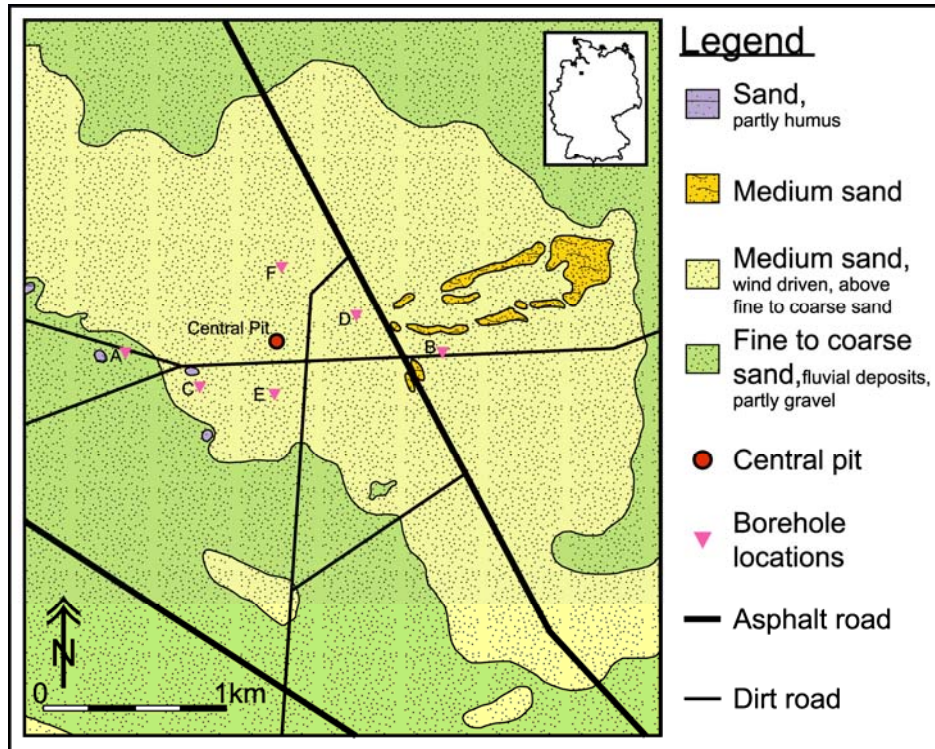


Fig. 2.1 The geological map of the research area.

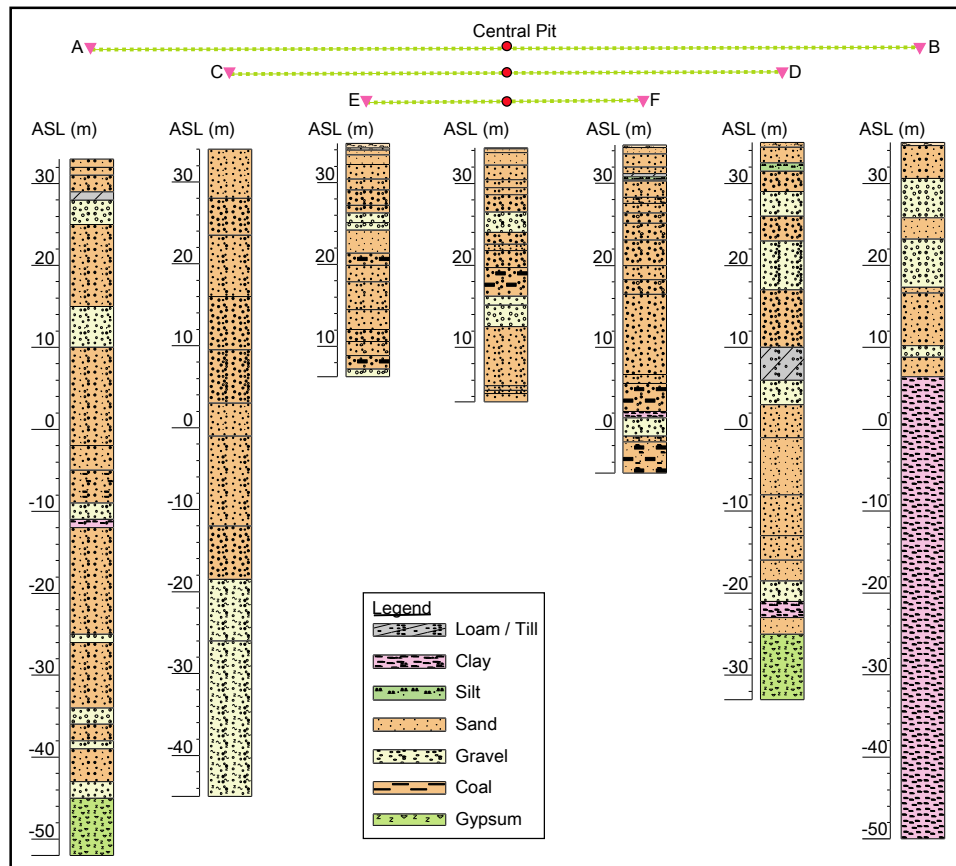


Fig. 2.2 Selected borehole data from the surroundings of the research area. Locations are shown in Fig. 2.1.

## 2.2 Poroelasticity

Since porosity exists in all natural rocks, poroelasticity is a proper term to describe the coupling behavior between the solid (as rock matrix strain) and fluid (as pore pressure) phases involved in a stress-strain relationship. Poroelastic behavior was observed in several situations, mostly related to water table variations responding to the ocean tides, passing trains or pumping wells nearby, or microseism caused by lakes (Wang, 2000). The theory basically established after Terzaghi's and Biot's theory and its object performance combines the concept of the elastic deformation in Hook's linear law and the fluid flow through a permeable media described by Darcy's law (Kümpel, 2004).

Considering the deformation in the matrix, the associated poroelastic constants, such as bulk modulus ( $K'$ ), Poisson's ratio ( $\nu'$ ), and shear modulus ( $\mu'$ ), are mostly considered in two conditions: drained (as pore fluid pressure remains constant) and undrained (as pore fluid volume remains constant). However, the shear modulus has the same value in both conditions (Kümpel, 1991). Through drained compressibility ( $c$ ), the amount of deformation of a fractional volume change due to pressure change is defined (eq. 2.1), where  $P_c$  denotes the confining pressure.

$$c = -\frac{1}{V} \left( \frac{\partial V}{\partial P_c} \right)_{\delta P=0} = \frac{1}{K} \quad (\text{eq. 2.1})$$

Four types of compressibility can in fact be defined: drained/matrix compressibility ( $c$ ), undrained compressibility ( $c_u$ ), grain/solid compressibility ( $c_s$ ), and fluid compressibility ( $c_f$ ) present the different solutions for possible relations between the matrix and the fluid.

For saturated porous materials, two specific parameters: Skempton ratio ( $B$ ) and coefficient of effective pressure ( $\alpha$ ) are defined in eq. 2.2 and eq. 2.3 (Skempton, 1954). The Skempton ratio ( $B$ ) is used to illustrate the proportion of changes between the skeletal framework and the fluid while a stress is applied. It is the ratio of the induced pore pressure due to a change in confining pressure (as applied stress) under undrained conditions. Its value varies between zero and one ( $0 < B < 1$ ) representing gas-filled pores and saturated soils, respectively.



$$B = \left( \frac{\partial P}{\partial P_c} \right)_{\delta m=0} \quad (\text{eq. 2.2})$$

$$\delta P_e = \delta P_c - \alpha \delta P \quad (\text{eq. 2.3})$$

The coefficient of effective pressure ( $\alpha$ ) is the fraction of pore pressure when an effective pressure ( $P_e$ ) is considered, showing the ratio of pore volume changes to the bulk volume. Values of  $\alpha$  also lie between zero and one ( $0 < \alpha < 1$ ) such that if the matrix compressibility is much larger than the grain compressibility (as for loose materials),  $\alpha$  is close to one. Alternatively, when the compressibilities of both the matrix and grain are similar,  $\alpha$  is close to zero (as for hard materials). The relationship between the Skempton ratio and the coefficient of effective pressure is shown in eq. 2.4 where  $\nu$  and  $\nu_u$  denote drained and undrained Poisson's ratios, respectively (Rice, 1976).

$$B = \frac{3(\nu_u - \nu)}{\alpha(1 - 2\nu)(1 + \nu_u)} \quad (\text{eq. 2.4})$$

Additionally, variations of fluid flow within the pore space may also be considered. Since coupling behavior exists between the matrix and the pore pressure gradient, the deformation in a permeable material associated with fluid flow can not be ignored. Hydraulic diffusivity ( $D$ ) is the parameter used to describe the coupling situation and includes the Poisson's ratios ( $\nu$ ,  $\nu_u$ ), Darcy conductivity ( $\kappa$ ), shear modulus ( $\mu$ ) and Skempton ratio ( $B$ ). It has a unit of  $\text{m}^2/\text{s}$  (eq. 2.5).

$$D = \frac{2(1 - \nu)(1 + \nu_u^2)}{9(1 - \nu_u)(\nu_u - \nu)} \kappa \mu B^2 \quad (\text{eq. 2.5})$$

Above all, to address the linear poroelastic problem, both the equations of the mechanical equilibrium and the fluid continuity have to be included, with consideration to the variables of stress components, displacement components, pore pressure and increment of fluid content in poroelasticity. Equilibrium, isotropic, homogeneous and saturated situations are set for initial and boundary conditions. The concise governing equations can be expressed as follows (Wang, 2000):

$$\mu \nabla^2 u_i + \frac{\mu}{1 - 2\nu} \frac{\partial \varepsilon}{\partial x_i} = \alpha \frac{\partial P}{\partial x_i} - F_i \quad (\text{eq. 2.6})$$

$$\alpha \frac{\partial \varepsilon}{\partial t} + S_\varepsilon \frac{\partial P}{\partial t} = \kappa \nabla^2 P + Q$$

, where  $\nabla^2 = \frac{\partial^2}{\partial x_1^2} + \frac{\partial^2}{\partial x_2^2} + \frac{\partial^2}{\partial x_3^2}$  ,  $\varepsilon = \varepsilon_{11} + \varepsilon_{22} + \varepsilon_{33}$

, and  $S_\varepsilon = \frac{\alpha^2(1-2\nu_u)(1-2\nu)}{2\mu(\nu_u - \nu)}$

The first part of eq. 2.6 describes the elastic behavior, with additional consideration to the fluid pressure gradient and body force F. The second part of the equation illustrates that the equilibrium is achieved per time unit change of the volumetric strain, fluid source and fluid pressure gradient. It indicates the coupling behavior between the pore pressure and the volumetric strain, i.e. a diffusion equation for pore pressure.

The notation of  $u_i$  stands for the displacements in the x, y, and z directions, respectively;  $\varepsilon$  for volumetric strain;  $F_i$  for volume unit of body force applied on the matrix in 3 components (N/m<sup>3</sup>);  $S_\varepsilon$  for specific storage coefficient; Q for fluid source (m<sup>3</sup>/s), respectively.

The governing equations are suitable for the quasi static status. Additional literature discussing the conditions of anisotropy, nonlinearity, inelasticity, dynamicity, thermoelasticity is reviewed in Kümpel (1991). Through in-situ measurements of tiltmeters and pressure transducers, the parameters  $\partial u_1/\partial x_3$ ,  $\partial u_2/\partial x_3$ , and P are obtained.  $F_i$  is assumed to be zero, and Q can be derived from the actual pumping quantity, thus the equations are validated.

The steady state solutions for the poroelastic equations is provided in eq. 2.7, which is proven by the recordings at profound depths through pump tests from deep production wells (Kümpel, 1989). So in a full-space, the solutions for the induced vertical radial tilt ( $\Delta\gamma_r$ ) and pore pressure (P) are as following:

$$\Delta r_r = \frac{q_0(1+\nu_u)B}{24\pi(1-\nu_u)D} \frac{r(z-d)}{\sqrt{(z-d)^2 + r^2}^3} \quad (\text{eq. 2.7})$$

$$P = \frac{q_0}{4\pi\kappa} \frac{1}{\sqrt{(z-d)^2 + r^2}}$$

For annotations: the pump rate is  $q_0$  (m<sup>3</sup>/h), the radial distance from the well is r, the depth of a chosen horizontal plane is z, and its vertical distance to the well is (z-d). The display of the tilt solution forms a symmetric mirror image along the plane of the

well screen, and a rotational symmetry away from the well center; instead, the pore pressure performs a spherical symmetry away from the well center. However, the effect of a free surface has to be considered when a near-surface measurement is performed. With the method of mirror loading solution and its adjusted factor from free surface movements, the steady state solutions for a homogeneous half-space condition are as given in eq. 2.8 (Lehmann, 2001; Wang and Kümpel, 2003).

$$\Delta r_r = \frac{q_0(1+\nu_u)B}{24\pi(1-\nu_u)D} r \left( \frac{(z-d)}{\sqrt{(z-d)^2+r^2}^3} - \frac{z+(4\nu-5)d}{\sqrt{(z+d)^2+r^2}^3} - \frac{6dz(z+d)}{\sqrt{(z+d)^2+r^2}^5} \right) \quad (\text{eq. 2.8})$$

$$P = \frac{q_0}{4\pi\kappa} \left( \frac{1}{\sqrt{(z-d)^2+r^2}} - \frac{1}{\sqrt{(z+d)^2+r^2}} \right)$$

The estimations for the tilt and pore pressure variations at shallow depths are possible. The maximum deformed locations are proportional to the well depth and the boundary line where the resulting symmetric mirror image is determined by the Poission ratio. Additionally, if the situation involves more than one well, the solutions are provided for by the superposition if solutions of various points.

More complicated situations can be obtained by some analytical methods or numerical methods, which can be applied to identify parameters values from field measurements. The POEL program was specifically developed (by R. Wang) to address this. By using solution propagation and numerical transformation, the evolution of poroelastic models can be examined. Wang and Kümpel (2003) has depicted the mathematical concept; Fabian (2004) used POEL to demonstrate a multi-layered poroelastic problem. More details about the solution processing with the program will be seen in Chapter 5.

## 2.3 Instruments

Though several other instruments may be also capable of that purpose, the tiltmeter is favorable to record pump induced rock deformation for its high sensitivity, accuracy, and simple installation. The resolution of the instrument may be designed up to nano-radian range. In principle, effects of thermoelasticity, earth tides, hydrology or micro seismicity are detectable.

According to the theory mentioned above, the changes of pore pressure gradients are involved with the deformation of the subsurface. The variation of the water table fluctuation may reveal this changing situation. Therefore, the pressure transducer is the preferred instrument to monitor the chronic condition of the water table.

### **2.3.1 Tiltmeter**

The borehole tiltmeter, known as type vertical tiltmeter, is used to measure movements induced by pump operation along a vertical plane. In this way, the recorded tilt signals reflect both the pump induced deformation and the local gravity influence. Tilt variations can be illustrated as time series and as chronological variations in a hodograph, respectively. Twelve tiltmeters from three different types (AGI Model as from Applied Geomechanics Inc., GGA Model and Lippmann Model) were available and were simultaneously positioned at various monitoring locations in the research area. The features of the instruments are described as below:

The sensor of the AGI Model consists of a quartz tube containing an electrolyte and a gas bubble (Fig. 2.3a). When connected to electrodes, changes in the orientation of the bubble induce changes in the field potential and consequently in resistivity differences so that the movement is thus quantified. This type of tiltmeter is also known as bubble tiltmeter (AGI, 1999a). In this case, the sensor is installed within a steel tube casing with a length of 0.883 m and a diameter of 0.054 m. Two tiltmeters belong to this type and are denoted as A1 and A2.

The GGA tiltmeter is based on the prototype of the AGI model, but the components of the instruments are separately ordered from AGI and assembled by GGA institute (AGI, 1999b; AGI, 2000). The steel tube casing is 0.880 m long and has a diameter of 0.062 m. Four tiltmeters G1, G2, G3, and G4 are included in the study.

Lastly, the Lippmann Model is based on an entirely different design. Its sensor is based on an electronic pendulum (Fig. 2.3b). The pendulum is made of aluminum and acts as a condenser. Another two condensers are placed by the sides of (but not attached to) the pendulum. The amount of the movement is estimated by the inclination of this electronic sensor (Lehmann, 2001). The instrument casing has a

length of 0.670 m and a diameter of 0.050 m. Six tiltmeters L1, L3, L4, L5, L6, and L8 in this study are of this type. Each of the tiltmeter types hosts two sensors at perpendicular orientation in order to record tilt movements in two different azimuths.

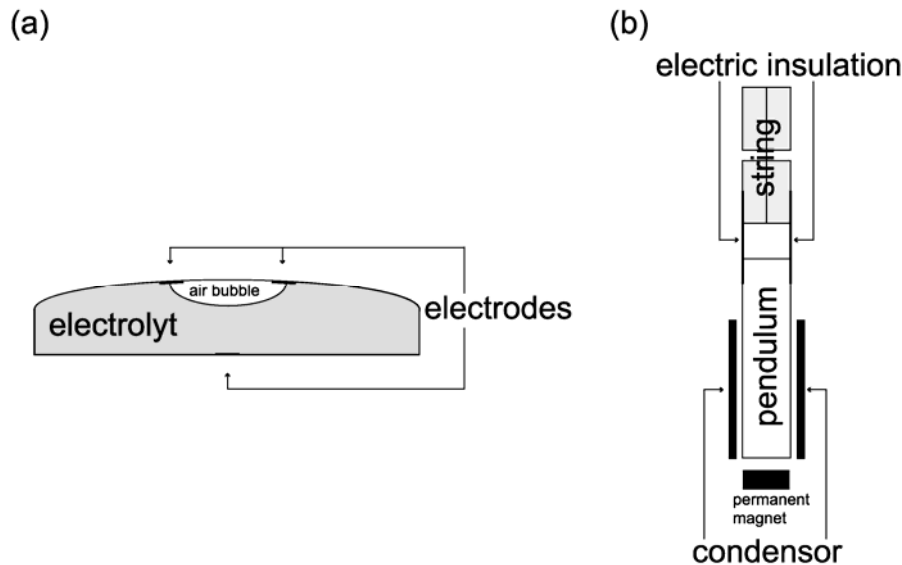


Fig. 2.3 Sketches of the sensors from different types of tiltmeters. (a) AGI Model (b) Lippmann Model.

All types of tiltmeters are positioned in holes of ca. 2 m depth and 0.15 m diameter. Fine sand is loaded in the ring space to stabilize the tiltmeter and cover it up to 90 % of its length. From the surface, a 1 m-deep soil wall is fastened by a PVC tube with a diameter of 0.125 m, whereby the gap between the wall and the tube is filled with sponges to reduce mechanical effects from ground freezing in winter time. Several measures were used to prevent any intrusion to the instrument: near the surface, the hole is covered by a lump of sponge (in the tube), plastic wrap and a mass of sand (above the tube). The tiltmeters are connected to a data recording system which is packed in a plastic briefcase and set above the mass of sand. On top, a plastic bucket is inverted to cover the entire installation to ensure waterproofing (Fig. 2.4).

The data recording system includes a rechargeable lead battery, a signal filter, and a data logger. The life capacity of the battery is around 8 days necessitating weekly replacement. Using the gain function of the filter, a resolution of up to 0.1  $\mu\text{rad}$  is obtainable, meaning that the tiltmeters can detect horizontal motions of 0.1  $\mu\text{m}$

along a 1m long vertical line. A memory card of 512 MB is inserted into the data logger and changed weekly. The data logger is activated by turning on a key and is able to record the changes of X- and Y-axis, temperature of instrument and battery capacity. Because the tilt records are measured in voltage and since each tiltmeter has its own mechanical coefficient, an adjustment parameter is required to determine the actual amount of the movements (Rifai et al., 2007). Additionally, an adjustment equation is applied to reduce the temperature effect of the instruments (Table 2.1).

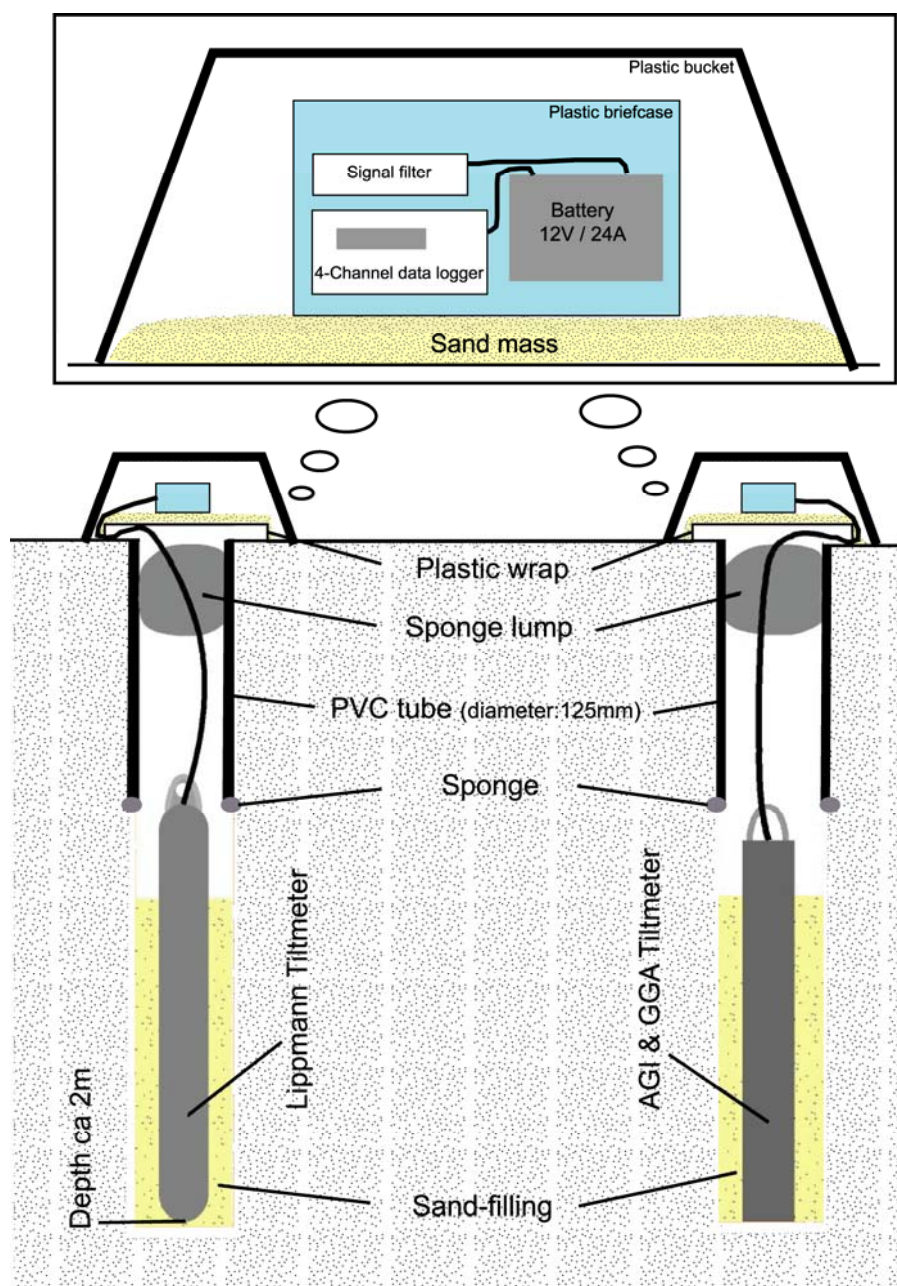


Fig. 2.4 The installation of the tiltmeter and its data recording system.

Type		AGI		GGA				Lippmann					
Size (mm)		54 × 883		62 × 880				50 × 670					
Tiltmeter		A1	A2	G1	G2	G3	G4	L1	L3	L4	L5	L6	L8
Adj. parameters ( $\mu$ rad/V)	TX	100.6	100.2	99.6	99.2	100.4	100.8	220	187	194	201	190	212
	TY	100.2	99.4	99.6	100.0	100.6	99.6	232	182	195	201	203	219
Adj. equation	TT	T / 100						3.4515-3.62918 × T / 10000 + 0.0147554 × T <sup>2</sup> - 0.0176562 × T <sup>3</sup>					

Table 2.1 The tiltmeter standards for different types and their adjustment parameters and equations for the movements in X-, Y-axis and instrument temperature T.

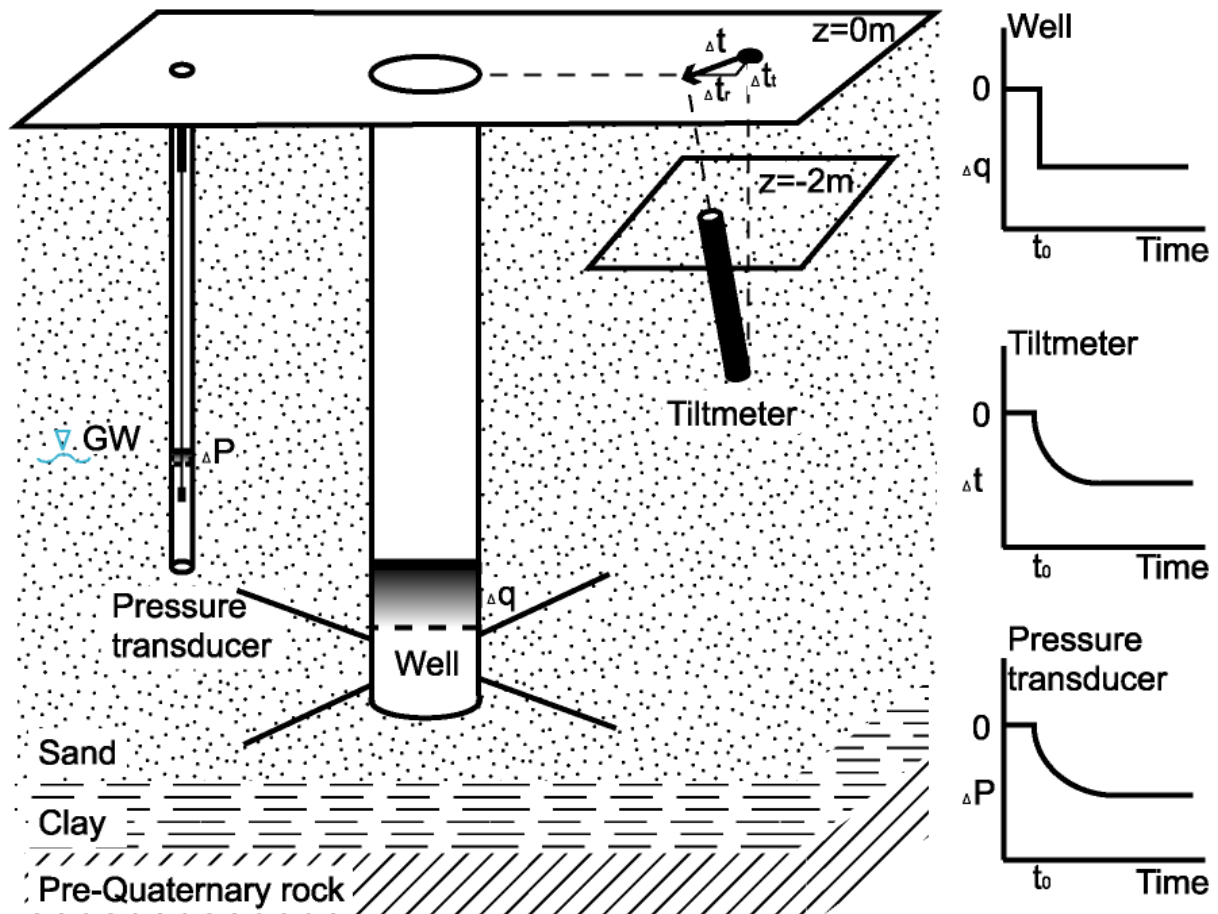


Fig. 2.5 The sketch of the measuring concept. When a tiltmeter is positioned in the vicinity of a well, its induced tilt motion ( $\Delta t$ ) by pumping ( $\Delta q$ ) can be illustrated in the radial vector ( $\Delta t_r$ ) and the tangential vector ( $\Delta t_t$ ). Ground water table is denoted as GW. The water pressure ( $\Delta P$ ) is recorded by a pressure transducer that is particularly depicted in the subsequent section.

Assuming a tiltmeter is positioned 2 m deep ( $z = -2$  m) and a tilt motion is induced by a pump operation (Fig. 2.5). When the tilt motion is projected to the plane of ground surface ( $z = 0$  m), the vertical deformation along the radial vector is denoted as  $\Delta t_r$ . The quantity is defined by its radial variations against its vertical variations (eq. 2.9). The corresponding vector perpendicular to the radial vector  $\Delta t_r$  as tangential vector  $\Delta t_t$  is also defined by the tangential variations against the vertical variations.

$$\Delta t_r = \frac{\partial u_r}{\partial z}, \text{ and } \Delta t_t = \frac{\partial u_t}{\partial z} \quad (\text{eq. 2.9})$$

The azimuth indicating the tilt angle is thus estimated by the arc-tangent value of these vectors. Taking the square root for the sum of the square values of these vectors, the amplitude of the induced tilt is determined (eq. 2.10).

$$\Delta t = \sqrt{\Delta t_r^2 + \Delta t_t^2} = \sqrt{\left(\frac{\partial u_r}{\partial z}\right)^2 + \left(\frac{\partial u_t}{\partial z}\right)^2} \quad (\text{eq. 2.10})$$

### 2.3.2 Pressure transducer

The variations of the water table can be recorded by pressure transducers consisting of a steel casing (including the air pressure sensor and the logging system) and a sensor cable. Two types of steel casings are used in this study. The old type is 53.35 cm long and contains 8 batteries while the new type is 38.1 cm long with 6 batteries. The diameter of both types of casing is 4.83 cm. The logging system is able to inscribe records in 5 channels and largely used to obtain information about water table fluctuation, air pressure, and temperature. The memory capacity is 256 kB, allowing 65000 datasets of time and 2 channeled records (Rifai et al., 2004).

The sensor cable is composed of a string of cable attached to a small cylinder head containing the sensor (consisting of the membrane and the capacitor) in its initial end. The length of the cable required is determined by the distance between the bottom of the steel casing and the water table level. A length of cable longer than 5 m was used to position the cylinder head below the water table level to sense changes of hydraulic heads at all times. A change in the water column of a meter corresponds to ca. 0.1 bar of water pressure changes, under the condition that the temperature and density of water is 11 °C and 999.6 kg/m<sup>3</sup>, respectively.



The cylinder head also comes in 2 types: one with a thicker head (with a diameter of 38 mm) contains an additional temperature sensor while the other with a thinner one (diameter: 20 mm) only has water pressure sensor. The manufacturers of the instruments are PHYTEC and DRUCK, respectively. The sensors with a resolution better than 1 mm are used. When activating the recording program, the thin type has auto-calibration function, but the thick type has to be calibrated manually. When connected to a terminal panel, the data stored in the instruments can be downloaded. Data calibration and alignment are done by Prodata, which is a program supplied together with the instruments.

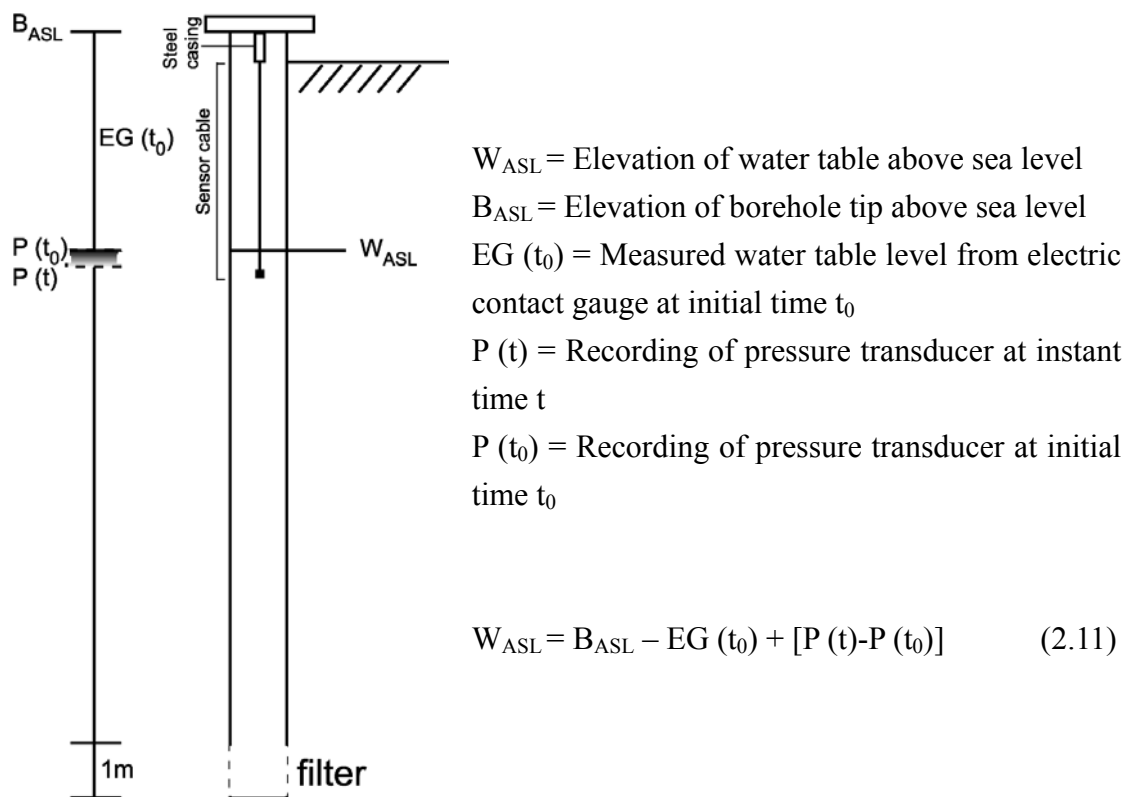


Fig. 2.6 The installation of a pressure transducer for water table measurements and the equation for calculating the water table level.

Figure 2.6 illustrates the installation environment of the measurement. The instrument is hung under the cover of the borehole; a more detailed description is available in Section 3.3. In this sketch, an explicit equation (eq. 2.11) to calculate the variable height of the water table from the output data of the pressure transducer is shown. Parameters necessary to be included into the equation are: the elevation of the borehole where the instrument is positioned ( $B_{ASL}$ ), the water table level manually

measured by electric contact gauge when the instrument is activated at initial time  $t_0$  ( $EG(t_0)$ ), and the recording data of pressure transducer at same moment ( $P(t_0)$ ).

At  $t_0$ , the water table level is actually the difference between  $B_{ASL}$  and  $EG(t_0)$ . But for subsequent periods, the water table level is considered to be under a state of continuous fluctuation so that a varied amount is estimated by the difference between  $P(t_0)$  and subsequent recording data  $P(t)$ . Therefore, the varied level of water table can be calculated at all times, by subtracting the height of the borehole reduced by the depth of the water table level with the variation of the water table (eq. 2.11).

## Chapter 3 Observations

The research area has only one shaft well, called the central pit hereafter, and eight horizontal screen tubes. However, the distribution pattern of the screen tubes and its resulting influences adds complexity to the study. The whole facility is surrounded by a parallelogram-shaped fence with a width of 140 m and a length of 156 m. The main entrance is located at the South of the area and the central pit can be accessed through a 75 m long sandy graveled path.

To record the size of near-surface movements over time, several tiltmeters are positioned. Changes of the pore pressure gradient are recorded by pressure transducers that reveal the conditions of water table fluctuations. Because of the capacities of the available rechargeable batteries and the limited memory capacities of the logging instruments, a weekly inspect visit is necessary. Additional geophysical methods as seismics, electrical and electromagnetic measurements are also undertaken to verify the existence of heterogeneities in the subsurface.

### 3.1 Geometric distribution

The forcing source to induce tilt signals mainly comes from the pumping well constructed by Hanover waterworks in Fuhrberg. The well is located centrally within our investigation area and connects to 8 horizontal tubes. These tubes, composed of 20 meter long transport sections and 50 meter long screens with asteroidal distribution, serve to gather groundwater to contribute to the water supply of Hanover county area (Fig 3.1a).

The central pit is a 25 m deep shaft well with a cylindrically-shaped interior of diameter 4 m. The upper construction of the facility is covered by a rectangular concrete building measuring 11 m × 8 m × 6 m. The altitude of ground surface of this foundation is 35.45 m above sea level. There are two pump heads within this central pit, denoted as PV1 and PV2. Both pump heads have a similar maximum withdrawing discharge of 400 m<sup>3</sup> / h. In general, the pumps are alternatively turned on and off every 2 days and maintain an average assemblage sum of 300 m<sup>3</sup> / h.

The 8 asteroidal screen tubes are 0.2 m in diameter and stretch out in the

underground at a depth of 20.5 m (Fig 3.1b). The tubes are separated from each other by 45°, and their orientations are approximately 8 azimuths: E, SE, S, SW, W, NW, N, and NE, with about 17° anticlockwise difference from the exact orientations. For convenience, each screen tube is named according to the main azimuth orientation where it is close to.

Besides the main constructions, several boreholes are found at the site, which might have been used for conducting specific hydraulic tests during the construction of the well assemblage. Their presence is taken as an advantage as they are used as observation wells to continuously monitor the water table variations.

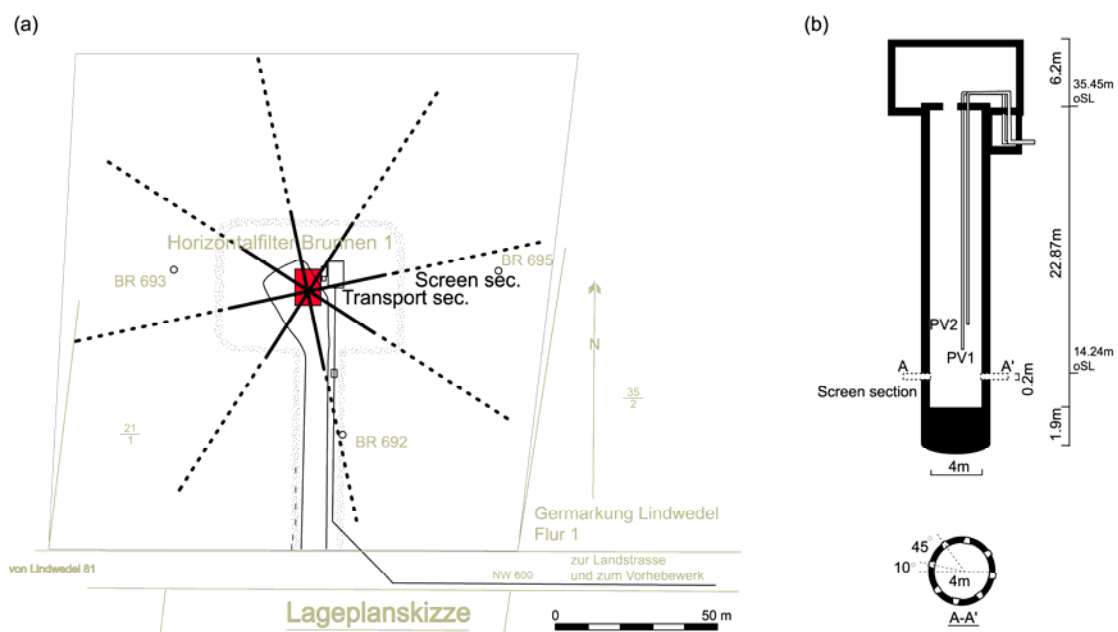


Fig 3.1 (a) The layout of the well location. (b) Profile of the central pit.

### 3.2 Tiltmeter campaign

To understand the influences from groundwater pumping through the central pit and its screen tubes on ground deformation, the tiltmeters should ideally be distributed equally into 8 groups (with two tiltmeters being assigned to a group) since the 8 screen tubes are entirely open and function well. However, each screen tube may include too many physical or hydraulic variables, such as individual discharge amounts, variable hydraulic conductivity of the surrounding sediments, degradation of screen inlets etc. Therefore, to simplify the analyses and to focus on horizontal diversions, we first placed 12 tiltmeters along one screen tube in the West flank and

subsequently shifted them systematically to the next screen tube in a clockwise direction until sufficient signal events were collected after several months. For this study, a semicircle monitoring loop has been completed in the research area.

During the positioning of tiltmeters, slight adjustments of their locations have been made if the planned spot coincides with tree trunks. The tiltmeter closest to the screen tube in the first row at the south flank is the one fixed as a standard. The locations of the tiltmeters are denoted as F1, F2 etc. Detailed information about the type of the tiltmeters used in different locations is shown in Fig 3.2 and Table 3.1.

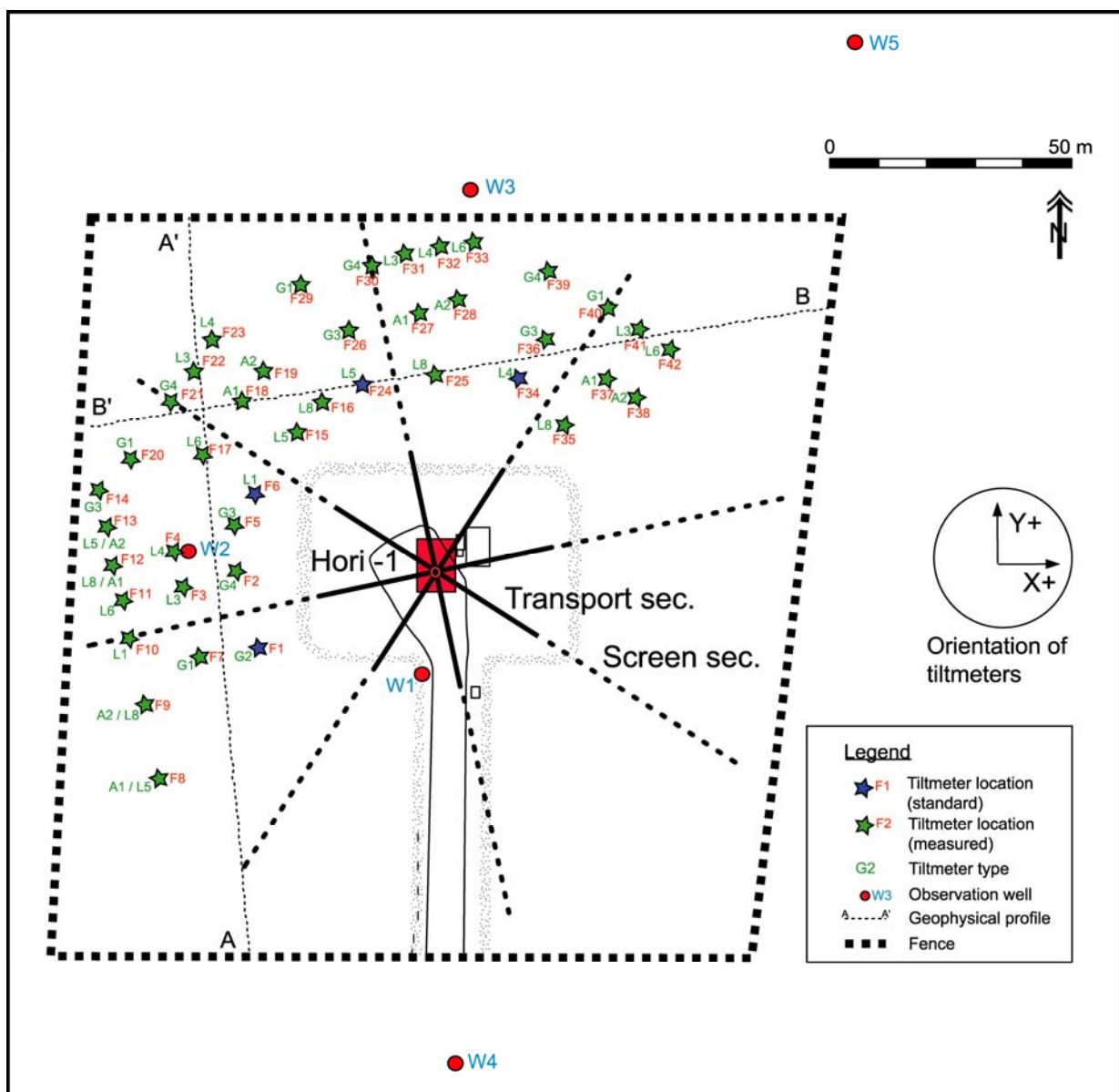


Fig 3.2 Locations of all monitoring positions of tiltmeters.

To ensure that every tiltmeter array maintains an equal distribution alongside a screen tube, all tiltmeters were arranged in 3 rows with corresponding distances of beginning, middle and end part of the screen tube. The first and the last rows are 40 m and 70 m away from the central pit, respectively. All rows are separated equally and maintained at a fixed interval of 12.5 m between each other. When the view facing the central pit is taken, the tiltmeters can be seen to be placed in several lines parallel to their surrounding screen tube, where the interval between each line is 7.5 m. To show any contrasts in the results of both sides of the screen tube, the tiltmeters positioned on the left flank are chosen to be experimental sets while on the right flank are control sets, so that a more complete route of installation is planned on the left flank (Fig 3.2).

position to screen tube		row 1			row 2			row 3		
		loc.	type	month	loc.	type	month	loc.	type	month
<b>W flank</b>										
right	line 4							F8	A1 / L5	8
	line 2							F9	A2 / L8	8
	line 1	F1	G2	24+	F7	G2	10			
middle	line 0							F10	L1	8
left	line 1	F2	G4	10	F3	G4	10	F11	L6	10
	line 2				F4	L4	10	F12	L8 / A1	10
	line 3							F13	L5 / A2	10
	line 4							F14	G3	8
<b>NW flank</b>										
right	line 2	F5	G3	5.5				F20	G1	3.5
	line 1	F6	L1	16+	F17	L6	3.5			
middle	line 0							F21	G4	3.5
left	line 1	F15	L5	5.5	F18	A1	3.5	F22	L3	3.5
	line 2	F16	L8	5.5	F19	A2	3.5	F23	L4	3.5
<b>N flank</b>										
right	line 2							F29	G1	6
	line 1	F24	L5	10+	F26	G3	6			
middle	line 0							F30	G4	6
left	line 1	F25	L8	6	F27	A1	6	F31	L3	6
	line 2				F28	A2	6	F32	L4	6
	line 3							F33	L6	6
<b>NE flank</b>										
right	line 2							F39	G4	4
	line 1	F34	L4	4+	F36	G3	4			
middle	line 0							F40	G1	4
left	line 1	F35	L8	4	F37	A1	4	F41	L3	4
	line 2				F38	A2	4	F42	L6	4

Table 3.1 Positions, instrumental types and monitoring durations for each tiltmeter array. Position attributes right and left hold for a view facing the central pit.

The durations of monitoring are shown in Table 3.1. More details about the installation and some measuring dates are given in Appendix A. The shortest monitoring period for a whole array was about 3.5 months while the longest was 10

months. Within each array, one tiltmeter is further on kept in its original position as a reference to determine if any discrepancies between 2 screen tubes exist. This means that the number of tiltmeters along the screen tubes was reduced from 12 to 11, 10 etc. after shifting the array to the NW flank and so on. In Table 3.1, F1, F6 and F24 represent those locations used as references. Location F1 has been serving in this way since the beginning of this research that is for nearly 2 years of monitoring. The lengths of monitoring periods strongly depend on the sufficiency of the records in terms of number of significant pump induced tilt events, and may be related with seasonal changes. More statistics of the data are shown in the next chapter.

The sampling rate is set to record data every minute which is sufficient to resolve the required signals. From a bird's view, the arrangement of the tiltmeters alongside one screen tube appears fan-shaped. Taking the locations of the tiltmeter installations for all 8 screen tubes, a ring profile will be completed. An advantage of using such arrangements is that results of signal magnitudes between different lines and rows are easy to compare. Thus, the general near-surface movements induced by the pumping operations from the central pit and the influences from the screen tubes may be determined.

From the primary short-term tiltmeter data, several characteristic factors generating tilt signals are shown in Fig 3.3. These factors are associated with the influences from hydraulic and meteorological conditions: pump rate (PR), water table fluctuations (WT), stormy wind periods (Wind), switching between the two pump heads (PV1 and PV2), changes in pore pressure gradient and effects of surrounding vegetations, respectively. The effects may combine and be reflected altogether in the tilt signal.

Fig 3.3 shows an example of one week data in X-axis response at F10 and illustrates the correlations between these effects and the tilt signal. Generally, the tilt curve presents diurnal or semi-diurnal variations, but seems to be more influenced by the factors mentioned in the preceding paragraph. The tilt curve presents a “jump” variation with a sudden increment while pump rate increases, which is also associated with the water table descending; vice versa. And when the wind speed increases, an obvious disturbance emerges in the tilt curve. Besides, occasionally some spike-like

signals appear. They represent the passage of seismic waves from earthquakes occurring in different locations worldwide. The effects mentioned above are the most frequently seen in tilt signals.

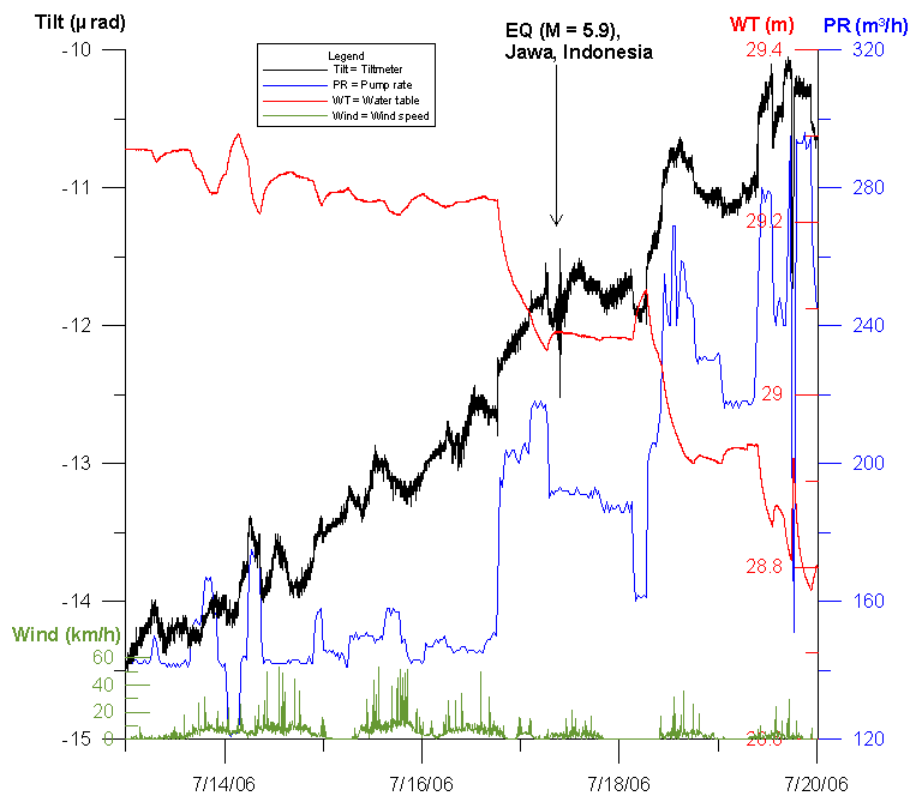


Fig 3.3 Comparison between different factors with influence on tilt signals.

### 3.3 Water table measurement

From the existing boreholes, 5 locations were selected as observation wells and have been equipped with pressure transducers for stationary monitoring of water table fluctuations. Although these boreholes have varying pipe sizes, adjustments were made to suit the installation of the pressure transducers. By using a clamping sustainable metal plate of flexible size, the pressure transducer may hang above and its connecting sensor extends below the water table in the well. The wells are named in sequence from W1 to W5. Their locations are arranged to grossly cover the study area as follows: W1 and W4 in the South, W2 in the West, W3 in the North, and W5 in the Northeast (Fig 3.2).

Information about borehole sizes and the radial distances of the wells from the central pit are listed in Table 3.2. The given depth of the water table is a reference



value. It is measured manually by an electric contact gauge each time the measurements are re-activated after memory capacity clearing. The depth of the water table in the area lies between 5 to 6 m below the surface.

Observation well No.	Diameter (cm)	Depth (m)	Elevation ASL (m)	Distance to central pit (m)	Water table depth on May. 22 <sup>nd</sup> of 2006 (m)
W1	10.2	13.81	35.39	21	5.74
W2	10.2	10.85	35.49	50	5.96
W3	4.9	15.92	35.39	78	4.97
W4	10.2	10.05	34.63	100	5.58
W5	12.9	32.97	35.23	126	5.86

Table 3.2 Parameters of observation wells W1 to W5.

Some general hydraulic parameters can be estimated from the monitoring results. Additionally, since water table fluctuations could be a relevant source causing near-surface movements, the sampling rate is set as one record for every minute for comparison against the results of the tiltmeters. Hence, simultaneous monitoring of relevant situations can reveal potential relationships between pore pressure gradient and ground deformation.

Fig 3.3 shows that variations in the water table are most significantly influenced by changes in pump rates. However, initial data from 5 of the observation wells (Fig 3.4a) indicated that the fluctuation patterns are rather inconsistent. We would expect that the location of the well with the shortest distance to central pit, revealing the largest fluctuations in water table elevation; yet this characteristic varied from W1 to W5 several times during the first 6 months. The circled periods in Fig 3.4 illustrate the changes among these different locations. Despite this, W1, which in fact is the nearest location to the central pit, continues to exhibit the largest fluctuations in its water table most of time.

Additionally, the turbulent part of the long-term fluctuation pattern shows a general two-typed variation: W1 and W4 behave in a similar manner while W2, W3 and W5 respond in another way. Transient changes in hydrodynamic conditions can be estimated by the streaming movements or discharge potentials (Schafer, 1996; Chesnaux et al., 2005; Kelson et al., 2005; Muralidharan et al., 2005). If these

observations are verified, taking the strongest turbulence/largest fluctuation as water withdrawing location, it may imply that the hydraulic flow direction between the 8 horizontal wells changes in a time-dependent fashion from the South to the West or the North rather than being constant. This may further affect the tilt results associated with the changes of the pore pressure gradients.

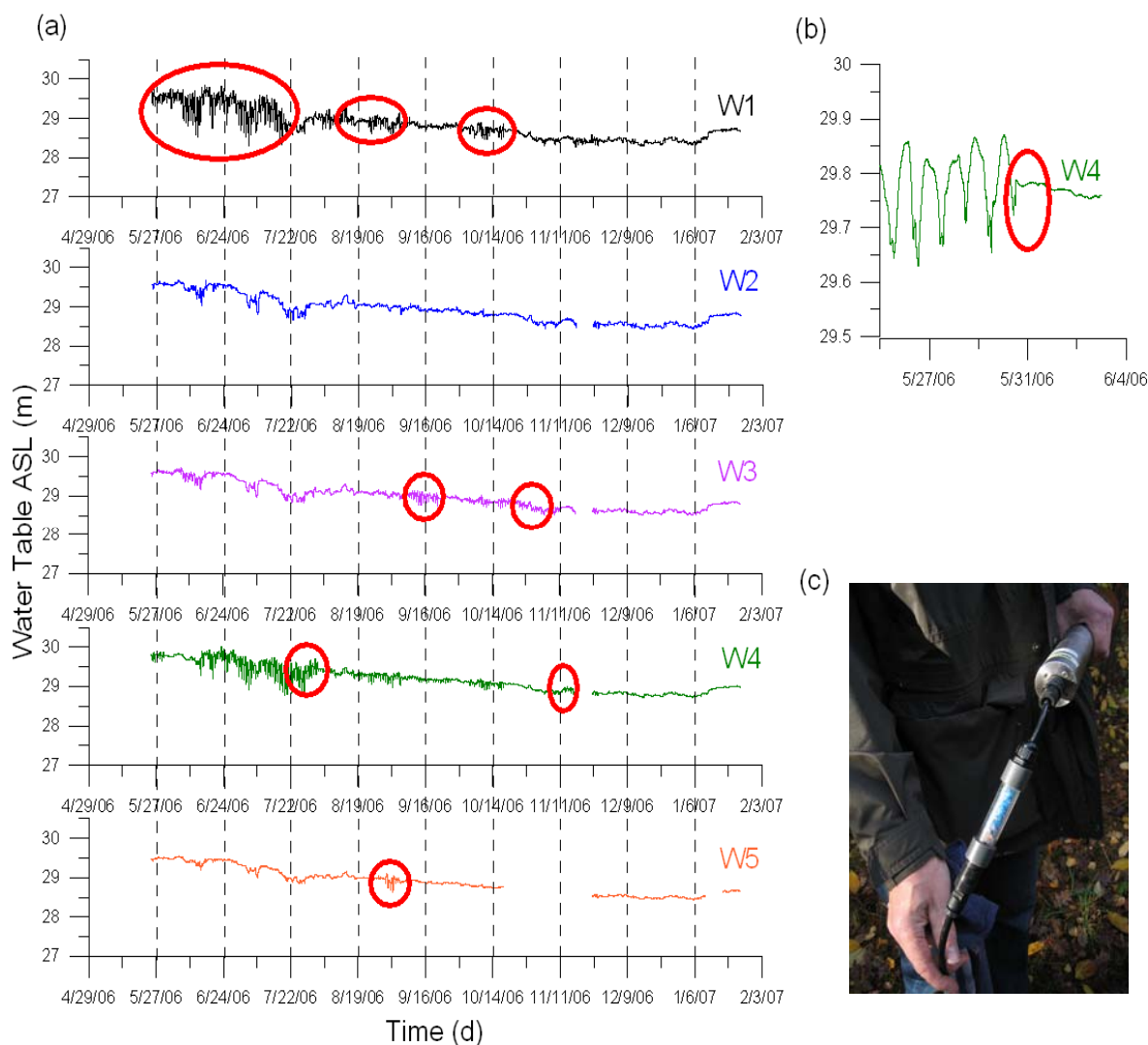


Fig 3.4 Results and refinement of water table measurements. (a) Beginning results of 5 observation wells among 9 months. (b) An example of turning point in fluctuation pattern. (c) A picture of dryer tube connecting to pressure transducer.

However, if the data is further scrutinized, the sudden changes of fluctuation patterns seem to occur mostly on the day of the routine inspections (Fig 3.4b). This suggested that the preconditions of monitoring, such as the temperature or the pressure of the sealed wells or chambers of the instruments may slightly change while

the cover of the well was opened during data collection.

To minimize such fluctuations, a second device, called a dryer tube, was connected between the pressure transducer and the cable sensor. The interior of the tube, measuring 10 cm long with a radius of 2 cm, contains silica beads and conducting wires. A pinprick-sized hole was machined on the top of the tube. Both sides of the tube are covered by pin plugs, and an extra 15 cm long cable is connected to this device for data transfer. The silica beads and the hole serve to prevent humidity from penetrating into the instrument and to maintain proper circulation of air pressure between the inside and outside of the instrument. This minimizes sudden pressure increases within the chamber of the instrument. Due to the installation of the dryer tubes the disturbances in the fluctuation patterns have been eliminated. This is seen from the more consistent variations in water table fluctuations in the data obtained from all the 5 observation wells for the last three months (Fig 3.4a). The gap appearing on the recorded data indicates the time while the dryer tubes were installed. Additional monitoring has ascertained the effectiveness of this refinement.

### 3.4 Other geophysical surveys

The study site is considered to be planar at first approximation which is the ideal environment to install tiltmeters. However, at closer look, some small hills are seen in the geomorphology. Further, though the disposal of the drilled holes of the tiltmeters is mostly sandy material, the possible heterogeneity of deeper formations should also be considered. Therefore, two nearly linear transects were plotted in Fig 3.2 to undertake additional geophysical measurements to determine the subsurface compositions or structures. The A-A' transect is approximately in N-S direction as B-B' is in E-W direction. Both transects cross 3 screen sections with tiltmeters positioned along them.

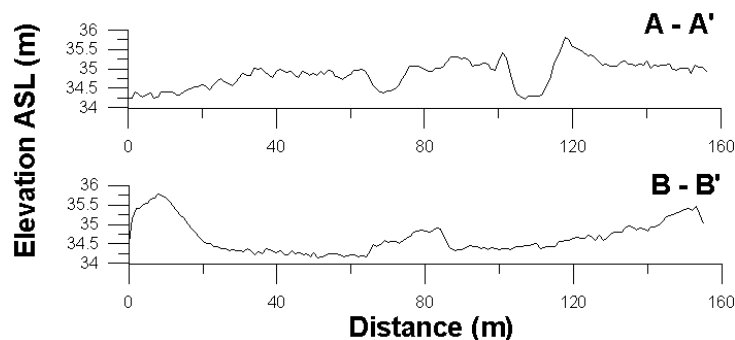


Fig 3.5 Elevation display along the profile for additional geophysical measurements.

From Fig 3.5, we can observe differences of the elevation along these transects. The coordinates along the transects and elevations (listed in Appendix B) were measured using GPS (Global Positioning System) with an accuracy of 1 mm for the exact locations and 2 – 3 cm for the elevations. The transects start from the fences, and the distances were measured northerly or westerly away from this point. The total length of A-A' transect is 156 m long while B-B' is 155 m, and the average elevation of both transects is about 34.5 m above MSL. Taking A-A' transect, the elevation displays a hilly linear with 2 minor clefts situated between 60 to 80 m and 100 to 120 m away from point A. The largest difference in the elevation is about 1.5 m. After dividing the difference in the elevation by their respective specific distances, two slopes with gradients of  $4.3^\circ$  and  $8.5^\circ$  are obtained. Though B-B' transect shows a relatively smooth topography, 2 small hills appear at a distance of approximately 10 m and 85 m of B, possessing slope gradients of  $7.1^\circ$  and  $8.5^\circ$ , respectively. The result indicated a relatively large variation in geomorphology. Hence further underground investigations using seismic reflection, DC (direct current) resistivity and GPR (ground penetrating radar) measurements were found to be useful.

### **3.4.1 Seismics method**

The principle of the seismics method is based on the transmissive velocities of the induced seismic waves. Basically, the waves are generated from a defined source (a sledgehammer, a vibrator or dynamite) and transmit through various subsurface formations. By measuring the time elapsed between the origin of wave generation to the arrival of the reflected or refracted seismic waves, the wave velocity is determined. This method is able to discriminate the physical properties of different layers and some characteristic structures or features could even be imaged using these differentiated properties. Besides, although some energy attenuation occurs while waves transmit, the degree of attenuation anisotropy may also assist in the determination of subsurface material. The material properties are sometimes useful to engineering purposes and may be equivalent to the values of some engineering tests, hence, the seismic imaging technique is prevalently utilized for various purposes (Chourak et al., 2003; Best et al., 2007; Long and Donohue, 2007).

Several studies have shown the advantage of using shear wave seismology for shallow subsurface investigations. Although it requires a more powerful seismic source to produce waves of higher dominant frequencies, the vertical resolution obtained is better than the results of longitudinal waves. In addition, reflections from the water table or changes in fluid saturation contribute less to the image resolution so that the appearances of stratigraphic interfaces or tectonic configurations are more easily clarified. Compared with ground penetrating radars, it can be used for probing greater depths (Dasios et al., 1999; Harris and Sorrells, 2003; Haines et al., 2007; Turesson, 2007). Therefore, we surveyed with the shear wave reflection method as priority along the pilot transect A-A'.

Recording system	Geometrics Geode
Receiver type	Single geophones SM6-H 10 Hz
Number of recording stations	151
Geophone spacing	1 m
Shot spacing	1 m
Line length	156 m
Source type	SH-Vibrator, electro-dynamic
Source signal	40-200 Hz linear Sweep, 10 s duration, 100 ms cos-Taper
Record length	11 s
Sample rate	1 ms

Table 3.3 Specific parameters for shear wave reflection survey.

Processing step	Purpose
Geometry editing	Definition of locations for subsequent calculations
Negative and positive S-wave traces summing	Removal of residual P-wave
Geometry information copying into seismic data header	Data arrangement by reflection point
Elevation statics calculating	Elevation Corrections for the transect
Stacking velocity picking	Determination of stacking velocity
Normal moveout with stacking velocity and stack	Reflectors flattened for stacking and noise reduction
Migration	Geometrical correction of stacked image
Apply depth conversion	Convert vertical axis from time to depth
Setting of the data to final datum	Elevation modification to in-situ condition

Table 3.4 Processing flow for seismic data.

The available seismic source with an electro-dynamic vibrator provided sufficient energy for conducting the measurements. The signal frequency was adjusted to vary from 40 to 200 Hz with 2 linear sweeps to amplify the results. The geophone spacing was set to be 1 m, as well as the shot spacing, to receive a detailed image at shallow surface. The survey was carried out from the point 5 m away from the fence edge. More specific parameters and the data processing flow are listed in Table 3.3 and Table 3.4.

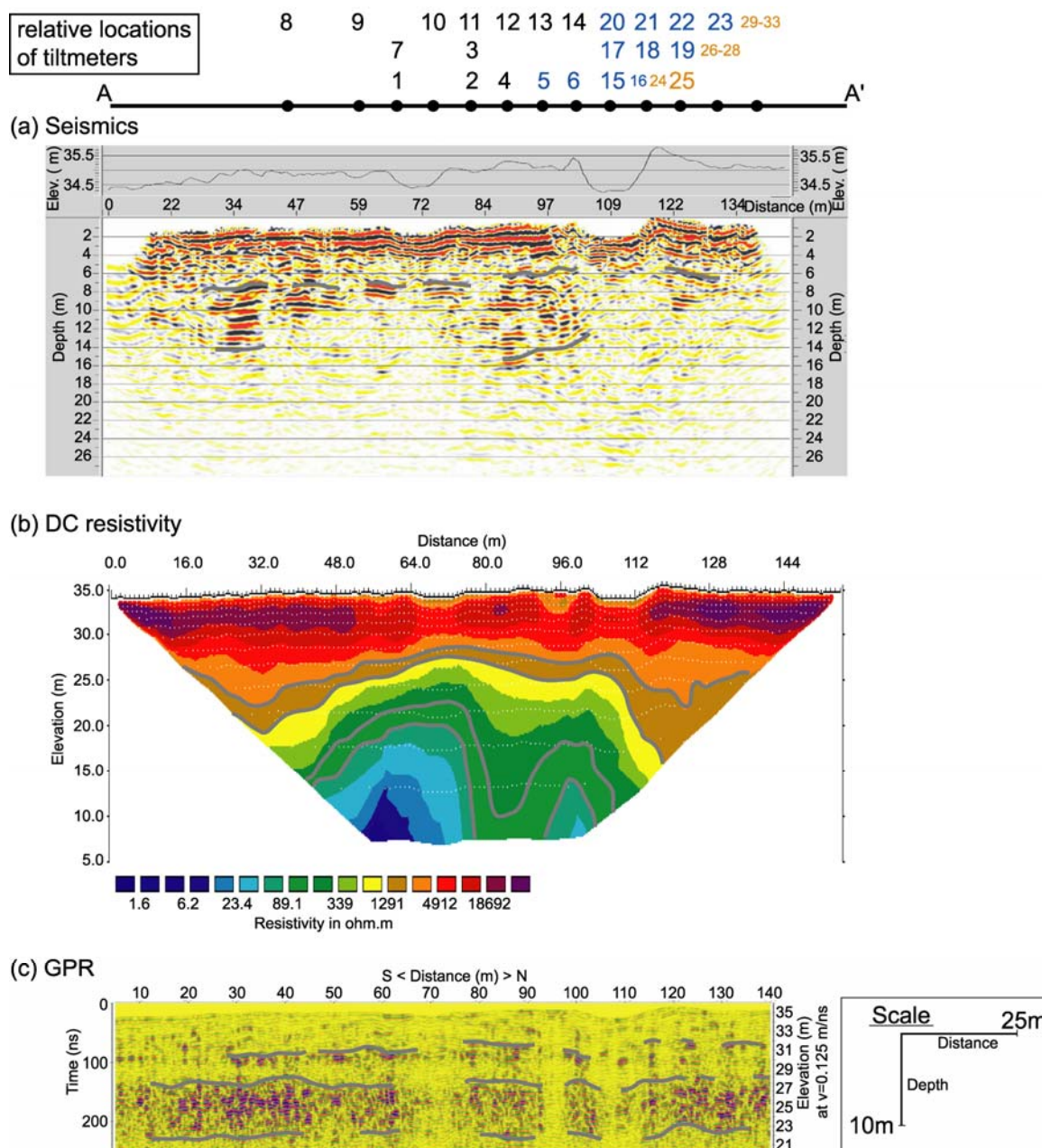


Fig 3.6 Results of additional geophysical surveys along A-A' transect: (a) seismic, (b) DC resistivity, (c) GPR.

Even though standard protocols were used for data processing, we had difficulties obtaining a result better than that shown in Fig 3.6a. Because the topography of A-A' transect is not ideally plain, and several big trunk trees sometimes obstruct the profile, the coupling between the ground and the vibrator was not optimal. Though the resolution of the image may not fit in with the best criteria, the layering continuity is distinct to the depth of 6 m. When compared with the borehole data (Fig 2.2), this may indicate the interface of sand and gravel formations. Besides, around distances of 35 m and 90 m and at a depth of 8 m, strong reflecting signals were observed appearing as small lump shapes. There is a possibility that this is related to the existence of some small structures due to some lateral heterogeneity, but partially obscured imaging requires a further survey for verification (Appendix C).

### 3.4.2 DC Resistivity method

Another method to gain better understanding of spatial distributions and physical properties in the subsurface is electrical resistivity tomography. The method is speedy, noninvasive and is of relatively low cost. By the contrasting electrical properties of the surrounding materials, some features, such as the geometry or depth of burial within, can be distinguished in terms of resistivity or conductivity. As in hydrogeology, the resistivity profiles and cross sections provide the vertical and lateral changes of subsurface. For hydrology, some signs of the transient hydraulic processes, water saturation or the seasonal variations in vadose zone soil moisture are indicated (Senosy and Riad, 1998; Chambers et al., 2002; Chambers et al., 2006; Furman et al., 2007; Malkowski et al., 2007; Park et al., 2007).

In other studies, the measurements were made using surface or downhole multi-electrode arrays connected to a computer-controlled system which collects the resistivity and induced polarization data. Four typical configurations of arrays are: Wenner, Schlumberger, dipole-dipole and square. Each array has its advantages but, based on the desirable suitability for sensitivity to lateral inhomogeneities and vertical resolution, the Wenner array was selected. Reported examples on the discovery of buried dykes, discontinuous permafrost delineation and leachate migration of landfill further add to the appropriateness of this configuration (Batayneh, 2001; Chambers et

al., 2006; Astley and Delaney, 2007).

The PC controlled 2-D DC resistivity measurement system (RESRCS) was used. The spacing between the electrodes is 1 m. From Fig 3.6b, the result of DC resistivity on A-A' transect shows relatively horizontal variations on its lateral section. The resistivity generally decreases with increasing depths, apart from shallow depths above the elevation of 30 m, and below the elevation of 15 m. Some selected resistivity data from common geologic materials are listed in Table 3.5 (adapted from Chapter 7, Reynolds, 1997), ranked in order of increasing resistivity values. The table presents possible alternatives of the existing formations in our study area. When compared against the borehole data (Fig 2.2), the value of dry gravel material may suit for the formation from 8 to 10 m depth, underlain by alluvium and sand material to 30 m depth. Among the thickness of sandy material, the appearance of saturated gravel formation is also likely intersect at depth of 15 m, and below layers followed with clayey sand or clays. However, there is no indication from the results to show the existence of water table at shallow subsurface.

The high resistivity zones roughly match the value of the moraine and permafrost material. Although there is no supporting information from borehole data, this shallow formation may simply represent a similar formation consisting of different water content and porosity. For some reason, this shallow formation does not display a continuous lateral structure. A large gap was observed from along 50 m to 115 m of the transect. This may suggest that certain inhomogeneity exists at shallow depths. The very low resistivity zones occur at the depth of screen tubes which are stretched out at about 22 m depth (Fig 3.1b). Yet the low values reflect clayey layer rather than the screen tubes.

Similarly, on transect B-B', these low resistivity zones do not refer to the existence of screen tubes (Fig 3.7): the extensions of these zones are even larger than on A-A' transect, the appearance does not diminish to the dot shape and the resistivity value of these zones is an order greater and belongs to the geomaterial range of sand and gravel or clayey sand (Table 3.5). This implies the possibility that the presence of these low resistivity zones may be partly due to the data inversion processing.



Material	Nominal resistivity ( $\Omega\text{m}$ )
Marls	3-70
Clays	1-100
Clay (very dry)	50-150
Sand clay/clayey sand	30-215
Sand and gravel	30-225
Dry sand soil	80-1050
Alluvium and sand	10-800
Gravel (saturated)	100
Gravel (dry)	1400
Moraine	10-5000
Permafrost	1000 -> 10000

Table 3.5 Resistivities of selected common geologic materials (after Reynolds, 1997)

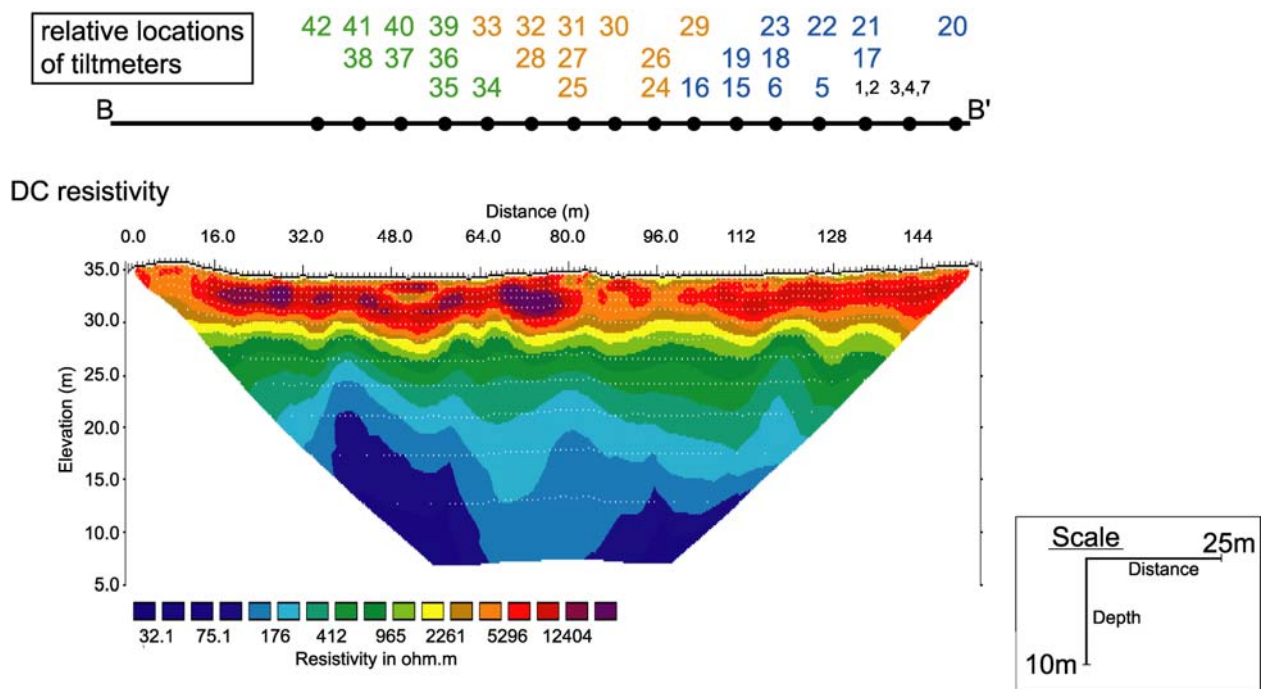


Fig 3.7 The result of DC resistivity on B-B' transect. Note that color coding is different from in Fig 3.6b.

The other resistivity values in B-B' transect are similar to the results of A-A' transect, except that the elevation of respective resistivity values is about 1 m to 2 m higher. This could be due to a cessation of regular pumping operation while B-B' transect was measured and hence a rising level of water table causing a different saturated condition of the geomaterials. The existence of inhomogeneities is still observed at shallow surfaces.

### 3.4.2 GPR method

The tomographic data from shear wave reflection and DC resistivity depict the probable subsurface conditions of the region above 6 m; deeper regions remain opaque to these methods in the study area. Ground penetrating radar (GPR) is another technology for subsurface survey. GPR was developed for glaciological applications because of its unique suitability for use in frozen media. More recently, it has also become a useful tool for subsurface investigations (Munroe et al., 2007). The reflectivity of the radar waves is sensitive to the changes in air/freshwater ratio or porosity (variations in water content and grain size can react on its signal contrast). Such anomalies or formation sequence can thus be recognized (Carreon-Freyre et al., 2003; Pessoa and Travassos, 2007). Hence, GPR was employed as the third geophysical method of survey.

Recording System	GSSI SIR System-20
Samples/Scan	512
Recording Filter	GSSI-Convention
Frequency	80 MHz
Recording Length	250 ns and 300 ns
Polarity	Transmitter and Receiver parallel to the recording line Distance Transmitter/Receiver 2.5 m
Frequency	200 MHz
Recording Length	200 ns and 250 ns
Polarity	Transmitter and Receiver perpendicular to the recording line

Table 3.6 Specific parameters for GPR measurement.

The GPR measurement depends on the delivery of electromagnetic energy and

the permissible transmission of radiowaves through various materials, with the assistance of an array of equipment: a signal generator, transmitting and receiving antennae and a receiver. The propagation velocity is estimated via processing of the collected data with specific geometry. It is related to a material dielectric constant and can be used to reveal hydrogeological features (Hubbard et al., 1997). To improve the survey in both shallow and deeper regions and to gain adequate resolutions, we chose 2 frequencies: 80 MHz and 200 MHz, respectively. More specific parameters are described in Table 3.6.

Fig 3.6c presents the best processed results of GPR measurements along A-A' transect, with frequency of 200 MHz and velocity = 0.125 m/ns. Although the delineation of the layer sequence is not favorably distinct, the profile resolves to a depth of 15 m. When compared against the borehole data, the obscure area between elevation 28 m to 30 m and below elevation of 22 m correlate with gravel formation while the formation in-between with comparatively clear reflecting signals is sand. The shallow surface above elevation of 30 m should be sand formation as well, which is illustrated by another sharply slender band zone. The fading out of signals in the upper region suggests the occurrence of different saturated conditions among this layer. Additionally, because this layer is followed by gravel formation, the abrupt appearance of a thin zone could imply the contrast effect of material interfaces, or the existence of the water table.

## Chapter 4

# Data processing

The chronological data collected about a period of 2 years yield abundant information on local ground deformations and hydraulic activities. However, some external effects, appearing occasionally or persisting for some periods are observed in the signals as noise. Other signals induced by particular processes were also noticed. Therefore the original data are processed as time series and parts of the data were filtered out for specific reasons. More details about the data processing will be described in the following paragraphs. The results of the NE flank have not been included in the analyses as data collection is still on-going. They will be incorporated once sufficient amounts of data are collected (see Section 6.2.2 and Appendix D). The water table data for the similar period of time is also attached in Appendix E.

### 4.1 Tilt signal

The original data indicates that the in-situ tilt signals are basically influenced by several hydraulic and meteorological factors (Fig. 3.4). With respect to their characteristic persistence or frequency, those signals are grouped and analyzed according to the following categories: general migration signals or event-type signals.

The type of general migration signals indicates the chronic tilting trend within short-term or long-term time frames. They may be associated with daily, seasonal or annual variations of ground deformations. Event-type signals, on the other hand, reflect movements induced by specific incidents of comparatively more irregular occurrence. These are generally related to non-periodic hydraulic or meteorological factors. Among them, varying pore pressure gradients due to changing pumping rates are the most relevant influences in this study. These are discussed in greater detail in the subsequent 2 sections.

Figure 4.1 shows some monthly results of general migration tiltmeter signals. The locations F3, F22 and F31 represent the West, NW and North flanks, respectively. The data illustrate the variations in X-axis, Y-axis and instrumental temperature. In the diagrams, most tilt signals have a saw-toothed pattern with daily period. On a long term scale, an upward or downward trend is observed. Similar trends are also seen in

the recordings of instrument temperature.

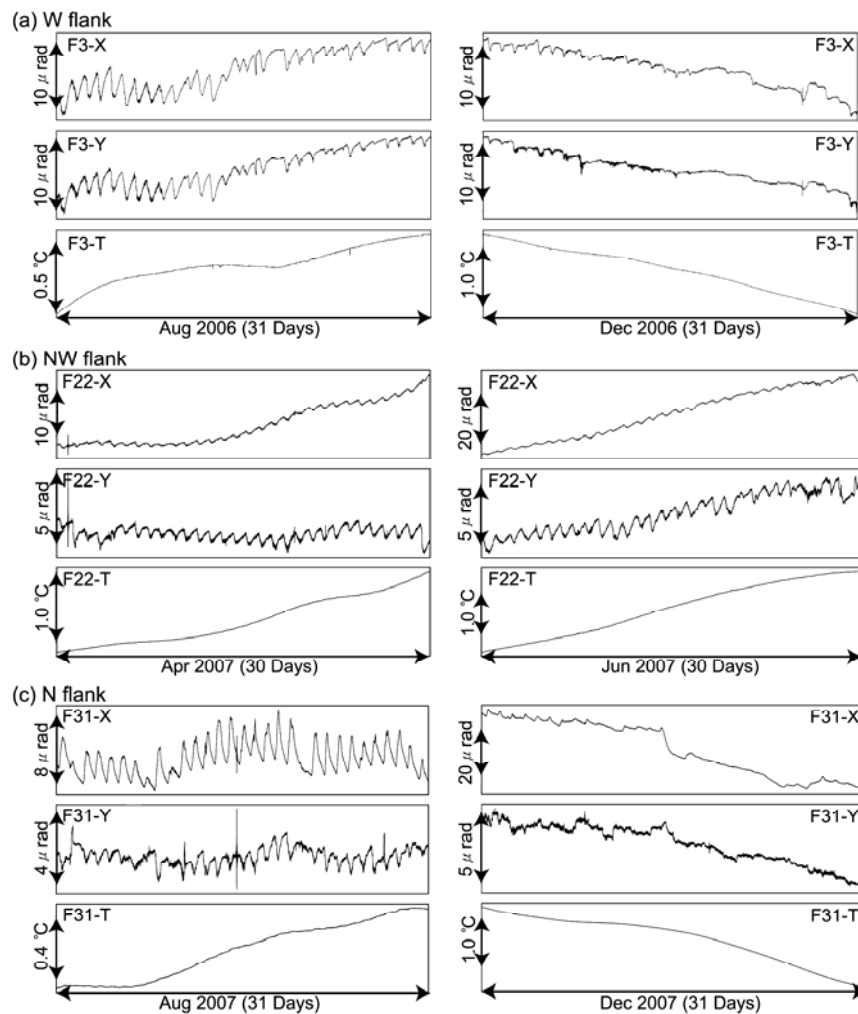


Fig. 4.1 Monthly general migration signals in different seasons. The results of X-, Y-axis and instrument temperature at location (a) F3 (West flank) in August/summer and December/winter, (b) F22 (NW flank) in April/spring and June/summer, and (c) F31 (North flank) in August/summer and December/winter are shown.

As for the daily undulations in the signals, we may note that throughout the day, soil temperature and barometric pressure are strongly influenced by the warming effects of the sun, as are the consumption requirements of vegetation. Those interactions are believed to trigger the diurnal variations and the characteristic saw-toothed patterns. Such tilt responses are suggested to be indicative of mechanisms underlying thermoelasticity and/or poroelasticity (Kümpel, 2001).

The amplitude of the diurnal variations appears to be related to seasonal changes.

Stronger fluctuations occur more frequently in summer time (June/July/August) than in other seasons. For instance, the maximum amplitude is 8.5  $\mu\text{rad}/\text{day}$  and 2.5  $\mu\text{rad}/\text{day}$  at location F3; 2.5  $\mu\text{rad}/\text{day}$  and 1.0  $\mu\text{rad}/\text{day}$  at F22; 7.0  $\mu\text{rad}/\text{day}$  and 2.0  $\mu\text{rad}/\text{day}$  at F31, for data collected in summer and winter/spring, respectively (Fig. 4.1).

If longer data sets (such as half a year or more) are considered (Fig. 4.2), the general migration signals show an increasing or decreasing tendency, whereby the curves do also encounter a turning point. Turning points normally appear during summer and winter, so that the long-term trends occur in the shape of a concave or convex parabola or a side of parabola.

In Fig. 4.2, the W flank (F1-F4, F7-F14) was monitored for the longest period (10 months) so that most locations along this flank present themselves as a more complete parabola-formed curve. On the other hand, the NW flank (F5-F6, F15-F23) was monitored for a relatively short period of 4 months and most of its variations reveal only a partially parabola-like trend. Variations in the N flank (F24-F33), despite being monitored only for half a year, already exhibit the form of a parabola trend. F1 and F6 have the longest series as they have been used as reference locations.

The total amplitudes of the annual variations are deduced from the highest and lowest points of the parabola. The difference between these 2 points usually falls within 50  $\mu\text{rad}$ . The smallest value is less than 20  $\mu\text{rad}$ ; the largest value is more than 100  $\mu\text{rad}$ . These amplitudes are seen at locations F4, F6, F23, F24, F25, F31, and F32.

As mentioned, the greatest probability for the occurrence of these points is during the summer and winter season, i.e. corresponds to months with the highest and lowest temperature. That is, the long-term general migration signals and the instrument temperature correlate well with these seasonal alternations. Accordingly, the general migration signals have a strong dependency on thermal effects.

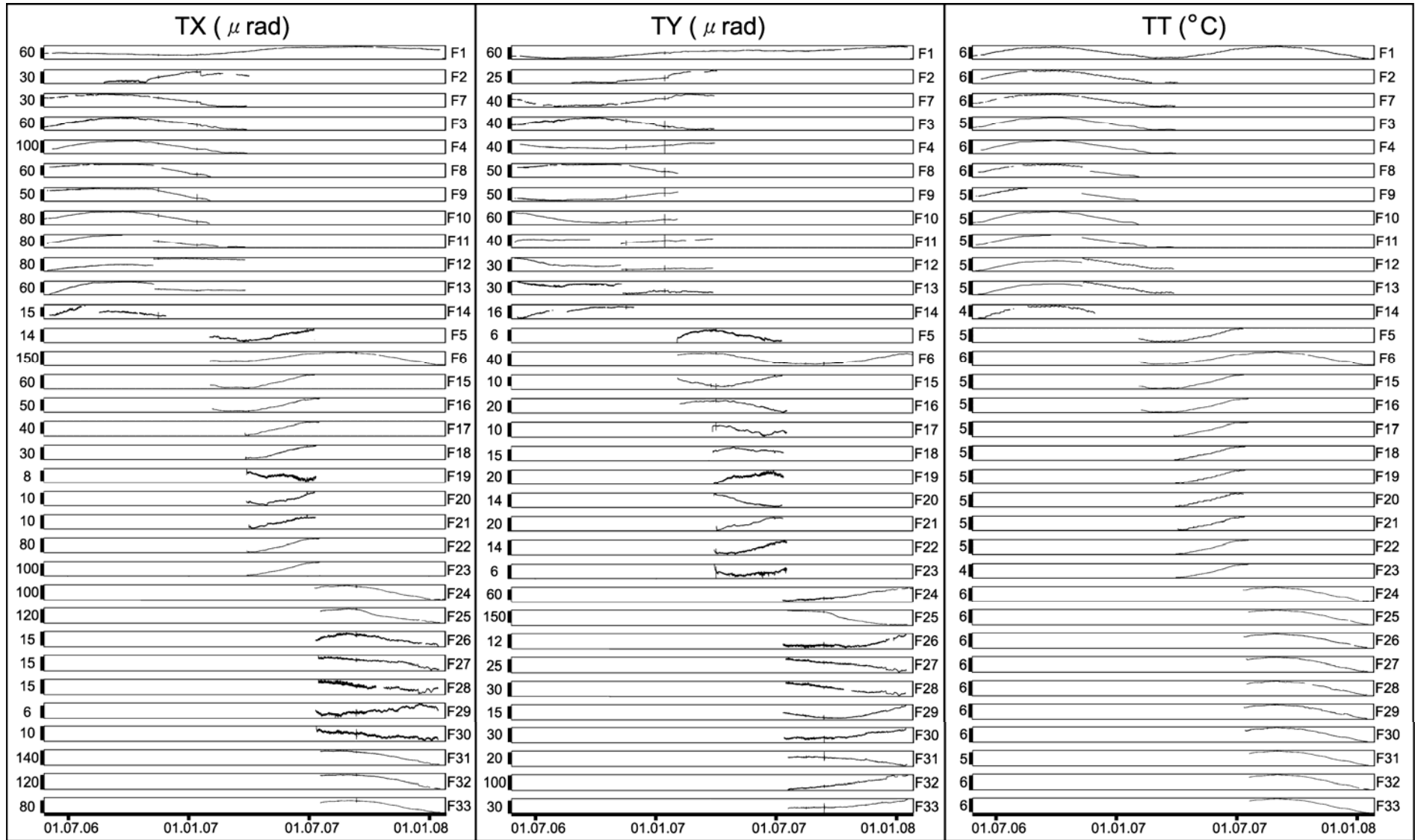


Fig. 4.2 Long-term variations of general migration signals (X-, Y-axis and instrument temperature) for each tiltmeter location. Numbers left to the diagrams indicate full range in  $\mu\text{rad}$  or  $^{\circ}\text{C}$ .

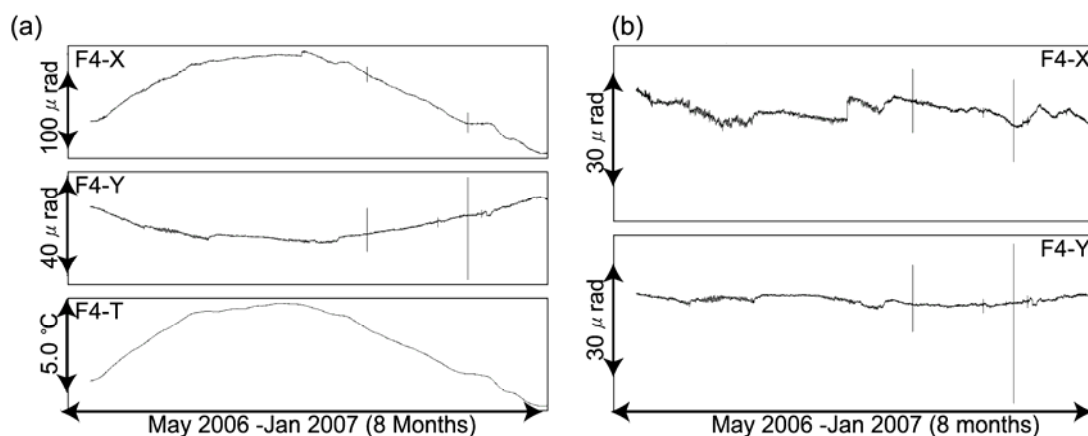


Fig. 4.3 (a) Location F4: long-term general migration signals of X-axis, Y-axis and instrumental temperature. (b) Removal of temperature effect for long-term general migration signals.

The temperature effect can be largely reduced by multilinear regression. Figure 4.3 shows results from location F4 as an example. It illustrates that thermal effects have a significant influence on signals. Removal of the temperature effect leaves a trend that can be approximated by a linear function.

The itemized information about the long-term migration signals in the form of differences in the X-axis and Y-axis is shown in Table 4.1. In principle, when the difference of tilt of the X-axis ( $\Delta\text{TX}$ ) or Y-axis ( $\Delta\text{TY}$ ) is divided by the difference in temperature ( $\Delta\text{T}$ ) during a certain time frame, this ratio is named the temperature factor (Tf.; eq. 4.1).

$$\text{Tf.} = \frac{\Delta\text{TX}}{\Delta\text{T}} \text{ or } \frac{\Delta\text{TY}}{\Delta\text{T}} \quad (\text{eq. 4.1})$$

This ratio reflects the impacting degree from the temperature effect (a larger number means a greater influence). Sometimes it can be flexibly modified or omitted to show a better linear function. A positive value is indicative that the variations of X-axis migrate towards to the East and Y-axis towards to the North when an increase in temperature occurs. On the contrary, negative shows a decrease in temperature when X- and Y-axis are still towards to the E and N, or they towards to opposite direction: W and S when an increase in temperature. Thus, to obtain the linear



function, the factor is required to be reduced for the trend of X-axis or Y-axis signals with a positive value, and be added to compensate the trend of X-axis or Y-axis signals for a negative value, respectively.

Loc.	TX	Tf.	TY	Tf.	Loc.	TX	Tf.	TY	Tf.	Loc.	TX	Tf.	TY	Tf.				
<b>W flank</b>					<b>NW flank</b>					<b>N flank</b>								
<b>F1</b>	32		40	-6	<b>F5</b>	15	3	7	-1	<b>F24</b>	104	16	70	-10				
<b>F2</b>	30	-6	28	-5	<b>F6</b>	93	15	36	-7	<b>F25</b>	115	16	185	30				
<b>F7</b>	35	7	40	-8	<b>F15</b>	63	13	13	3	<b>F26</b>	13	2	10	-2				
<b>F3</b>	60	12	44	9	<b>F16</b>	59	12	21	-4	<b>F27</b>	13	2	24	3				
<b>F4</b>	105	20	18	-3	<b>F17</b>	49	10	9	-2	<b>F28</b>	9	2	26	-2				
<b>F8</b>	15	55	3	20	14	34	3	10	<b>F18</b>	31	6	5		<b>F29</b>	13		13	-4
<b>F9</b>	10	50	2	13	10	26	-2	-6	<b>F19</b>	9		20	2	<b>F30</b>	7	1	20	-3
<b>F10</b>	75	13	50	-10	<b>F20</b>	11	2	13	-2	<b>F31</b>	125	16	19	3				
<b>F11</b>	65	50	13	10	12	20		-4	<b>F21</b>	9	1	19	3	<b>F32</b>	103	15	96	-8
<b>F12</b>	45	10	9		22	4	5		<b>F22</b>	80	16	12	2	<b>F33</b>	70	12	18	-3
<b>F13</b>	80	10	16		16	10			<b>F23</b>	108	22	6						
<b>F14</b>	17	10	5	5	8	6	3	3										

Table 4.1 The optimal temperature factor for each location. See text and eq. 4.1.

At locations F8, F9, F12 and F13, data are not continuous because the instruments at these locations were interchanged in order to determine the resolution of different tiltmeter types. Similar breaks exist at locations F11 and F14, yet due to instrumental malfunction requiring inspection and repairs. In all, the temperature factor can be calculated separately for the periods before and after the time gap, if necessary.

The results of general migration signals can also be illustrated as hodograms (Fig. 4.4), which display the overall drifting variations in 2-D. The scale bar for all locations in Fig. 4.4 is 250  $\mu$ rad for both X- and Y-axis. The black curve with sequence of monitoring months is the hodogram, and the red arrow with numbers in  $\mu$ rad unit indicates the variation of the hodogram orientation. The general orientations at most locations are in the NW-SE direction while a substantial subset of the others inclines toward NE-SW direction. The most prevalent rate of this type of tilt signals is 15  $\mu$ rad/month. However, at locations F1, F5, F12, F13, F14, F29 and F30, the rate was below 5  $\mu$ rad/month and at locations F25 and F23 exceeded 30  $\mu$ rad/month.

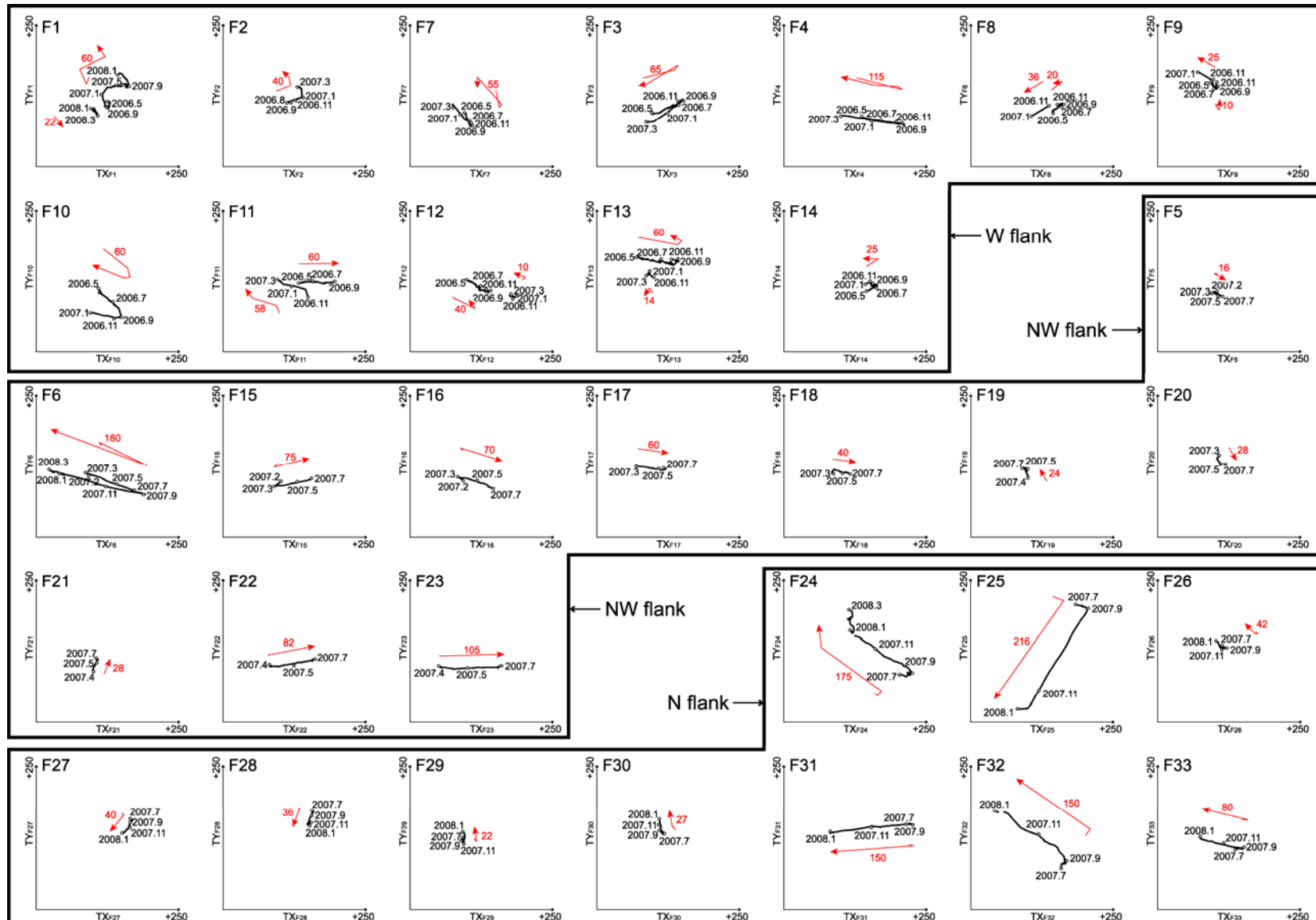


Fig. 4.4 Hodograms of general migration signals with time sequences at different monitoring locations (F1-F33). All scales of the X- and Y-axis in hodograms are the same (250  $\mu\text{rad}$ ). The red arrows indicate the migrating directions, and the red numbers give the total magnitude in  $\mu\text{rad}$ .

The cyclicality of the trend is best seen by the hodogram of location F1 which has been continuously monitored for almost 2 years. The mechanism of the migration signals remains unclear. In principle, it could be ground deformation or a temperature effect. When the temperature factor is considered, the total amounts of the variations are often greatly decreased.

## 4.2 Water table variation

Changes of pore pressure gradients constitute one of the most important factors generating tilt signals. As variations of pore pressure gradients are reflected in the height of the water table, if unconfined, monitoring water table variations can yield meaningful information regarding local hydraulic conditions and parameters.

The chronological data of water table variations obtained over a period of 16 months starting in November 2006 is shown in Fig. 4.5. Vertical dashed lines in the graph are drawn every 4-months. Compared to the initial variation patterns of water levels (see Fig. 3.4), the present dataset is rather consistent apart from some small instrumental defects resulting in a lower value recorded in W1 (indicated by the circle) and some short time intervals of missing data (evident as breaks in the curves) in most observation wells.

The average height of the water table is normally between 28.5 m to 29 m above sea level. Only W4 presents a value of 0.3 m higher than the others. Also, two unusual shark fin-shaped zones occurred, indicated by two arrows (Fig. 4.5). Thus, the local hydraulic system remains at a relatively steady state except when the water level in a fin-shaped kind rises smoothly with a height difference of 1 m to 1.5 m within a few weeks. This latter phenomenon indicates the occurrence of water recharge events with large quantitative variations.

In fact, the first example of the water table increase is caused by an accidental leakage of the neighboring transport tubes while the second is due to routine cleaning of the central pit and its 8 horizontal wells (Fig. 4.5, 1<sup>st</sup> arrow). When these events occurred, the regular pumping operations of the central pit were shut down (meaning that the maintenance of minimum pump rate of 300 m<sup>3</sup>/h was halted for the activities) which resulted in the rising of the water level. Once the regular pumping operations

were reactivated, the water level dropped abruptly and subsequently fluctuated gently back to the average value. For some unknown reasons, the new average of water level appears to be about 0.5 m higher than that before the leakage accident.

The fluctuations of water table are mainly generated by the alternating activation of two pump heads. Regardless of which pump head is in use, when the pump rate changes exceed  $300 \text{ m}^3/\text{h}$ , small fin-shaped perturbations in the water level curves can be observed, such as the one (shortly before the 2<sup>nd</sup> arrow) occurring before the recommencement of the regular cleaning procedure. However, if the change in pump rate lasts less than a day, due to the time scale of the diagram in Fig. 4.5, the fin-shaped character of the water table variations can hardly be seen. The signals become merely vertical lines as indicated by the two star symbols. Yet, the water table variations appear wave-like if viewed on short scale. A smaller time scale is in fact required to examine the signal correspondences and interrelations.

Figure 4.6 illustrates an example of water table results viewed on a narrower time-scale. The results were obtained from selected weekly data to represent differences in water table fluctuations corresponding to different seasons: winter, spring, summer and autumn, respectively. Data for most seasons shown are from consecutive 3 months intervals apart from the data for autumn. Because the instrument in well W1 encountered a recording problem in October 2007, data from a month later were used instead. The scale of each diagram is identical in that the water table above sea level is on the left side with 0.75 m total range and pump rate on the right side with  $400 \text{ m}^3/\text{h}$  total range.

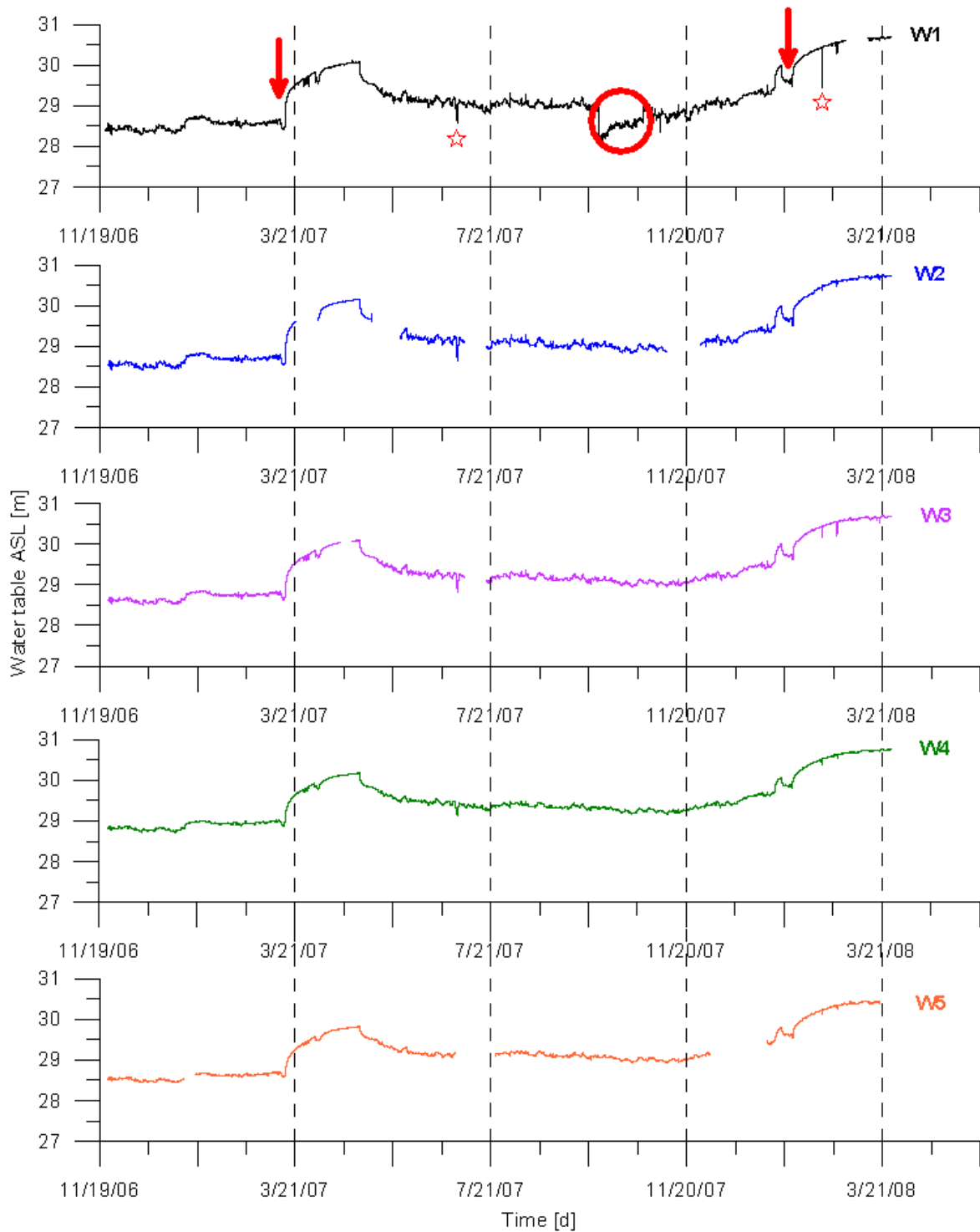


Fig. 4.5 Variations in the water table height of the 5 monitoring observation wells (W1-W5). The fluctuations are quite steady with some exceptions; the arrows mark the cessation of pumping and the stars indicate pump rate changes greater than  $300 \text{ m}^3/\text{h}$ . The circled area could display an instrument defect.

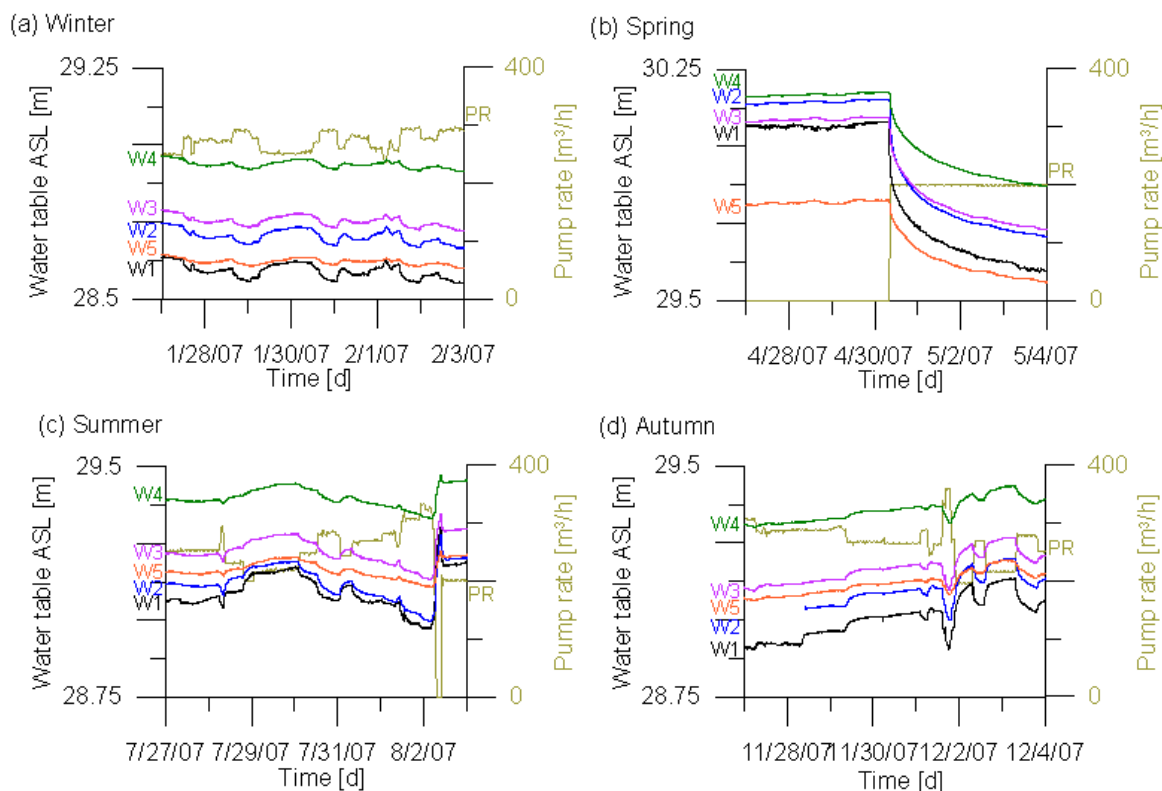


Fig. 4.6 Water table variations in 5 observation wells (W1-W5) compared with the pump rate operations (PR) in different seasons: (a) winter, (b) spring, (c) summer, and (d) autumn.

Figure 4.6 shows that the water table fluctuations in the 5 observations wells (W1-W5) vary exactly at same instants as the pump rate: the elevation of the water table rises while the pump rate decreases and vice-versa. Some rather fluctuating curves and small fin-shaped variations of the water level related to small quantities (ca. 100 m<sup>3</sup>/h) in pump rate changes are also observed. In general, the pump rate is maintained at an average of 300 m<sup>3</sup>/h. The exception was observed in spring 2007 due to a leakage accident (Fig. 4.6b). The average elevation of the water table was lowest (around 28.5 m) in winter of 2007 and highest in spring (around 30.1 m). During this period, zero pump rate was recorded which as previously mentioned, was caused by the cessation of central pit operation due to the leakage accident. This resulted in the rising of the water table. Without pump operation, the elevations of the water level would eventually have become equalized after long pause. Whereas W1 to W4 have similar values of the water level with minimal standard deviation ( $\pm 0.06$  m), W5 was an exception. In subsequent seasons of summer and autumn, regular pumping

operations recommenced and the pump rate was maintained rather constant. Consequently, the elevations in summer and autumn dropped to around 29.25 m and 29 m, respectively.

Comparing the results obtained under the condition of regular pumping, such as Fig. 4.6a, c and d, the average water level from different observation wells differs slightly and the elevation at W1 is usually the lowest while the one at W4 is highest. This is related to the distance between the central pit and the locations of the observation wells (i.e. the longer the distance, the higher the elevation). However, the results at again W5 did not follow this trend and varied irregularly with its level being mostly at the middle of the range observed and occasionally at the lowest position.

To understand the general drawdown situation induced by pumping, the midnight recordings from the 30<sup>th</sup> of each month from the different seasons in Fig. 4.6 is selected. Using the coordinates and the values of the water level from the 5 observation wells, a 3-D topographic visualization for the general drawdown distribution is created (Fig. 4.7). The values of the color scale bar are not identical for each season because the ranges of water table variations differ. However, each tick on the scale bar represents the same interval of 0.1 m.

Gradient changes away from the central pit do not increase evenly. A long edge sometimes develops inclining to the west (W2) or northeast (W5) and the gradient changes of the water level are slightly higher at the south (W4) than at the north (W3) while small high apices develop near W 3 and W4. However, most of the results indicate a flow focusing close to the center. The drawdown appears to be funnel-shaped: the base of funnel is located at W1 (which is the closest location to the central pit) and the edge spreads gently out to other observation wells.

The funnel-shaped appearance of the drawdown is no longer observed in spring when pumping operations ceased. The water level rises in all observation wells and nearly reaches identical levels. Nevertheless, some indications remain which suggests highest well levels at W3 and W4, a slightly lower well level at W1, and the lowest water level at W5, respectively. These results verify that the local drawdown is generally associated with the pump operation in the central pit and the water table gradient is in the order of 0.001 (m/m).

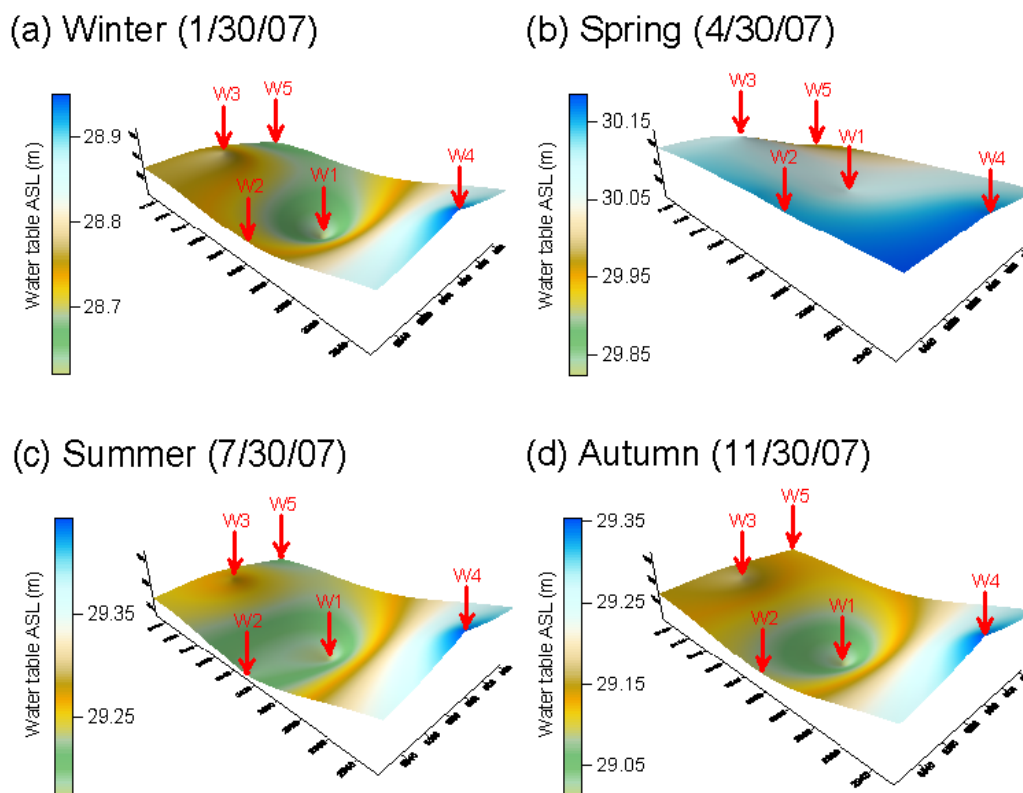


Fig. 4.7 Variations of general drawdown situations from 5 observation wells (W1-W5) in different seasons: (a) winter, (b) spring, (c) summer, (d) autumn.

### 4.3 Pump event

The results from the previous section clearly show that the changes in pump rate are the main factor contributing to water table variations. Since changes in pore pressure gradients are known to induce tilt signals and near-surface movements, the effects in changes of pump rate are inevitably significant. It is important to establish a criterion to evaluate the changes in pump rate in order to explore quantitatively the monitored data and to deduce representative results for ground deformations. Observations suggest that either the pump rate decreases (injecting appearance) or increases (enhanced withdrawal). When the change in rate exceeds  $100 \text{ m}^3/\text{h}$ , a distinct tilt signal is recorded. Thus, data were selected according to this criterion, and these pump induced signals are categorized as event-type signals, discriminating them from the general migration signals. Additionally, the occurrence of the  $100 \text{ m}^3/\text{h}$  pump rate changes is denoted as a pump event.

In general, the frequency of the pump event is slightly related to seasonal



changes. In the periods of spring (March/April/May) and summer, pumping events were more likely to take place and more than 20 pumping events were reliably recorded. Indeed, an extraordinarily high frequency of 14 pumping events per month was observed in the summer of 2006. This number decreases significantly to between one to five per month in autumn (September/October/November) and winter.

<b>W flank</b>	<b>F1</b>	F2	F7	F3	F4	F8	F9	F10	F11	F12	F13	F14
Pumping event (numbers)	120+	18	39	59	57	43	55	45	50	47	47	43
	2006 Summer: 41 / Autumn: 14 / Winter: 4											
<b>NW flank</b>	F5	<b>F6</b>	F15	F16	F17	F18	F19	F20	F21	F22	F23	
Pumping event (numbers)	40	62+	40	42	33	29	27	27	25	29	29	
	2007 (Winter:4) / Spring: 25 / Mid Summer: 13											
<b>N flank</b>	<b>F24</b>	F25	F26	F27	F28	F29	F30	F31	F32	F33		
Pumping event (numbers)	22+	19	22	20	18	22	22	20	19	20		
	2007 Late Summer: 11 / Autumn: 6 / Winter: 5											

Table 4.2 Total amounts of pumping events occurring at different monitoring locations along each flank of the horizontal well, and listed in context of the recording seasons. The W flank has longest monitoring durations while the N flank has shortest. The instruments at F1, F6 and F24 were not replaced so that their counting numbers are with a (+) sign.

Table 4.2 shows the total amount of the pump events during the seasonal alternations and the ones at different monitoring locations during these time frames. The largest number of pump events along one flank of the horizontal well normally equals to the sum of events from each monitoring duration, i.e. 59 pump events are observed at location F3, and the sum of the pump events during monitoring durations along the W flank also equals 59. Besides, monitoring at F5, F6, F15, and F16 started earlier than the others along the NW flank in the winter of 2006. The recording duration overlap at the W flank, therefore a bracket was used to indicate it. Moreover, F1, F6 and F24 are in bold character and the amounts of pumping events have a plus (+) sign to indicate their continuous monitoring since the tiltmeters were installed at these locations.

Monitoring durations of half a year or longer were spent on the W flank, so that the largest number of pump events (close to 60 times) was collected. The monitoring periods were shortened when the tiltmeters were relocated along the NW flank and the N flank because the numbers of pump events already exceeded 15 and were sufficient to distinguish the results of tilt azimuths and amplitudes induced by pumping operations. This criteria number is much easier to be fulfilled in spring and summer time, which suggests that these are excellent times for data recording and instrument relocating at this site.

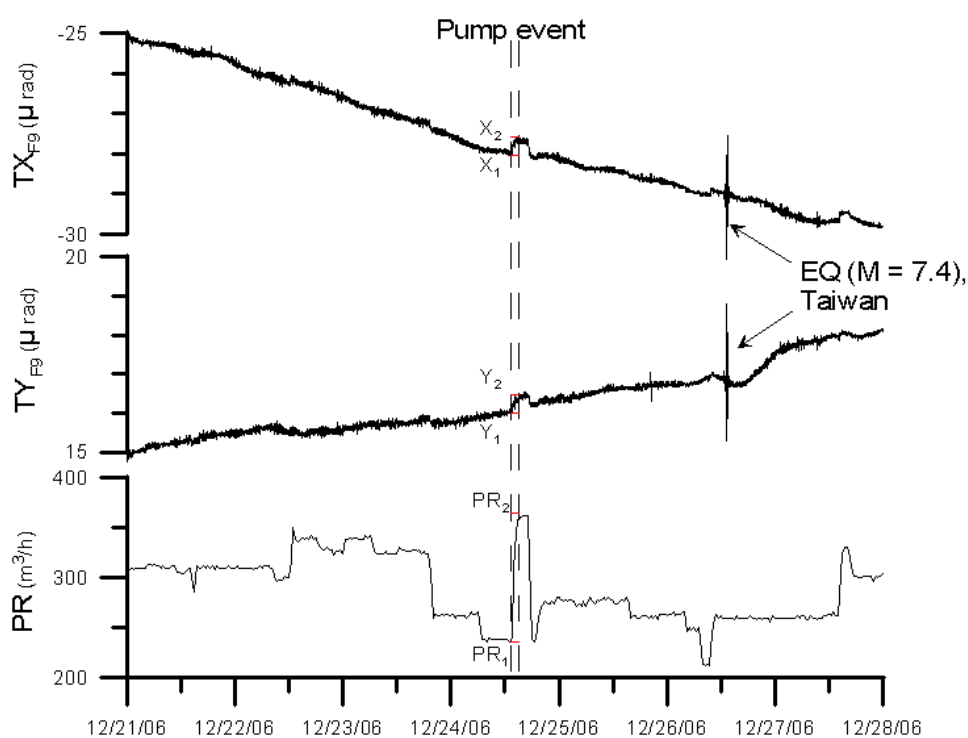


Fig. 4.8 A selected example of tilt signals in X- and Y-axis at location F9 induced by a pump event. ( $X_1$ ,  $X_2$ ,  $Y_1$ ,  $Y_2$ : induced signal in X- and Y-axes;  $PR_1$ ,  $PR_2$ : pump rate)

Figure 4.8 shows a typical pump induced signal with distinct variations in X- and Y-axes corresponding to changes of pump rate at location F9. The variations can be quantified using the following formulae:  $\Delta X = X_2 - X_1$ ,  $\Delta Y = Y_2 - Y_1$ , and  $\Delta PR = PR_2 - PR_1$ . From the calculated values of  $\Delta X$  and  $\Delta Y$ , a linear function with 0 intercept can be deduced. The arc tangent value of the linear slope ( $r$ ) stands for the apparent azimuth ( $\theta_a$ ) indicating the angle induced by the pump event. Using the difference between the apparent azimuth and the radial orientation ( $\theta_r$ ) of the tiltmeter locations

to the central pit, the true azimuth ( $\alpha$ ) is calculated (eq. 4.2).

$$\alpha = \theta_a - \theta_r = \tan^{-1} r - \theta_r \quad (\text{eq. 4.2})$$

$$\text{, where } r = \frac{S_{\Delta X \Delta Y}}{\sqrt{S_{\Delta X \Delta X} S_{\Delta Y \Delta Y}}} = \frac{\Delta X_1 \Delta Y_1 + \dots + \Delta X_n \Delta Y_n}{\sqrt{(\Delta X_1^2 + \dots + \Delta X_n^2)(\Delta Y_1^2 + \dots + \Delta Y_n^2)}} \quad (\text{n = last data set number})$$

If a graph is plotted, setting the X-axis as  $\Delta PR$  and the Y-axis as the value of the square root from the sum of  $(\Delta X)^2$  and  $(\Delta Y)^2$ , the amplitude corresponding to the magnitude induced by pump event can be estimated using linear regression analyses. Figure 4.9 illustrates the results of the induced azimuths and amplitudes according to each monitoring location and its corresponding type of tiltmeter. The direction of the arrows indicates the azimuth; the length is proportional to the amplitude; the units are degree and  $\mu\text{rad}$  per  $100 \text{ m}^3/\text{h}$  of pump rate changes, respectively. When the azimuth has a positive value, the deviation of the azimuth presents an anticlockwise rotation away from the radial orientation and vice versa.

The results can be analyzed in two ways. First, the screen sections of each tube flank are used as different standard positions. When the orientation facing the central pit is taken, the azimuths of right-sided tiltmeters should present a positive sign while the left-sided group should have a negative sign. The amplitude of both sides is expected to be symmetrical. A larger amplitude with little azimuth deviation is expected for the tiltmeters situated right above the screens (F10, F21, F30).

Second, all tiltmeter positions were arranged in form of a loop, so that all rows and lines along different tube flanks can be compared. The lines are distributed laterally away from section screens as the rows are distributed perpendicularly to section screens (Table 3.1 and Fig. 4.10). The azimuths of tiltmeters on the lines in Fig. 4.9 show a trend namely the closer to the screen section, the larger is the absolute azimuth value of the tilt signal. The results on the middle part of the lines have an opposite trend that a greater absolute azimuth value appears on the farer line to the screen section. A similar trend is observed in the amplitude results of the tiltmeters, but the results of the monitoring locations near the boundary area between two adjacent tube flanks are slightly controversial. A rising value may appear on the line furthest away from screen section.

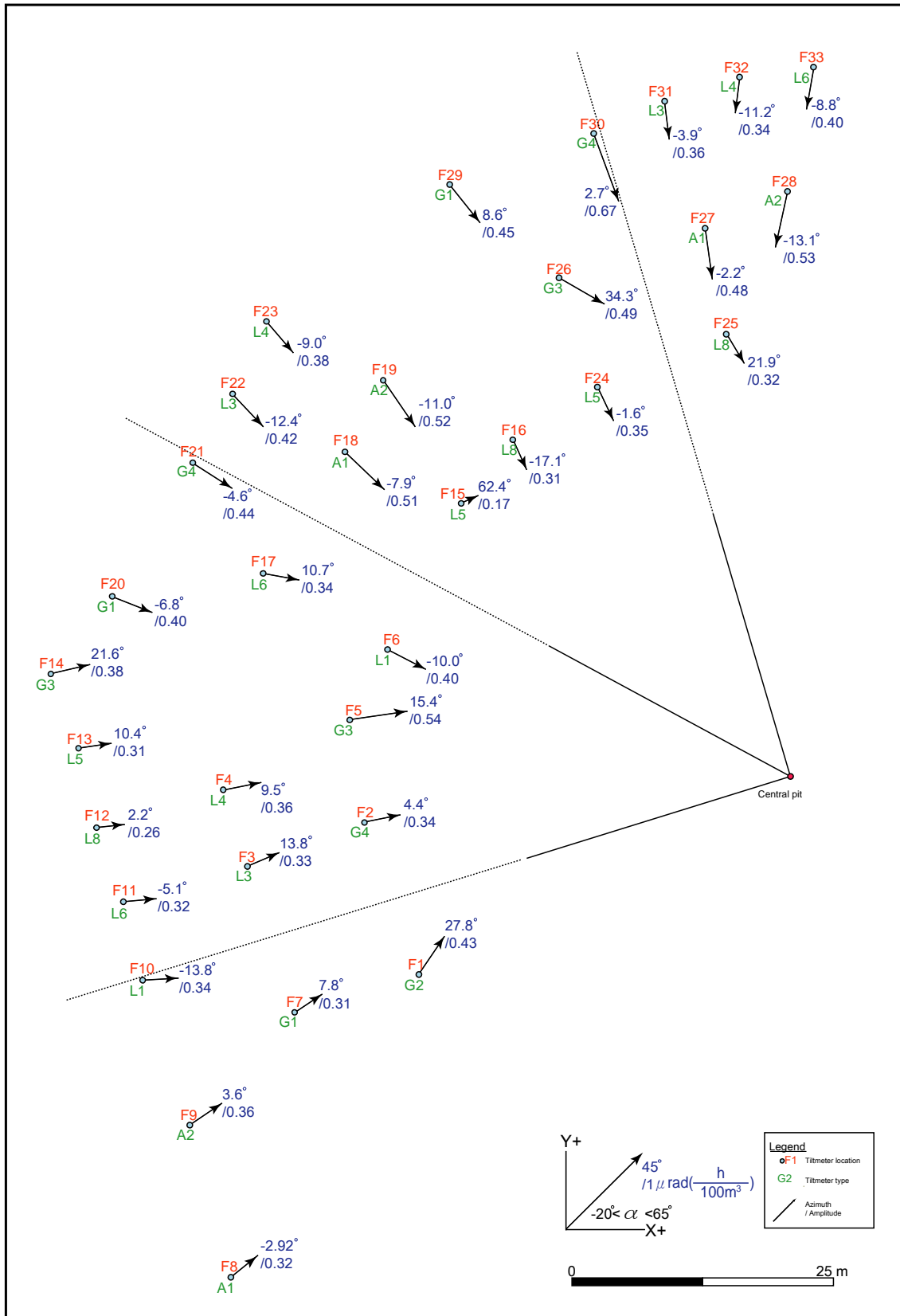


Fig. 4.9 Tilt azimuths and amplitudes induced by pump events for all locations. The direction and the length of each arrow represents the azimuth (in degree) and amplitude (in  $\mu\text{rad} \cdot h/100\text{m}^3$ ), respectively.

In addition, another view for rows; the azimuths of tiltmeters on the 1<sup>st</sup> and 3<sup>rd</sup> row show a rather disperse range of results that is the absolute value of azimuth could be comparatively higher than 20° or lower than 5° while it has an average value around 10° on the 2<sup>nd</sup> row. The tendency indicates that an increasing distance away from the central pit would matter slightly, so that the values of azimuths decrease from the 1<sup>st</sup> row to the 3<sup>rd</sup> row, but sometimes a larger value appears on the 2<sup>nd</sup> row instead of on the 1<sup>st</sup> row. The amplitudes have a similar tendency; a larger value of amplitude exists on the locations of the 1<sup>st</sup> row or 2<sup>nd</sup> row, where are closer to the central pit compared with the 3<sup>rd</sup> row. The range of most amplitudes is from 0.3 to 0.4  $\mu\text{rad} \cdot \text{h}/100\text{m}^3$ , yet the value sometimes increases to 0.5  $\mu\text{rad} \cdot \text{h}/100\text{m}^3$  that is for the locations on the 2<sup>nd</sup> row of the NW and N flank.

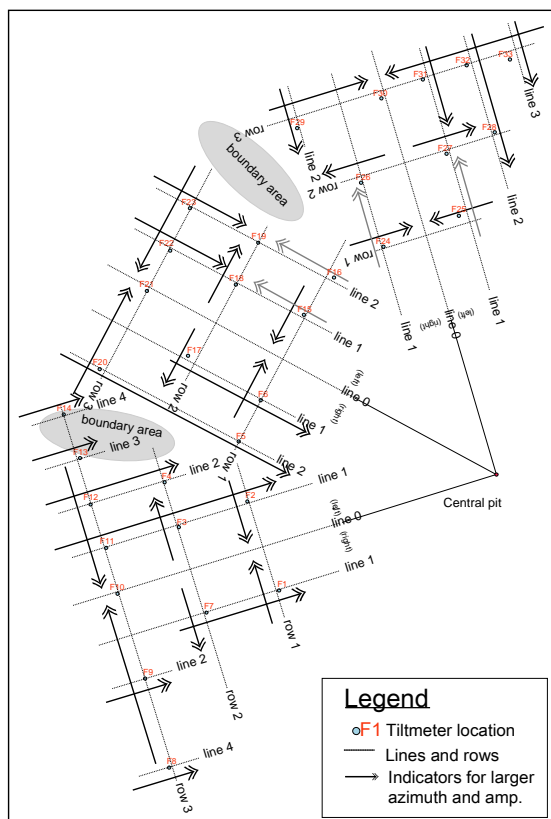


Fig. 4.10 Tiltmeter arrays and their corresponding signal distribution.

Figure 4.10 shows the configuration of the lines and rows and the distributing tendency of data variations which are mentioned above; the arrow points to a larger azimuth and amplitude. From these results, the trends of pump induced azimuths generally point to the central pit and are slightly parallel to the orientation of the transport tube. The absolute value of the azimuth is positively related to the radial distance of the screen section of flank tube and central pit, showing where the tiltmeter locates would matter to its induced signals. That the difference of results between different rows seems to be larger than the one between different lines may imply that the major influential force

comes from the central pit, although the screen section also contributes to the ground deformations. Further, when close to the boundary area, some convergent boundaries may exist, where the results are influenced by two adjacent flank tubes.

Some results appear to be contradictory and disobey the general trend described above at some locations: F2, F3, F10, F25 and F31 are anomalous in azimuth; F9 in amplitude; F5 and F15 are anomalous in both. This might indicate certain local inhomogeneous conditions in the subsurface. Some underground structures have been verified by the preliminary geophysical surveys. This will be alluded to in the chapter discussion. Overall, the results of azimuths indicate that the deviated angle from its radial orientation to the central pit generally falls within  $10^\circ$  and in some cases by more than  $20^\circ$ . The average tilt amplitude is  $0.33 \mu\text{rad}$  in response to  $100 \text{ m}^3/\text{h}$  change in pumping rate along the screen section of the west flank, and is up to  $0.4 \mu\text{rad} \cdot \text{h}/100\text{m}^3$  on the NW and N flank.

Concerning the water level, the variations induced by pump events are observed as well, but the response duration of the signals lasts clearly longer and requires more time to return to equilibrium status than for the in tilt signals. Normally, an interval of a few hours is considered sufficient to obtain the result in water table variations related to pump rate changes (Fig. 4.6), while a period of a few minutes is the relatively instantaneous response in tilt signals (Fig. 4.8). Therefore, for analyzing typical response in water table variations induced by pump events, a restriction for the response duration is set. When the variations of the water table respond to each pump event within up to 3 hours, the samples are selected.

Figure 4.11a shows the results of water table variations one hour after different pump rate changes ( $\Delta\text{PR}$ ) have been conducted; the locations of the observation wells are marked. Contour lines have been calculated from only the water level changes in these wells. Each bold line represents 0.01 m increment in water level change, when the value of the contour increases, e.g. from -0.05 m to -0.04 m or 0.1 m to 0.2 m, the area of the contour becomes lighter and lighter. Two examples when the pump rate change is positive are given (Fig. 4.11a, two left panels). The variation values of water level are negative and descend more close to W1, so that the color of the contour fades from inside to out. From these two diagrams, the quantity of pump rate changes differs largely so that the spacing from two bold contours in each appears greatly different. If the same distance is taken, such as the distance between W1 and W2, the bold lines plot at least 3 times denser in the 2<sup>nd</sup> diagram than the first one, indicating

the increment of water table variation is 3 times larger for the same distance.

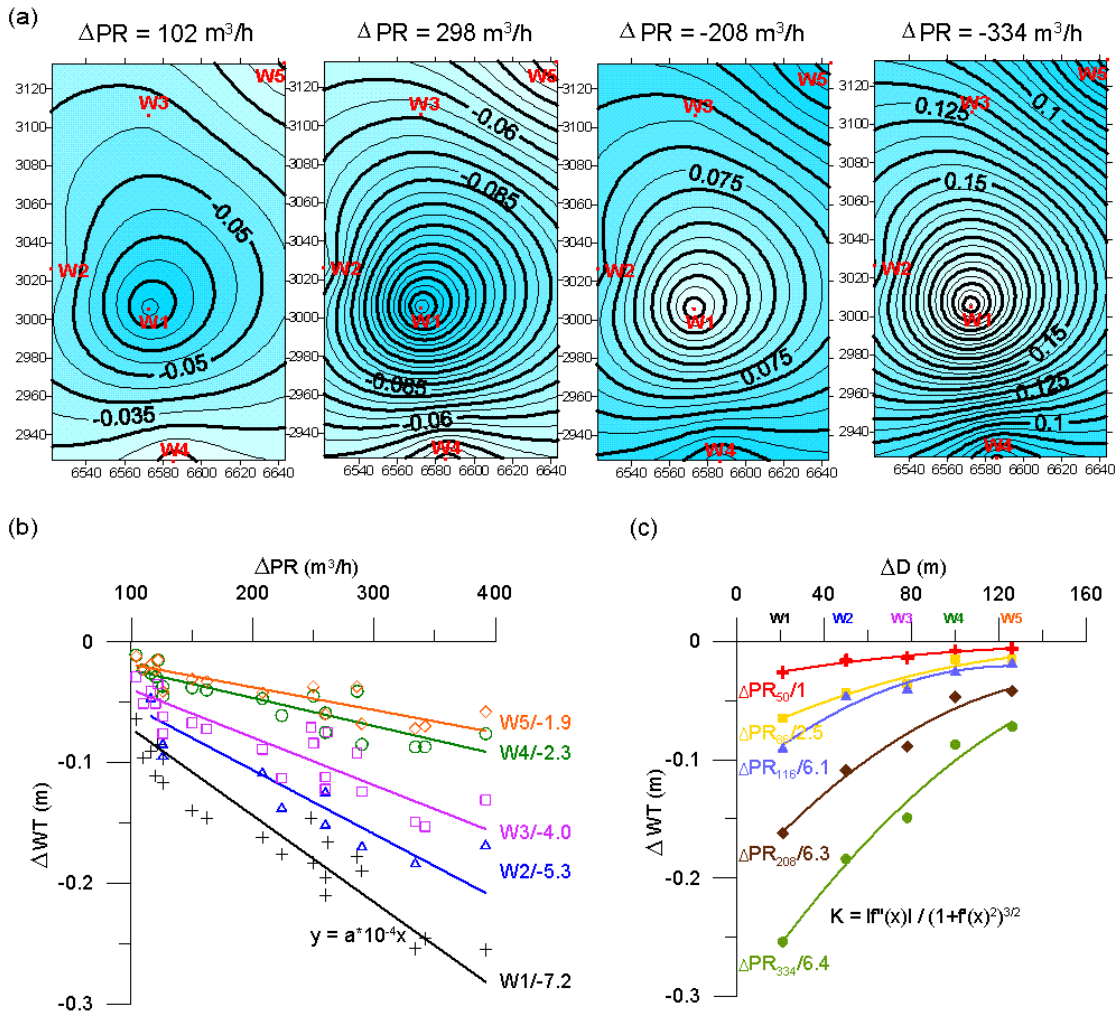


Fig. 4.11 The water table changes induced by pump rate changes ( $\Delta PR$ ). (a) Contours of water table variations extrapolated from different observation wells (W1-W5). (b) Relations between pump rate and water table changes ( $\Delta WT$ ). Each line symbols for each well (e.g. W1), and the number, i.e. a, multiplies by  $10^{-4}$  equals to its slope of the linear function. (c) Relations between the distance ( $\Delta D$ ) from each well to the central pit and their induced water table changes. Each polynomial line is related to a different pump rate, give, as index, e.g.  $\Delta PR_{50}$  in  $\text{m}^3/\text{h}$ , and the number (1) indicates the curvature (K) of the line.

In contrast, injection operations (negative pump rate changes) occur in the 3<sup>rd</sup> and 4<sup>th</sup> diagram (Fig. 4.11a). The water level rises, the variations are positive and a larger increment appears near W1 so that the color fades from outside to inside. The

increments of water table variation in these two diagrams are not much different, because their pump rate changes differ little. This example also shows that larger pump rate changes cause more intensive water table variations. The increment of contours in the 4<sup>th</sup> diagram is about 1.5 times denser than in the 3<sup>rd</sup> diagram.

If the sign of pump rate is ignored (either pump or injection), the increment of water table variation is positively correlated with the pump rate changes, i.e. the contours in the 3<sup>rd</sup> diagram are about twice denser than in the 1<sup>st</sup> while the pump rate change is doubled; the 2<sup>nd</sup> and 4<sup>th</sup> diagram are almost equivalent in increment of contour and pump rate changes. Moreover, the absolute value of water table variation is largest at W1 and smallest at W5, indicating that the distance to the central pit matters. The contours around observation well W2 and W4 slightly cave in, which corresponds to the neighborhood of the West and South flank of screen sections, whether it implies these screen sections also have influences on the water table changes would be discussed.

Some quantitative relations between pump rate changes ( $\Delta PR$ ) and water table changes ( $\Delta WT$ ) are illustrated in Fig. 4.11b. A linear function can be deduced between the water table changes and pump rate changes. Each linear line stands for the results of one observation well, the number next to the well name (W1-W5) equals an algebraic parameter  $a$ , and  $a \cdot 10^{-4}$  represents the gradient of the line. When the line is steeper, the absolute value of the number is greater, revealing that if the same quantity of pump rate change is calculated, the induced water table changes at W1 are larger than at other locations.

A clearer picture about the relation between the locations of observation wells and their water table changes ( $\Delta WT$ ) is demonstrated in Fig. 4.11c. Two examples ( $\Delta PR_{50}$  and  $\Delta PR_{86}$ ) of lower pump rate changes which fall outside the criteria of a pump event are also chosen. The locations of the wells (W1-W5) are labeled along the X-axis to show their distance to the central pit ( $\Delta D$ ). Each polynomial line indicates the variation curve of water table changes induced by different pump rate changes;  $\Delta PR_{50}$  is related to 50 m<sup>3</sup>/h pump rate changes. The numbers next to the pump rate changes, denoted as  $K$ , are the curvatures of the polynomial line after Newton (Chapter 26, Arens et al., 2008).



In general, the shorter the distance to the central pit, the stronger is the change in water level. The relation between well locations and water table changes follows a polynomial function. The curved line indicates that the appearance of the water table changes takes the shape of a cone, similar to its drawdown distribution. The larger the amount of pump rate changes, i.e. the greater the expression  $K$  given in Fig. 4.10c, the stronger are the variations in water table change. Besides, the curvature  $K$  is similar from  $\Delta PR_{116}$  to  $\Delta PR_{334}$ , but the value in  $\Delta PR_{50}$  and  $\Delta PR_{86}$  is quite different from the others, implying that  $K$  changes little for a certain range of pump rate changes. To summarize, the water table changes are positively related to pump rate changes, and negatively to the distance to the central pit.

## **Chapter 5**

# **Model calculation**

Most in-situ recordings depicted in the last chapter revealed some heterogeneous situations. Using a numerical method, one can compare the differences between the actual values measured against theoretical predicted values. The progresses of the fluid flow and ground deformation can thus be illustrated using a numerical simulation model.

The POEL, program compiled by R. Wang using Fortran was chosen as the software for the simulation. The diffusion-deformation process in plane multi-layered half space poroelastic materials can be modeled. The geometry of the model can grossly be designed according to the field scenario; the parameters of the sediments are selected from some representative soil materials; the sources of the forces are differentiated into 4 types to approach an optimal model. According to the different model frames, the time-dependent variations in pore pressure gradients and tilt can be analyzed.

### **5.1 Parameters**

The model must fulfill some prerequisites to better fit the in-situ conditions. The near-surface movements need particular attention so that the spatial frame is narrowed under the free surface. Since the driving source of the deformations are the pumping activities and the media are poroelastic materials the sediments are regarded as fully saturated and unconsolidated sediments for the subsurface formations.

Some major interest is to clarify whether the effective forcing source comes from the central pit or is distributed over the well screens. Accordingly, a rather simple subsurface structure is modeled. Based on the poroelastic character, the hydraulic diffusivity of the subsoil is the dominating factor influencing the variation of the pore pressure gradient and ground deformation. This factor may result in greatly different behavior between diverse grain-sized materials. The local borehole information at shallow surface (Fig. 2.2) indicates the layering alternation between sand and clay possibly appears from 30 to 50 m deep, so a median number of 40 m is taken for the formation boundary, and a two-layered model is constructed.

Additionally, since the grain size of sand distribution varies from coarse to fine, medium sand is chosen to be the representative formation. The input parameters of both materials are selected from standard poroelastic samples (Fabian, 2004) and listed in table 5.1. Five parameters of shear modulus ( $\mu$ ), drained and undrained Poisson's ratios ( $\nu$  and  $\nu_u$ ), Skempton ratio (B), and diffusivity (D) are required. As the end points of the screen sections stretch 70 m away, the resolution frame of the model is set to 100 m for radial distance as well as for the vertical distance – both distances reaching far beyond the range of the screen sections. For the stress free surface, the rotationally symmetric variations of the hydraulic flows and the surficial movements disperse from the central pit to its radial distance and descending depths, extending to the infinity taken as the boundary conditions. Considering that the self loading and compaction effects of soils may increase with increasing depth, a slightly higher value of 0.7 GPa is adopted for shear modulus ( $\mu$ ) for distances exceeding 80 m (Wang and Kämpel, 2003).

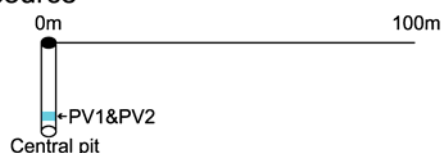
depth	formation	$\mu$ (GPa)	$\nu$	$\nu_u$	B	D (m <sup>2</sup> /s)
0-40	medium sand	0.2	0.15	0.4	0.85	18.2
40-80	clay	0.6	0.2	0.4	0.75	0.00042
80-100	clay	0.1	0.2	0.4	0.75	0.00042

Table 5.1 The formation parameters for modeling.

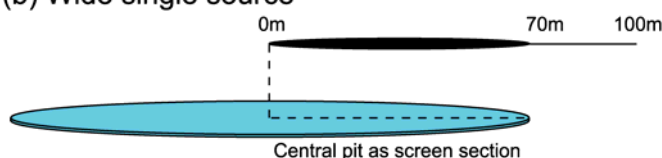
Four types of models with different forcing sources are constructed to differentiate the influences arising from either the central pit or the well screens. They are denoted as follows: (a) single point source, (b) wide single source, (c) disk-like source and (d) continuous points source. Models (a) and (b) assume the central pit as being the main forcing source, and are also called central source models. Models (c) and (d) emphasize more the impacts from the screen sections and can thus be considered as the peripheral source models. The concepts of different source types are illustrated in Fig. 5.1. The horizontal straight line symbolizes the radial distance (100 m) from the central pit, the round or elliptic black spots along the line are the surface-projected locations and forms of forcing sources and the blue areas indicate the real depths and distributions of the forcing sources.

In POEL, the source can be defined by its start depth, end depth, and the radius in the program. The difference between the two central source models, i.e. models (a) and (b) is the scale of the central pit. In (a), the single point source resembles to the case of a single well, which represents the central pit of this study. The start and end depths of the source are 18.5 m and 22 m, respectively, with depths of the two pump heads (PV1 and PV2) as references and the radius of the central pit being 2 m. In (b), a wide single source widens the radius of the central pit, extending it to the end of the screen section with a radial distance of 70 m. This assumes that an enormous central pit fully covers the area of the screen section and mimics the existence of a circular screen section at similar depth where it stretches out. For this purpose, the start and end depths of the source are set at 20.4 m and 20.6 m, respectively

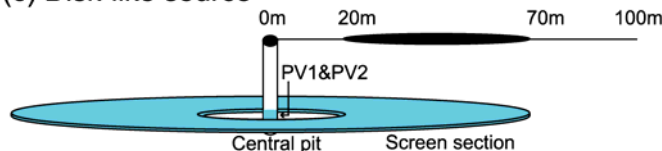
(a) Single point source



(b) Wide single source



(c) Disk-like source



(d) Continuous points source

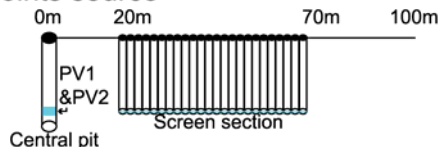


Fig. 5.1 Four types of pump source; the effective sources are shown by the round or elliptic spots. The central axis is at the central pit. Visualization of the results will be given to 100 m depth and 100 m radial distance.

Other parameters such as the duration and quantity of the pumping activity and the sampling spacing of data points are identical between the 2 models. To obtain a closer look over the length of each screen section, a denser mesh of sampling spacings is set between radial distance of 20 m and 70 m (2 m apart) while the mesh beyond this distance is set in steps of 10 m, giving a total of 31 steps. In addition, based on the criteria value of pump inducing signals, the source function is adjusted to  $100 \text{ m}^3$  per hour as the pump rate.

As to the peripheral source models, models (c) and (d) are distinct in terms of their source distribution style on

the screen sections. The concept of model (c) is similar to that of the wide single source but two enormous central pits are simultaneously considered, with radius of 20 m and 70 m, respectively. By subtracting the force distribution from these two pits, the area remaining appears to be a disk form with a hole in the center. To better mimic the in-situ scenario, a central pit is added into the model. The superposed result is denoted as disk-like source, i.e. model (c). The sampling spacing of data points and the duration and the source function follow the aforementioned conditions (i.e. 31 steps, 1 hour and  $100 \text{ m}^3/\text{h}$ ).

In contrast, the continuous points source model (d) partitions the length of the well screen into numerous points and imagines the points as several small wells continuously queued on the line. The start (20.4 m) and end depths (20.6 m) of the source are identical as in model (c), but the radii of these continuous small wells are reduced to 1 m. This model considers the impacts from one screen section separately, so that the quantity of the pumping activity along this well screen has to be divided first by 8, i.e.  $12.5 \text{ m}^3/\text{h}$ . A central pit is also included in this model to better represent the actual scenario. Besides, each point within the screen sections also acts an incoming source to certain fixed location or profile, the distance between them is individually calculated and varies from 0 to 170 m. To reduce the computing time, the distances are rounded upwards (e.g. 1 m is rounded up to 2 m, 3 m to 4 m, etc) so that the spacing is set to every 2 m instead of 1 m, giving a total of 86 steps. The general settings for the different source types are summarized in Table 5.2.

Source type	Spacing distance (m)	Central pit		Screen section		Pump	
		d (m)	r (m)	d (m)	r (m)	t (h)	q ( $\text{m}^3/\text{h}$ )
(a) single point	0, 10, 20, 22, 24.....66, 68, 70, 80, 90, 100 (31 steps)	18.5-22	2			1	100
(b) wide single		20.4-20.6	70				
(c) disk-like		18.5-22	2	20.4-20.6	20/70		
(d) continuous points		0, 2, 4...166, 168, 170 (86 steps)	18.5-22	2	20.4-20.6		1

Table 5.2 The settings for 4 types of forcing source, where depth is denoted as d, r is radius, t is duration and q is change in pump rate.

According to the spacing distance, the amplitude of tilt and pore pressure changes occurring at a fixed location, e.g. 10 m or 20 m away from the central pit can be estimated. Using a series of results of different locations (0, 10, 20-70, 80, 90, 100 m) along one profile, the induced variations from the central pit to its farthest radial distance of 100 m (in this study) can be illustrated. This is valid for the isotropic distribution with a spatial frame except for model (d).

Because the variation along the screen section might differ from its surrounding areas, a consistency check is performed. Accordingly, the simulated results of model (d) have to be calculated in 2 ways (Fig. 5.2): one is along the screen section and the other along the boundary area which has identical distance to its neighborhood screen sections. In Fig. 5.2a, the 8 horizontal wells, starting from the E flank, are denoted anticlockwise as R1 to R8. The number in subscript, i.e.  $R1_{10}$ , denotes the location 10 m away from the central pit on the E flank. Thus,  $Rn_{20}$ - $Rn_{70}$  (where  $n = 1$  to 8) is used to indicate locations of the partitioned points of screen sections. For example, if the impacts on point  $R1_{10}$  are considered, because  $Rn_{20}$  to  $Rn_{70}$  are regarded as 26 small wells, multiplying by 8 due to different directions, the superposed result from 208 individual forcing sources represents the result for location  $R1_{10}$ .

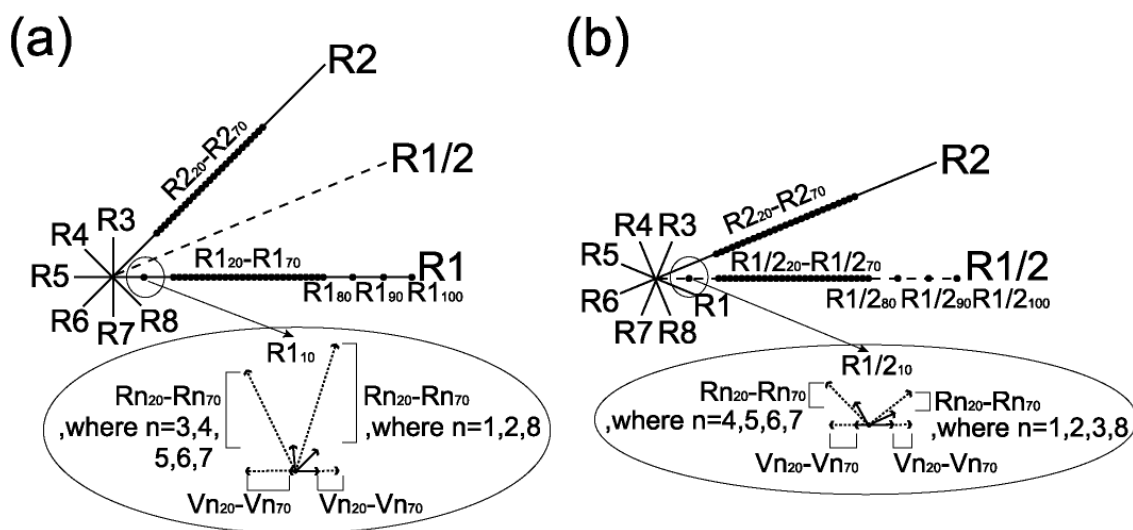


Fig. 5.2 (a) The analyzed vectors along one screen section (R1); (b) The analyzed vectors along one boundary area (R1/2).

As the influencing sources are placed in 8 directions, these 208 components may

be expressed by vectors. Because the 8 directions of arms are symmetric the vertical vectors are counteracted, and only the horizontal vectors are considered, e.g.  $V_{2_{20}} = R_{2_{20}} \cos \theta_{2-20}$ , (where  $\theta$  is the angle between  $R_{2_{20}}$  and  $R_{1_{10}}$ , and when  $\theta > 90^\circ$ , i.e.  $n = 3$  to  $7$ , the length of the vector becomes a negative number), thus the tilting quantity on a point can be estimated (eq. 5.1). Instead, if the pore pressure is reckoned, because the influence of hydraulic flow has to be superposed, an absolute value of  $\cos \theta$  is taken. Besides, the final amounts have to be divided by 26, showing that the modified pump rate along one flank still maintains  $12.5 \text{ m}^3/\text{h}$ , and by continuously calculating the effective vectors from 208 components to points ( $R_{1_0}$ ,  $R_{1_{20}}$ ,  $R_{1_{22}} \dots R_{1_{68}}$ ,  $R_{1_{70}}$ ,  $R_{1_{80}}$ ,  $R_{1_{90}}$ ,  $R_{1_{100}}$ ) along the E flank, the variations along this profile are seen. Moreover, due to the symmetry, the lengths of the vectors summed from R2 and R8; R3 and R7; R4 and R6 are respectively equaled ( $R_2 = R_8$ ;  $R_3 = R_7$ ;  $R_4 = R_6$ ).

$$\begin{aligned}
 R_{1_{10}} &= (V_{1_{20}} + V_{1_{22}} + \dots + V_{1_{68}} + V_{1_{70}}) / 26 \\
 &+ (V_{2_{20}} + V_{2_{22}} + \dots + V_{2_{68}} + V_{2_{70}}) / 26 \\
 &+ (V_{3_{20}} + V_{3_{22}} + \dots + V_{3_{68}} + V_{3_{70}}) / 26 \\
 &+ (V_{4_{20}} + V_{4_{22}} + \dots + V_{4_{68}} + V_{4_{70}}) / 26 \\
 &+ (V_{5_{20}} + V_{5_{22}} + \dots + V_{5_{68}} + V_{5_{70}}) / 26 \\
 &+ (V_{6_{20}} + V_{6_{22}} + \dots + V_{6_{68}} + V_{6_{70}}) / 26 \\
 &+ (V_{7_{20}} + V_{7_{22}} + \dots + V_{7_{68}} + V_{7_{70}}) / 26 \\
 &+ (V_{8_{20}} + V_{8_{22}} + \dots + V_{8_{68}} + V_{8_{70}}) / 26 \\
 &= (R_{n_{20}} \cos \theta_{n-20} + R_{n_{22}} \cos \theta_{n-22} + \dots + R_{n_{68}} \cos \theta_{n-68} + R_{n_{70}} \cos \theta_{n-70}) / 26 \\
 \text{or} &= (R_{n_{20}} |\cos \theta_{n-20}| + R_{n_{22}} |\cos \theta_{n-22}| + \dots + R_{n_{68}} |\cos \theta_{n-68}| + R_{n_{70}} |\cos \theta_{n-70}|) / 26
 \end{aligned} \tag{eq. 5.1}$$

, where  $n = 1$  to  $8$ .

Generally, this result represents the variations along the screen sections. However, the result along boundary area ( $R_{1/2}$ ) may change, because the distances from  $R_{1/2}$  to each screen section of incoming sources are different. Figure 5.2b illustrates the analyzed vectors similar to Fig. 5.2a. If the induced amplitude on point  $R_{1/2_{10}}$  (where  $R_{1/2_{10}}$  is 10 m away from the central pit along the boundary area) is considered, the distances from each screen section of forcing sources ( $R_{n_{20}}-R_{n_{70}}$ ) to  $R_{1/2_{10}}$  have to be accounted for. The forces are similarly transformed to vectors ( $V_{n_{20}}-V_{n_{70}}$ ), which are superposed and divided by 26 to show the induced amplitude of tilt. But when  $n$  equals 4 to 7 that  $\theta$  is larger than  $90^\circ$  and negative vectors appear in this case.

The flow can also be expressed by eq. 5.1, and the  $|\cos\theta|$  values are used when the variations of pore pressure are considered. The effective vectors on the other 30 points (R1/2<sub>0</sub>, R1/2<sub>20</sub>-R1/2<sub>70</sub>, R1/2<sub>80</sub>, R1/2<sub>90</sub>, R1/2<sub>100</sub>) along the boundary area are successively solved according to the same superposition principle. But the symmetric condition of pairing distance in this case would be R1 equals R2; R3 equals R8; R4 equals R7 and R5 equals R6, which results in the same transformed vectors from any point along the boundary area to R1 and R2; R3 and R8; R4 and R7; R5 and R6.

For all types, the resolved spacing in depth is every 10 m, and since through the transform and superposition, the results in radial distances of model (d) are under the same spatial frame as the other types, the variations of the tilt and pore pressure for 4 types of forcing sources can be compared. The results are presented in following sections, grouped by central source and peripheral source models. All the diagrams show results within the X-Z plane for 100 m radial distance and 100 m depth.

## **5.2 Central source models**

The central source models include the single point source and the wide single source. The forcing source of both models is in the central pit only, but differs from its scale. The induced processes for each model are shown in Fig. 5.3 and Fig. 5.4. The diagrams on the left side (a) and right side (b) give the results of pore pressure and tilt in units kPa and  $\mu\text{rad}$ , respectively. The variations are illustrated in a chronological order after the initiation of pumping at the given time points: 3.6 s, 18 s, 36 s, 72 s (1.2 min), 108 s (1.8 min), 144 s (2.4 min), 180 s (3 min), 720 s (12 min), 1800 s (30 min), and 3600 s (1 h). The line with zero amplitude called zero-line in the subsequent; is enhanced in all diagrams.

### **5.2.1 Single point source**

For model (a), the increment of each contour line in Fig. 5.3a is 4 kPa, while in Fig. 5.3b it is 0.4  $\mu\text{rad}$ . Fig. 5.3a shows an obvious concentration of pore pressure near the location of the central pit, i.e. the source in this model. The maximum gradient of pore pressure appears at this point and decreases outwards along its radial distance. The influencing range of the source with pore pressure distortion exceeding -1 kPa



extends to 45 m deep, and expands from 20 m to 30 m radially. It leads to the development of a zero-line changing from the outer circle of the source to a gradually flattening line, existing near the upper surface at 2 m depth and at the boundary of the 2 formations i.e. at 50 m depth. The variations in the sand formation evolve quickly. The results approach to a relatively steady status in 1 hour. Except for some variation of zero-line changing contours are rarely seen in the clay formations due to the great difference in diffusivity which require much longer time to reach steady state.

Similarly, in Fig. 5.3b, the variations in tilt movements are clearly observed in the subsurface above 50 m depth. However, since our major concern is related to the near-surface movements, the one-hour interval resolution of the models is sufficient. Under homogeneous half-space condition, the maximum tilt normally appears to be at  $1/\sqrt{2}$  portion of the source depth in radial distance, i.e. at 14 m depth here. But in this two-layered model, the maximum tilt occurs from 10 m to 20 m radial distance eventually reaching steady state.

The zero-line appears to be near the source and be an enveloping circle from 10 m to 20 m in depth with reducing width from 25 m to 20 m in radial distance. It is close to the axis (0 m) beyond 50 m depth. The gradients of tilt develop from the enveloping circle upwards to the surface and downwards to the formation boundary in a slightly symmetric mirror image. Additionally, the upward variations to the surface are greater than the downward variations due to a stress free plane at the surface. Induced tilt movements of large amplitude concentrate within 60 m in radial distance, but the influenced range extends up to a radius of around 100 m.

Normally if the increment of the maximum value reaches 1/3 of the final status, the time frame of this situation is assumed to be approaching the steady state. However, this is hard to distinguish in the figure due to the scale used for the contours in the diagrams. But from the gradients of variations can be see that the time interval between 108 s and 144 s could represent this approaching phase. The maximum pore pressure and tilt reach about -29 kPa and -3  $\mu$ rad, respectively.



### 5.2.2 Wide single source

The identical layout of time series and variations in pore pressure and tilt movement of model (b) are seen in Fig. 5.4. But the amounts of distortions are greatly different since the increment of contours is reduced a hundred-fold to 0.05 kPa for pore pressure (Fig. 5.4a) and 0.04  $\mu\text{rad}$  for tilt (Fig. 5.4b). An even smaller increment of 0.01  $\mu\text{rad}$  is taken at time 3.6 s. The maximum pore pressure and tilt also decreases to -0.65 kPa and -0.5  $\mu\text{rad}$ , respectively.

Compared with model (a), the source of model (b) is slightly shorter in depth but much wider in radial distance. Accordingly a thinner and wider pore pressure concentration zone (like the shape of a tongue) in the sand formation is seen in Fig. 5.4a. The maximum value in the zone occurs at the location of the source. The strongly influenced range of the source extends from 10 to 30 m depth and is 70 m wide after a few seconds. With increasing time, the range expands downwards to 50 m and to more than 100 m in radial distance.

The zone of greater pore pressure value appears to be thicker than model (a) but narrows down 0 m radial distance gradually. The zero-line evolves from 40 m to 50 m depth and also becomes more flat eventually. Below the formation boundary i.e. from 50 m to 80m depth, the value of the pore pressure change turns to be weak and positive; here the variations form in the shape of a triangle whereas the values increase inwards. The maximum value is close to the formation boundary.

As for the results of induced tilt in Fig. 5.4b, symmetric variations evolve from the source location upwards and downwards. The strongest variations appear to be associated with the end point of the source that near the radial distance of 70 m. The maximum tilt appears at the same distance but along the stress free plane at zero depth. The amplitude decreases towards the center and downwards to the 100 m depth boundary as a quarter-arc envelop.

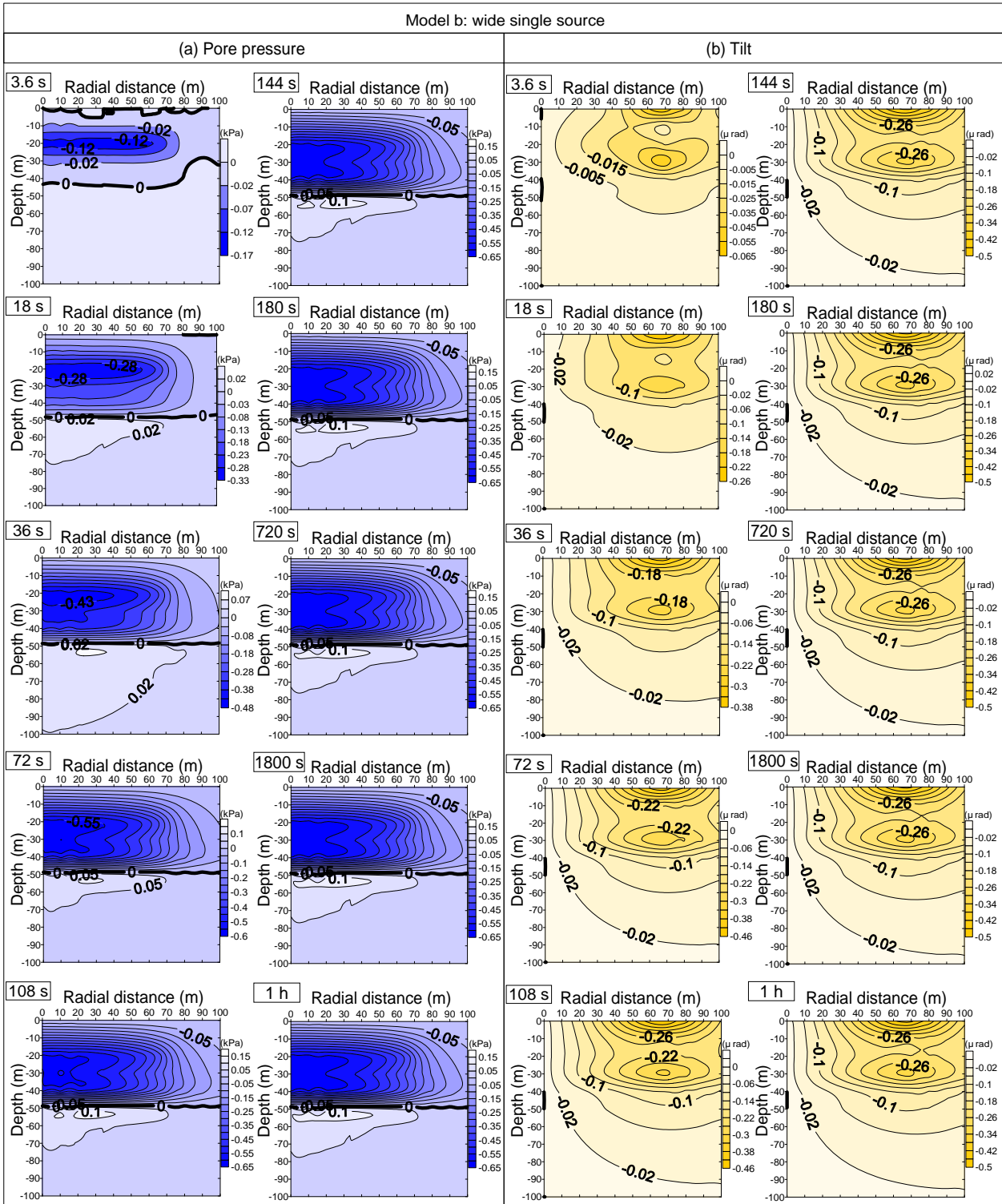


Fig. 5.4 Simulated results of pump induced changes on X-Z profile for wide single source (type b). (a) The variations of pore pressure, and (b) tilt through times after onset of pumping: 3.6 s, 18 s, 36 s, 72 s (1.2 min), 108 s (1.8 min), 144 s (2.4 min), 180 s (3 min), 720 s (12 min), 1800 s (30 min), and 3600 s (1 h).

The zero-line is confined to near zero radial distance at shallow depth of 5 m and from 40 to 50 m. The strongly influenced range of tilt movements extends to 80 m radius at the beginning and develops to more than 100 m in the quasi-steady status. As the gradient patterns do hardly change from time 108 s to 144 s, the system is assumed to be approaching the quasi-steady state.

A comparison is made for the location of the maximum values of tilt movements for both models in Table 5.3. Regardless of model (a) or (b), the value in the sand formation is 3 to 5 times larger than in clay.

	formations	location (r, z)	max. tilt ( $\mu\text{rad}$ )
Model (a)	Sand (0-40m)	(20, 0)	-3
	Clay (40-100m)	(16, -40.5)	-0.6
Model (b)	Sand (0-40m)	(67, 0)	-0.5
	Clay (40-100m)	(70, -40.5)	-0.14

Table 5.3 Comparison of maximum tilt between the two formations of models (a) and (b).

### 5.2.3 Depth-radial distance comparison

Figure 5.5 shows analyses of sections from the 2 models for several selected depths. The variations of the pore pressure and tilt movement are given with “close-up” images. The total duration of the time frame is set to 0.5 hour only to see the difference before and after the pump starts (at 1 h). Each plotted line in the diagrams represents the number of the radial distance from center (0 m), i.e. r10 is 10 m in radial distance. Stronger changes occur in the sand formation and at locations relatively near to the surface. The depths sampled between ground surface (0 m) and well screen (20 m) is 10 meter, and an additional depth of 50 m for the boundary of the clay formation is chosen.

When  $z = 0$  m, the pore pressure of both models is 0 kPa, because the energy dissipates along this stress-free plane. Besides it can also cause greater ground movements than at other planes (depths), so that the induced amplitudes of tilt at this plane are the largest (-3  $\mu\text{rad}$  and -0.5  $\mu\text{rad}$  in models (a) and (b), respectively). No tilt is induced at  $r = 0$  m, but with the increment of radial distances, the variations of amplitudes are different between two models. For model (a), the amplitude of tilt

keeps increasing up to  $r = 20$  m, being the location of the maximum tilt, and the amplitude of tilt decreases from  $r_{30}$  to  $r_{100}$ . Instead, the turning point of maximum tilt in model (b) is at location  $r = 70$  m, and the amplitude of  $r = 80$  m is similar to the range of  $r = 50$  m;  $r_{90}$  is similar to  $r_{40}$ ; and  $r_{100}$  is similar to  $r_{30}$ .

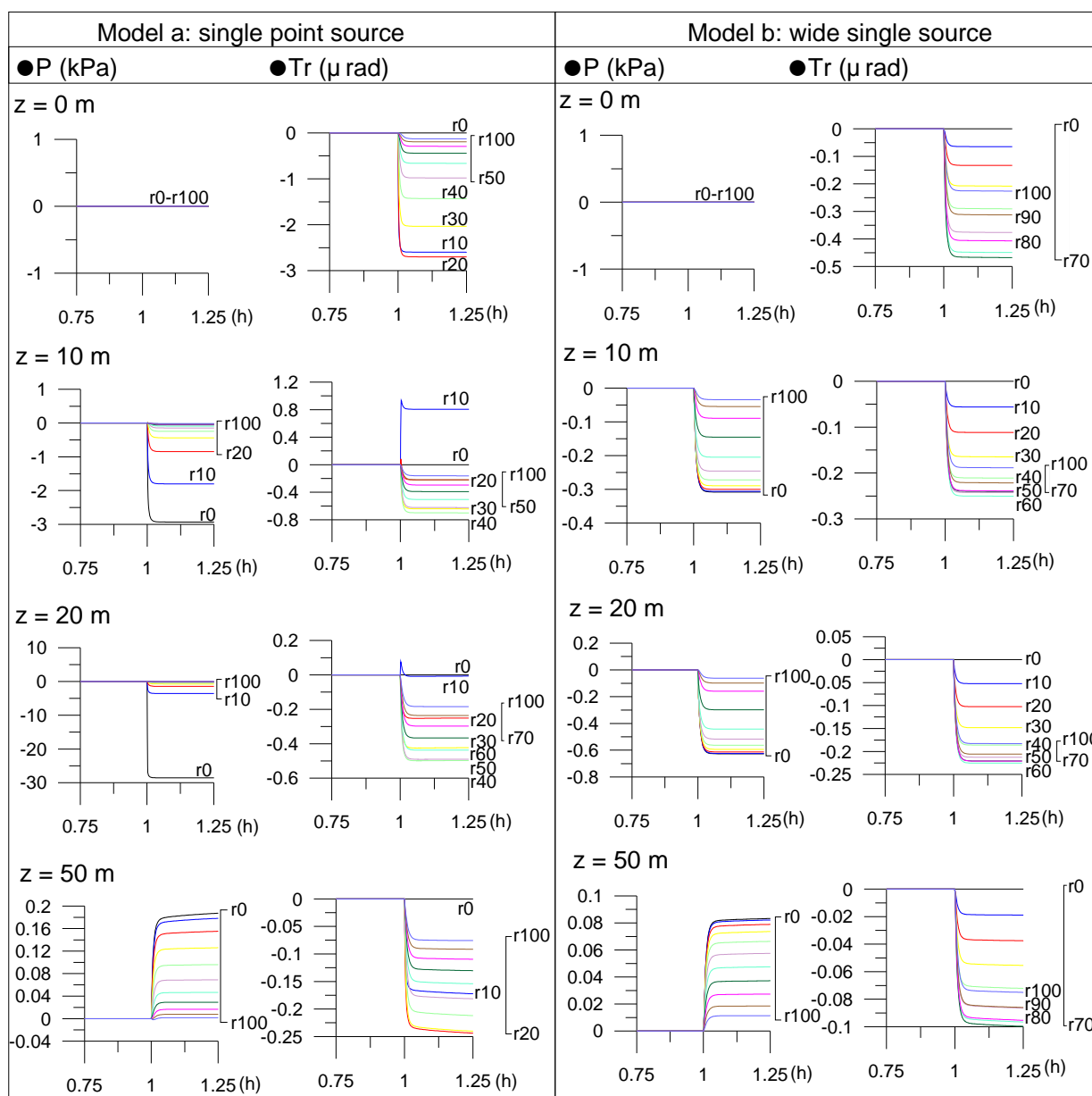


Fig. 5.5 Analyses of pore pressure (P) and radial tilt variations (Tr) for models (a) and (b) at 4 selected depths. The notation  $r$  is for radial distance and  $z$  is depth.

At a depth of 10 m, the variations of pore pressure at different radial distance distribute similarly. When the location is closer to  $r = 0$  m, the magnitude of pore

pressure is greater; when closer to  $r = 100$  m, the magnitude is smaller. But because the source of model (a) is much smaller than model (b), when  $r$  is larger than 50 m, the magnitude of pore pressure declines to 0 kPa.

For tilt variations, normally when pumping occurs, a subsidence response in ground deformation is expected, which causes a tilt with increasing amplitude. However, a reverse tilt signal at first few seconds, so called Noordbergum effect (Verruijt, 1969; Maruyama, 1994; Kim, 1997) is seen at  $r = 10$  m and 20 m in model (a), showing a good example for the coupling of pore pressure and ground deformation. For the other locations, the amplitude of tilt increases to  $r = 40$  m, and decreases to  $r = 100$  m where it is the minimum. The result of  $r_{50}$  decreases similarly to  $r_{30}$  and  $r_{90}$  to  $r_{20}$ . No Noordbergum effect is observed in model (b), the amplitude of tilt increases to a maximum value at  $r = 60$  m, and decreases to  $r = 100$  m. The amplitude of  $r = 70$  m and 80 m is about in the range of  $r = 50$  m;  $r_{90}$  is  $r_{40}$ ; and  $r_{100}$  has a value between  $r_{30}$  and  $r_{40}$ .

The variations of pore pressure and tilt movement at depth 20 m have similar distributions as at 10 m depth. But the magnitudes of pore pressures are much larger, probably the largest among all depths. It indicates the depth where the forcing source is located, which can be seen more clearly in model (a). The result at  $r = 0$  m is about 6 times larger than at other radial distance, showing it is close to the center of the source, and the magnitude decreases with increasing radial distance ( $r_{10}$ - $r_{100}$ ). However, while this source extends to 70 m with a smaller magnitude in model (b), the difference between the center of the source ( $r_0$ - $r_{70}$ ) and the influenced area ( $r_{80}$ - $r_{100}$ ) is not obvious. Only a relatively large difference occurs around  $r = 70$  m, but the magnitude keeps decreasing from  $r_0$  to  $r_{100}$ .

At  $z = 20$  m, the Noordbergum effect can only be seen at  $r = 10$  m in model (a). Thus, the existence of this effect is reflected well in the development of the zero-line in Fig. 5.3b. When the radial distance ( $r$ ) and depth ( $z$ ) of a chosen point is located in the area where the zero-line evolves, the reverse sign of tilt is appearing. This is verified with the development of the zero-line in Fig. 5.4b which is on the edge of  $r_0$ , so that none of these effects appear in Fig. 5.5 of model (b). The maximum tilt is at  $r = 40$  m, and minimum at  $r = 100$  m in model (a) as at  $z = 20$  m, but a similarity of

amplitude changes exists between: r50, r40; r60, r30; and r90, r20. For model (b), the maximum tilt is still at  $r = 60$  m, and the similarity of amplitudes is between: r70, r80, r60; r90, r50; and r100, r 40.

As for  $z = 50$  m, weak positive values of the pore pressure are seen in both models (a) and (b). This may be caused by the much smaller diffusivity of clay which traps the pore pressure, confines it in this formation and appears to be an opposing force to pumping. This probably indicates the presence of the Noordbergum effect. The amplitude of pore pressure reduces with increasing radial distance; the maximum is at r0 and the minimum is at r100 in both models. The tilt variation is related to the location of the source which has a maximum value at r20 and minimum at r100 in model (a) while the amplitude increases to r70 and decreases to r100 in model (b). The amplitude similarity in model (a) is between r10 to r50; and in model (b) at depth of 20 m between: r80, r60; r90, r50; and r100, r 40.

In general, with increasing depth, the difference between models (a) and (b) becomes smaller. That is, the pore pressure in model (a) is about 10 times higher and tilt is 3 times higher than in model (b) at  $z = 10$ ; but the ratios reduce to 2 times and 2.5 times, respectively, at  $z = 50$ . An exception with pore pressure occurs at  $z = 20$ . Due to the large difference in the source itself, the difference in the ratio of pore pressure is about 37.5-fold. Amplitude differences will be compared more in the next section.

### **5.3 Peripheral source models**

The disk-like source (model c) and the continuous points source (model d) consider not only the central pit, but also the screen section as the forcing source, so that the results are the superimposed outcomes from both effects. Figures 5.6 to 5.8 illustrate the developing processes for model (c), model (d) along the screen section and for model (d) on the boundary area, respectively.

The layouts of the three figures are identical: the changes in pore pressure in unit of kPa are on the left (part a) while the tilts in  $\mu\text{rad}$  are on the right (part b). As before, the diagrams are chronologically ordered: 3.6 s, 18 s, 36 s, 72 s (1.2 min), 108 s (1.8 min), 144 s (2.4 min), 180 s (3 min), 720 s (12 min), 1800 s (30 min), and 3600 s (1 h).



The timing starts with the activation of the pump.

### 5.3.1 Disk-like source

Model (c) is considered first. In Fig. 5.6a, contour lines increase by 4 kPa and in Fig. 5.6b by 0.2  $\mu$ rad. Additional extrapolation is applied for drawing the zero-line. The distribution of contours in Fig. 5.6a is similar to that in Fig. 5.3a, the central pit has strongest influence on pore pressure. However, another smaller influenced zone, namely along the screen section, can also be seen. Due to the dual effects of 2 forcing sources, the strongly influenced range near the central pit reduces to a 10 m wide zone but still occurs at a depth between 10 m and 30 m. At 3.6 s, an enclosed envelope develops near the screen section from radial distance of 20 m extending to 100 m and within 40 m depth and probably marks the Noordbergum effect.

With increment of time, the influencing source of the central pit enlarges to cover a radial distance of 100 m while the effect of the source of the screen section migrates towards opposite direction to 0 m. The influenced zones from the 2 sources eventually join, except for a small spot located at a depth and radial distance of 20 m. The zero-lines also change from 2 envelopes to 2 flat lines near the ground surface and the formation boundary. However, the source point of the central pit still has the maximum value of pore pressure because the forcing here is much larger than at the source of the screen section.

The variations of tilt in Fig. 5.6b are based on a similar principle of sources with joining influence. The larger amplitudes of tilt mostly occur at the location near the central pit, especially along the ground surface. Slightly symmetric variations of tilt develop upwards and downwards from the depth of 20 m with increasing amplitudes. Because of the double source effect, the sources may be considered as 2 opposing forces for the locations within intermediate radial distances. With propagation of the forces, the tilt variations and induced subsidence become partially “neutralized”. So when time evolves, the tilt movements induced by the screen sections join and form some wavy distributions of contours.

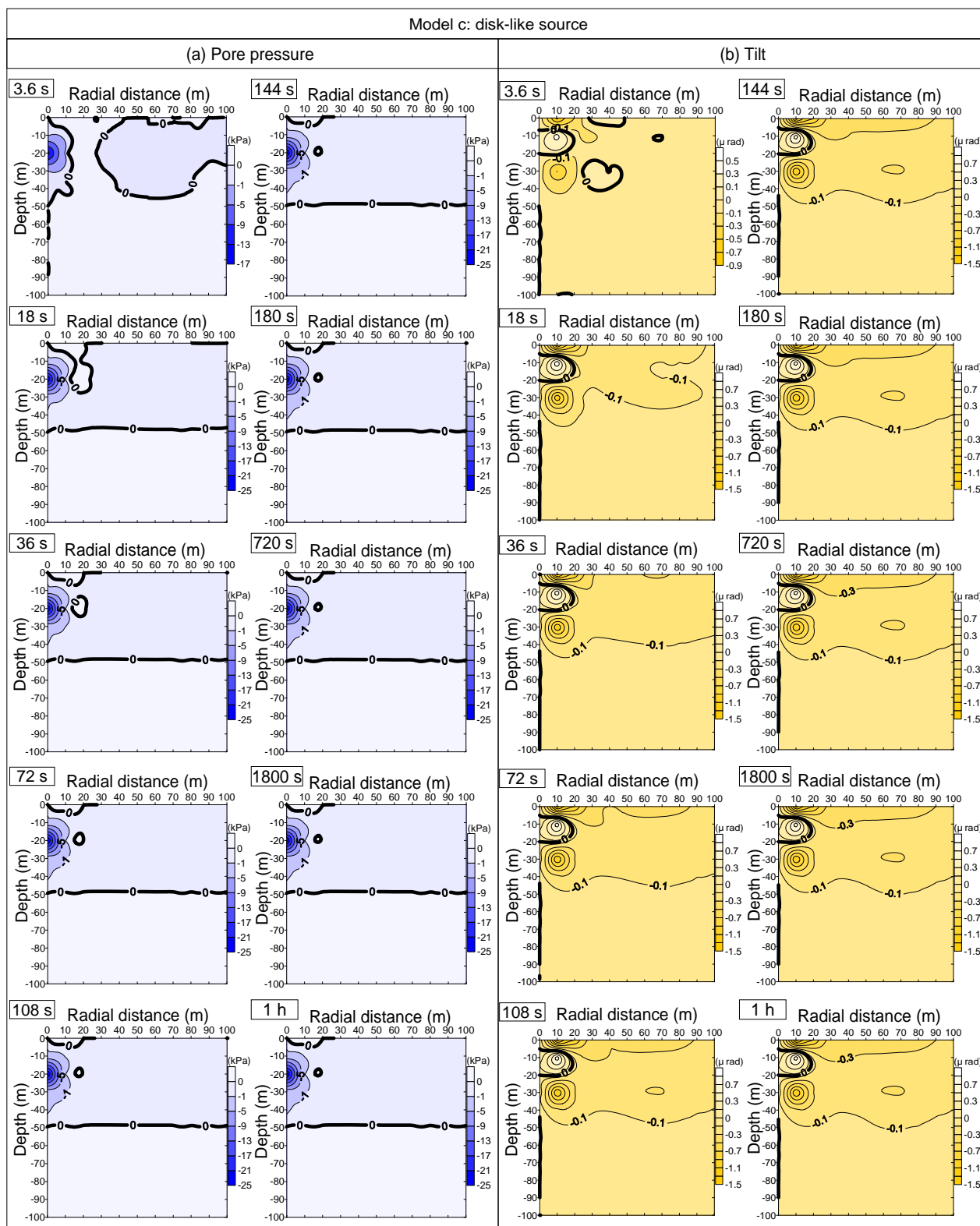


Fig. 5.6 Simulated results of pump induced changes on X-Z profile for disk-like source (type c). (a) The variations of pore pressure, and (b) tilt through times after onset of pumping: 3.6 s, 18 s, 36 s, 72 s (1.2 min), 108 s (1.8 min), 144 s (2.4 min), 180 s (3 min), 720 s (12 min), 1800 s (30 min), and 3600 s (1 h).

Although the order of the tilt amplitude is relatively small (compared to the one induced by the central pit), the subsidence existing from 20 m to 70 m in radial distance shows that the concentrating forces partly come from the screen section.

The zero-line appears to contour 3 zones and 2 edges at the beginning. One zone occurs near the source of the central pit at depth of 10 to 20 m extending to 20 m width. The other two are located at similar radial distance from 30 m to 50 m but with different depths (10 m deep and from 30 m to 40 m, respectively) and edges (from 30 m to 40 m and from 50 m to 90 m, respectively). The zone near the central pit remains even though the two zones at the locations between the 2 sources vanish with increasing time. This reflects the sources joining as well.

The maximum tilt occurs at radial distance of 10 m, and the amplitude decreases radially outwards from this point. A wider influencing range extending more than 100 m has contributions from both sources. The variations beyond 50 m in the clay formation still have nearly the same distributions, pointing out that more time is needed before a deformation is observed. The variations in the sand formation are considered to be in quasi-steady status with no major gradient changes after 144 s. In general, the order of the range of this model is similar to model (a); the maximum pore pressure and tilt are -25 kPa and -1.5  $\mu\text{rad}$ , respectively.

### 5.3.2 Continuous points source

As for model (d), the pore pressure and tilt variations are presented in chronological order as aforementioned. Although this model separately considers the situation for the screen section and the boundary area, the analytic results (by screen section and boundary area) fall in the same order. The increments of contours are identical: for pore pressure 4 kPa and for tilt 0.04  $\mu\text{rad}$  (Figs. 5.7, 5.8). The maximum pore pressure and tilt of both scenes are -29 kPa and -2.9  $\mu\text{rad}$ , and similar to the results of model (a).

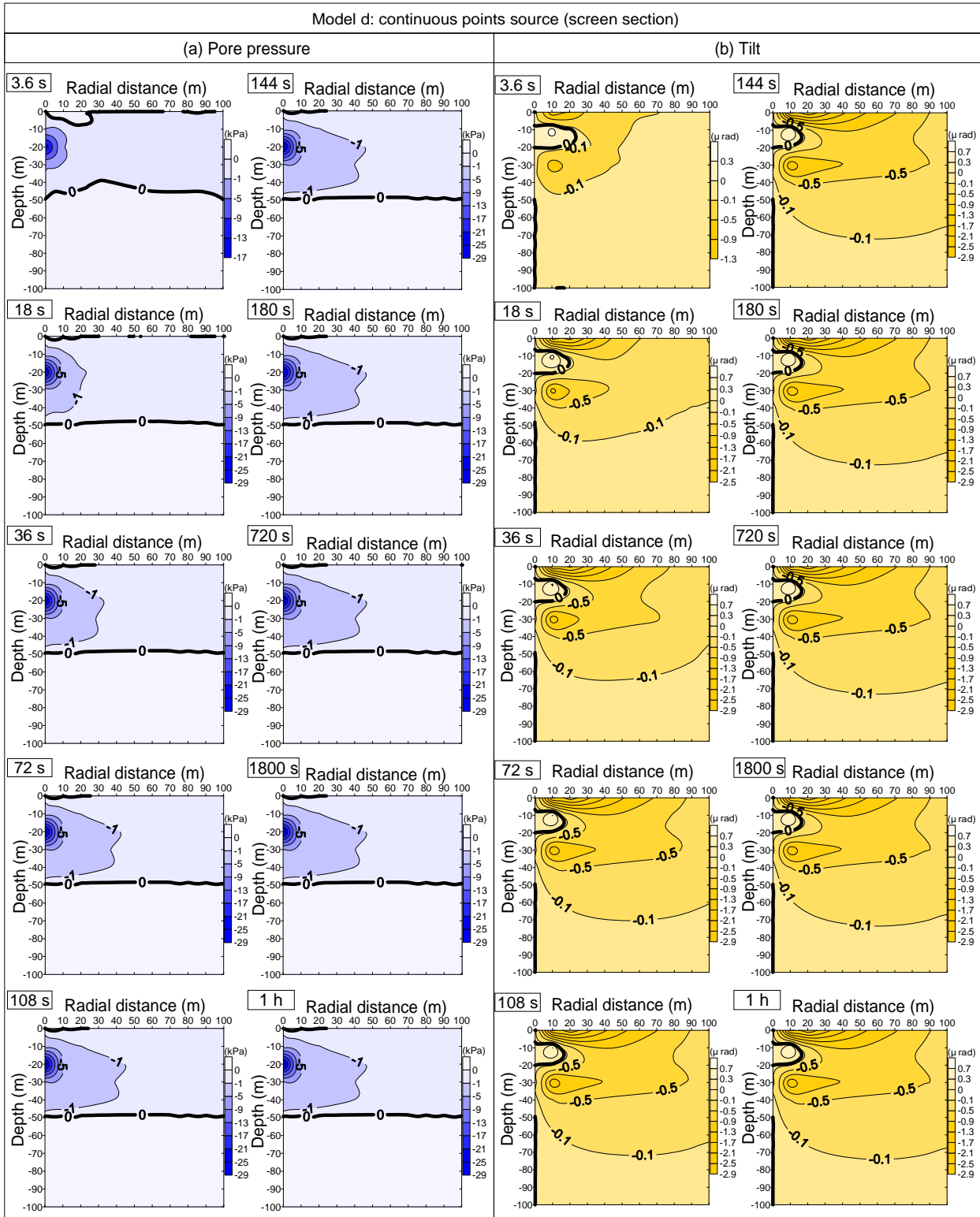


Fig. 5.7 Simulated results of pump induced changes on X-Z profile for continuous points source (type d) on the screen section. (a) The variations of pore pressure, and (b) tilt through times after onset of pumping: 3.6 s, 18 s, 36 s, 72 s (1.2 min), 108 s (1.8 min), 144 s (2.4 min), 180 s (3 min), 720 s (12 min), 1800 s (30 min), and 3600 s (1 h).

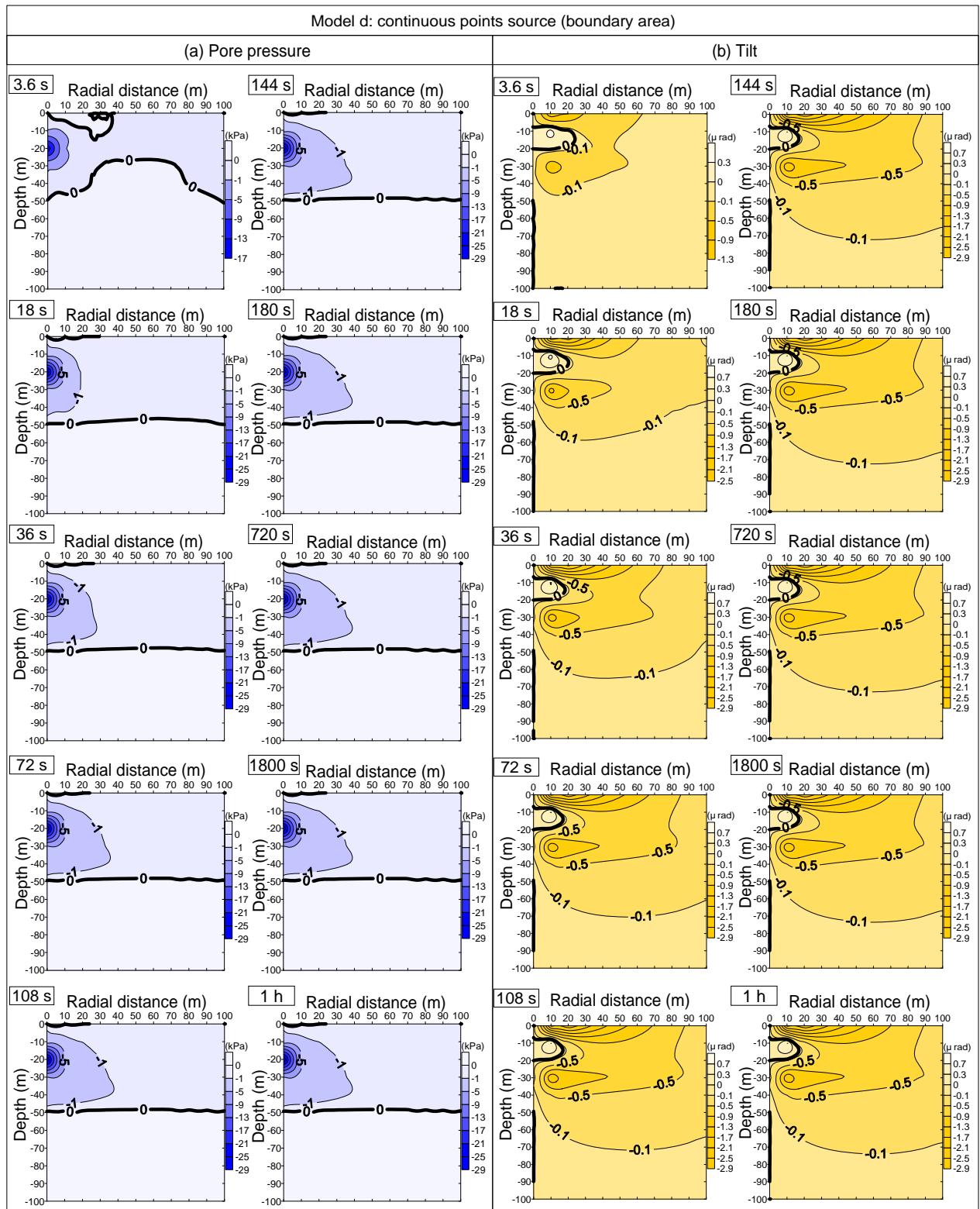


Fig. 5.8 Simulated results of pump induced changes on X-Z profile for continuous points source (type d) on the boundary area. (a) The variations of pore pressure, and (b) tilt through times after onset of pumping: 3.6 s, 18 s, 36 s, 72 s (1.2 min), 108 s (1.8 min), 144 s (2.4 min), 180 s (3 min), 720 s (12 min), 1800 s (30 min), and 3600 s (1 h).

However, some differences still exist between models (a) and (d), because the influence of the screen section is additionally considered in model (d), similarly to model (c). As the source of the screen section in model (c) is subtracted from two hypothetical large wells, a gap exists that is not compensated by the source of central pit. Unlike in model (c), the source of the screen section in model (d) is supposed to be continuous, with a compensating force from the central pit. The combined process of 2 sources appears at beginning in Fig. 5.7a and Fig. 5.8a.

The zone with higher pore pressure still lies near the central pit from depth of 10 m to 20 m and extends 10 m wide. The maximum value occurs at the source, where the influenced range reaches the screen section area at 20 m radial distance, the gradients plot slightly different. At radial distance of 40 m, the contour in Fig. 5.7a appears to be a “rotated M” while a “rotated V” is even in Fig. 5.8a. Two peaks of the “rotated M” occur at depths of 20 m and 40 m, showing that the influence of the screen section and the formation intersection may cause the increase in magnitude. The peak of the “rotated V” occurs around 40 m depth at the formation boundary.

The difference between the screen section results and the boundary area results can also be distinguished by the development of the zero-line at the beginning phase. Because no screen section is located in the boundary, the influenced range in Fig. 5.8a is smaller than in Fig. 5.7a, so initially the zero-line appears to be more curved. With increasing time, the zero-line distributions of both similarly evolve and become two flat lines: one near the ground surface extending about 25 m wide, and another beyond the formation boundary at depth of 50 m.

The similar evolving progress of 2 influencing sources can also be seen in the tilt results of Fig. 5.7b and Fig. 5.8b. The amplitude increases symmetrically from the source of the central pit upwards and downwards. Closer to the screen section, the distribution of the contours seems to be “stretched” to the radial direction. The influencing range is wider and the amplitude at the same location is larger than in model (a).

The zone of larger amplitudes between the depth of 10 m and the stress free plane (0 m) expands radially from 20 m to 70 m, the location of maximum tilt changes from 10 m to 20 m in radial distance. Another, smaller large amplitude zone exists

above the formation boundary (from depth of 30 m to 40 m), expanding radially from 10 m to 30 m and showing a more obvious stretching effect from both sources. The zero-line develops near the source of the central pit from 10 m to 20 m depth, extends to radial distance of 20 m, and also appears along the axis from 25 m to 30 m and from 50 m to 90 m depth.

The contours between Fig. 5.7b and Fig. 5.8b are slightly different in that the 2 concentration zones are wider and flatter in 5.8b. Because these two zones develop above and below the location of the screen section, and since the boundary area has no screen section, the direct influence from the screen section is eliminated. The increasing gradient from the source location is further up and down in this case. Due to the same effect, the valley-like contour at depth 20 m, from radial distance of 80 m to 90 m shows a smoother curve in Fig. 5.8b. In general the quasi-steady status is achieved around 144 s.

### 5.3.3 Comparison of screen section and boundary area

To distinguish the differences between the induced signals on the screen section and the boundary area, Fig. 5.9 integrates the results from both components and illustrates them as 2-D and 3-D images. The results of the screen section (Fig. 5.7) represent the flanks in the orientation of E, NE, N, NW, W, SW, and S, and the one of the boundary area (Fig. 5.8) is for of ENE, NNE, NNW, WNW, WSW, SSW, and SSE. The variations in pore pressure and tilt are shown for selected depths and time frames, the spatial frame of the diagram is 200 m × 200 m.

Because most variations appear at shallow depth and also at the depths of the central pit and the screen section, section analyses for depths of 10 m and 20 m are committed. Also, an additional section for the clay layer at 50 m depth is selected. The evolving progress and differences from the dynamic to the steady states can be understood by choosing 3.6 s and 3600 s as short and long time influences. To better show the contrast in pore pressure magnitude and tilt amplitude, the scales for all diagrams have not been adjusted to the same dimension. The increments of contours for each are listed in Table 5.4. Zero-lines are extrapolated as well.

At a depth of 10 m, the influencing range caused by the screen section or the

boundary area can be easily distinguished in the 3-D diagrams. For pore pressure, the light blue area with the larger magnitude represents the 8 screen sections while the dark blue zones mark the boundary area. When approaching the steady state, larger amplitudes appear in the center while the mostly influenced range is about 20 m wide. It shows that the influence from the central pit becomes dominant instead of that of the screen section at this phase, so that the difference between the screen section and the boundary area diminishes greatly. The distinct distribution of the screen sections fades away.

This can be also seen from the contour distributions in the 2-D diagram. The pattern of the pore pressure looks like a shining sun at beginning, each beam of sunlight indicates the boundary area that is not in the influenced range of the screen section. It turns to be flower like with eight petals, where a petal tip is for a screen section. The hydraulic flow distributes more equally in the whole space, but the amplitude difference between the screen section and the boundary area becomes much less. The influence decreases radially outwards from the central pit and also from the screen section to the boundary area.

Instead, the tilt results at beginning appear to be flower like already, but the petal tip indicates the boundary area. Because initially, the influence of the screen section is stronger than in the final state, the tilt movements are rather “neutralized” at locations close to the screen section. On the boundary area, the screen section influence is reduced by increasing distance; the remaining influence comes mostly from the central pit and has a larger effect than the screen section.

By reaching the steady state, the role of the screen section is concealed by the central pit with much stronger source. The difference between the screen section and the boundary area largely vanishes. Only a small indication exists at radial distance of 30 m (a flower like pattern) that the screen section still has a slightly larger influence at this distance. The gradient pattern evolves to an octagon at 50 m that has its angle points at the locations of screen sections; the amplitudes at the locations of the screen sections and boundary areas are similar. Gradients in large radial distance become merely concentric circles. The tilt amplitude decreases with increasing radial distance and with increasing distance from the screen section because the role of the central pit



is the most important.

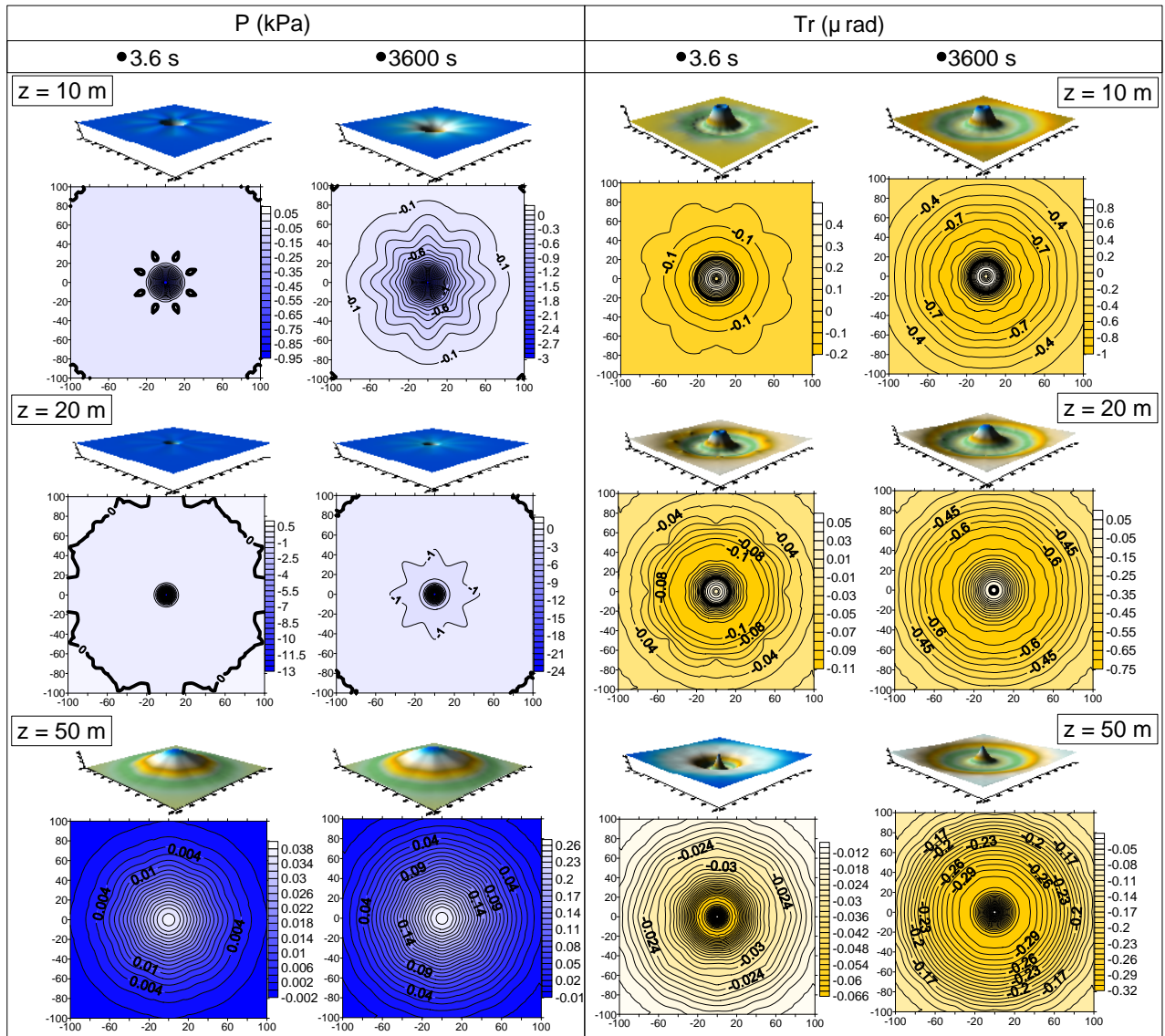


Fig. 5.9 Integrated results from the screen section and the boundary area in 2-D and 3-D illustration. Specific times (3.6 s, 3600 s) and depths (10 m, 20 m, 50 m) are selected for the variations of pore pressure and tilt.

Time \ Depth	P (kPa)		Tr (μrad)	
	3.6 s	3600 s	3.6 s	3600 s
z = 10 m	0.5	0.1	0.5	0.1
z = 20 m	0.5	1	0.01	0.5
z = 50 m	0.002	0.01	0.002	0.01

Table 5.4 The increments of contours for all times and depths in Fig. 5.9.

A similar evolution is seen at depth of 20 m, but because this is the depth of the central pit source, the amplitude difference has enlarged. All patterns are alike to the results at  $z = 10$  m, but the scale is apparently smaller. In pore pressure, the beam of sunshine disappears, the petals of flower shrink; in tilt, more octagons distribute from radial distance of 50 m to 60 m at initial phase, and only concentric circles are left at the steady state. In the 3-D image, the pore pressure distribution of the screen sections becomes vaguer, and the tilt differences at the petal regions turn to be rounder. All this indicates the strong dominance from the central pit.

At depth of 50 m, due to the confined environment, the value of the pore pressure becomes positive in the center, the amplitude still decreases with increasing radial distance. This is also valid with the tilt movements. Due to the depth, the influence from the screen section reduces further, only the patterns of concentric circles can be seen both in pore pressure or tilt.

In general, if a similar section analysis of depth-radial distance such as Fig. 5.5 is taken for models (c) and (d), the results of pore pressure and tilt distributions would be more like the results of model (a). The aforementioned results from Fig. 5.7 and Fig. 5.8 illustrate excellent examples of this possibility. The Noordbergum effect could be observed at similar depths and radial distances while the development of the zero-line is alike.

The maximum tilts and the locations where they occur for the two formations of both models are noted in Table 5.5. The values in the sand formation are about 5 times larger than in the clay for both models, and the locations of maximum tilts differ. It implies that the source of the screen section in model (c) has a stronger influence on the central pit than in model (d) and that the amplitude is much reduced compared with model (a). A more detailed discussion about the validation of the 4 models will be given in the next chapter.

	formations	location (r, z)	Max. tilt ( $\mu$ rad)
Model (c)	Sand (0-40 m)	(10, 0)	-1.4
	Clay (40-100 m)	(14, -40.5)	-0.3
Model (d)	Sand (0-40 m)	(20, 0)	-2.8
	Clay (40-100 m)	(16, -40.5)	-0.6

Table 5.5 Maximum tilt values in two formations of models (c) and (d).

## Chapter 6 Discussion

Theoretically, variations of pore pressure gradients may cause near-surface deformation and affect the tilt intensity. Since at the study site the conditions of pump rate and the depths of well sources for each measurement location are the same, radial distances to the wells are expected to be the major factor influencing the tilt amplitudes (based on the eq. 2.7). However, the correlation between the distributions of tilt amplitudes and their distances to the pumping source do not show good correlation. The possible causes for the non-linearity are examined in following sections.

### 6.1 In-situ measurements evaluation

From the in-situ results of tilt observation, it can be stated that the tilt signals generally respond to pump rate, water table fluctuations, and stormy winds (Fig. 3.3). Due to the long monitoring period, it is found that the characteristics of these factors possess some irregularities appearing within certain specific time frames. Those irregularities and improvements to the instrument and installation settings are discussed next.

#### 6.1.1 Instrumental effects

The pump induced pore pressure gradient basically distributes in a conical shape. This was confirmed by examination of water table observation after the repair of the well level sensors. The variations of the water tables at the 5 observation wells became consistent, i.e. a more proportional relationship between the distance to the pump source and the observed pore pressure gradients become evident. The hydraulic flow presents a rather concentric pattern at this area. The ground deformation and the responses of tilt signals match a similar performance based on the hydraulic conditions. However, some heterogeneity still exists which might be associated with some other influencing factors.

In addition, good coupling between the instruments and the ground is proven by the earthquake induced signals during the monitoring period. A quake induced tilt

amplitude of about  $0.2 \mu\text{rad}$  corresponded to an earthquake with magnitude around 6.0 can be detected in this study. The resolution of the signals is not optimal though, since instruments with resolution higher than  $1 \mu\text{rad}$  is recommended for this purpose (Roeloffs and Langbein, 1994; Dal Moro and Zadro, 1999).

Further, the tiltmeters have been calibrated in the lab, the ground coupling or meteorological effect may alter their performance (Mentes et al., 1996). Specifically, tilt responses measured using 2 different principles (bubble and pendulum) may give rise to differing results depending on the type of tiltmeter used. Therefore, it was important to determine whether the type of tiltmeter used for collecting the data can have influence on the quality of the signals recorded. Since the design of the GGA Model is derived from the AGI Model, four locations with two types of tiltmeters (AGI and Lippmann) were interchanged: tiltmeter A1 was changed from location F8 to F12; A2 from F9 to F13; L8 from F12 to F9; and L5 from F13 to F8.

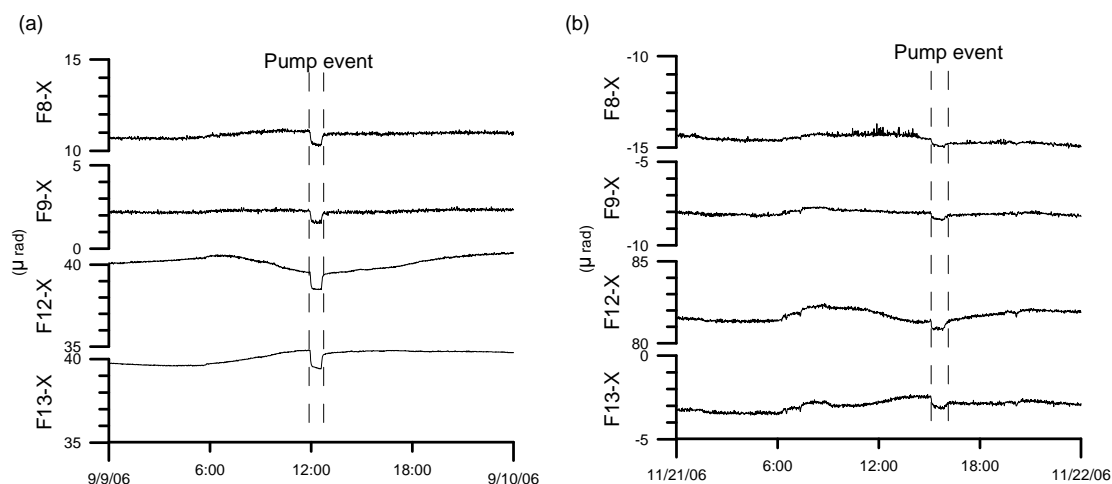


Fig. 6.1 The tilt signals in X-axis at F8, F9, F12, F13, respectively. (a) Before, and (b) after the interchange of the instruments

Figure 6.1 shows an example of induced signals in the X-axis from the 4 locations. The time intervals in (a) and (b) correspond to the recordings before and after the instrument adjustment, respectively. The pump rates of two selected pump events are different, but a similar decline in the ratio of amplitudes between (a) and (b) is valid for all 4 locations. Smoother curves of induced signals appearing in the data recorded from the bubble tiltmeter, visible after the pump event, show that this instrument may require a longer adjustment time to return to momentum equilibrium

state. Besides, its consuming voltage is higher and time periods for reaching temperature equilibrium are also relatively longer. Thus ca. 0.2 degree rising in temperature may appear after the weekly inspection. Compiling all data in annual time frame reveals a mild ladder-like pattern at time points of routine inspections (Fig. 4.2). Nevertheless, the general temperature trends in both types are comparable and the temperature effect is similarly eliminated eventually.

In general, the induced behavior and responds time point for these types resemble closely, so that the results of tilt signals differ little between the situations before or after the adjustment. This point is also proven by the statistics of amplitudes in Fig. 6.2. The models of instruments used before and after the switch are shown above their respective bars. At all locations (F8, F9, F12, F13), the amplitudes measured after the switching are similarly diminished. The difference between the black (preceding) and gray (afterwards) bars appears to be less than  $\pm 0.6 \mu\text{rad} \cdot \text{h} / 100 \text{ m}^3$ . It implies that the type of instrument does not affect the resolution of the signal. Therefore, instrument differences are not responsible for the diversity in signal distribution.

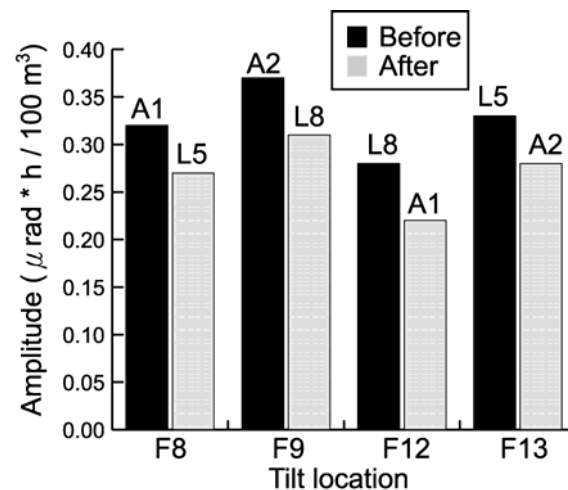


Fig. 6.2 Amplitude differences for the situations before and after the instrument interchange.

### 6.1.2 Vegetation effects

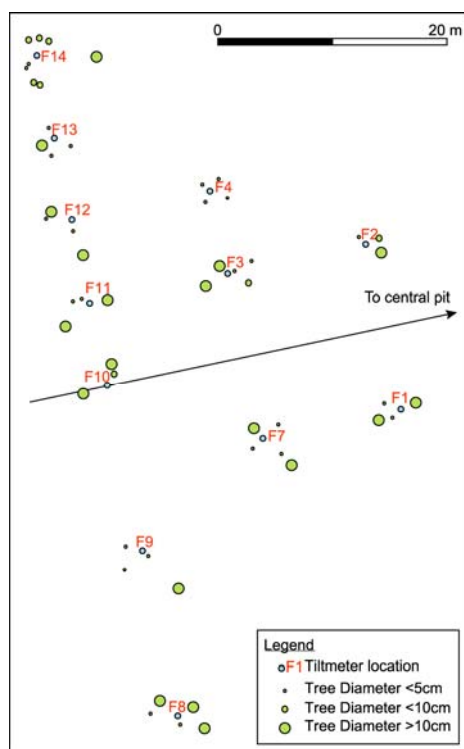


Fig. 6.3 The distribution of surrounding trees for the tiltmeters along the W flank.

Secondly, the effect of meteorology is considered. Some studies suggest that strong precipitation may induce tilt signals (Kümpel, 1986; Lacy, 1987; Rebscher et al., 2000). However, while this situation is not present in the study, wind conditions appear to influence tilt signals instead. Also, assuming the water consumption of vegetation is associated with location, the positions of instruments would matter (Kümpel et al., 1999). An example of the W flank is selected. In Fig. 6.3, the distances between the tiltmeter locations and the surrounding trees are drawn to scale, but the sizes of the trees are not. To simplify the visualization of tree distribution, three ranges of tree sizes were defined: tree diameters smaller than 5 cm, smaller than 10 cm, or larger than 10 cm. More detailed

information about the locations and the number of trees, and the distance between the trees and the instruments are depicted in Table 6.1.

Position	F1	F2	F3	F4	F7	F8	F9	F10	F11	F12	F13	F14
ca.0.5m	(1)	(1)	<b>X</b> <sub>(3)</sub>				(1)					
<1m				(1)	<b>X</b> <sub>(1)</sub>	(1)			(1)	(1)		(1)
<1.5m	<b>X</b> <sub>(2)</sub>	<b>X</b> <sub>(2)</sub>		(3)	(2)	<b>X</b> <sub>(1)</sub>		(1)	(1)		<b>X</b> <sub>(3)</sub>	(3)
<2m	<b>X</b> <sub>(1)</sub>				(1)		(2)	<b>2X</b> <sub>(2)</sub>	<b>X</b> <sub>(1)</sub>	<b>X</b> <sub>(1)</sub>	(1)	(1)
<3m			<b>X</b> <sub>(2)</sub>			<b>2X</b> <sub>(3)</sub>			<b>X</b> <sub>(1)</sub>	(1)		(2)
>3m					<b>X</b> <sub>(1)</sub>		<b>X</b> <sub>(1)</sub>			<b>X</b> <sub>(1)</sub>		<b>X</b> <sub>(1)</sub>

Table 6.1 Presence of trees and their distances to nearby tiltmeter locations. **X**: tree with a diameter larger than 20 cm, (1): number of trees.

The number in brackets refers to the number of surrounding trees. The bold capitalized **X** symbolizes a tree with a diameter larger than 20 cm; **2X** means two

trees are in this condition. When comparing the statistics with the tilt signals, a good correlation between the vegetation and the signals with strong influence from weather conditions is observed. Especially during seasons with storms or turbulent wind, the correlation between tree movement and tiltmeters is reflected in the signals, i.e. the amplitude might have more noises.

The extent of this effect is not determined by the numbers of surrounding trees but by the size of the tree and its distance to the instrument. Thus, if a tree with a diameter larger than 20 cm is situated less than 2 m away from the location of the instrument, it would have a large impact on the signal. This is evident at locations of F3, F8, and F10. These locations show most of the “windy” signals; the surrounding trees have trunk diameters larger than 30 cm and distribute within 2 m of the tiltmeters. In contrast, the locations with less varied diurnal swing signals have surrounding trunks nearby with smaller diameters (e.g. F4 and F9).

Therefore, additional adjustments for tiltmeter positions were made to minimize the vegetation effect. Eradication of local vegetation is reported to be an optimal method to reduce disturbances (Lacy, 1987). However, this was no option as the study area is in the protected neighborhood of water preservation. A alternative to minimize the effect of the surrounding trees is to place the instruments midpoint between the trees. The improvement was carried out after the experience from the W flank. The signal-to-noise ratio is higher, so that the average pump induced amplitudes along the NW and N flank are slightly enhanced to  $0.4 \mu\text{rad} \cdot \text{h}/100 \text{ m}^3$ .

### 6.1.3 Topographic effects

Lastly, the topographic effect is examined. Although according to the geological information that tectonic structures do not exist, the topography of the ground surface is not flat. Figure 6.4 illustrates the topography from a GPS survey. (The raw data are given in Appendix B). Each contour represents an increment of 0.1 m. The lighter colors correspond to higher elevations. Diverse topographic gradients are seen: the highest gradient is up to 0.1 m/m, such as the distance from F17 to F21; low gradients are 0.015 m/m (e.g. F15 to the central pit).

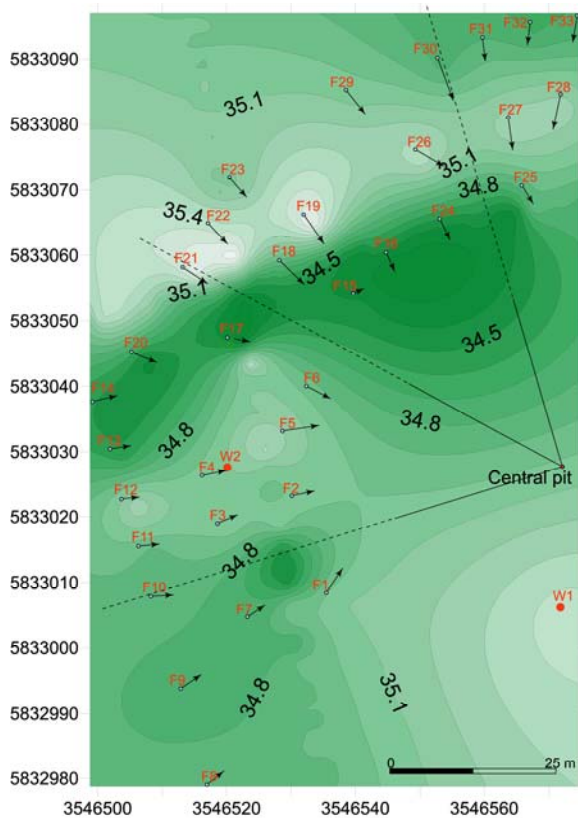


Fig. 6.4 Comparison between the topography and tilt results.

When the tiltmeter is installed near a hill side/foot, cavity or tectonic structure, it can contain an additional component of strain (Harrison, 1976a; Teufel and Warpinski, 1984; Sato and Hamaguchi, 2006). Therefore, it was felt necessary to determine whether pump induced signals are related to topographic effects and if partial responses are proportional to local creep deformations. Thus, the results of pump induced tilt movements from each location are superposed in Fig. 6.4. The azimuths obviously are not associated with the topographic effect, because the deviated directions do not match the variations of slope inclinations. Of the

aforementioned locations with anomalies (Chapter 4), only the results at F15 and F25 appear to have slight connections with topographic variations. The larger amplitudes of the NW (F18, F19) and the N flank (F26-F28) appear at the 2<sup>nd</sup> row, which coincidentally are the locations with higher elevations, but topographic effect is merely obvious at F19.

This indicates that the shallow depth (2 m) used for instrument installation is practical for most locations; however a deeper installation could be more suitable in some exceptional cases to diminish the topographic effect. In any case, the topographic effect has a minor contribution to the diversity of tilt results. Further, since the instrument resolutions are verified and the installation settings are optimized, another possible cause for tilt anomalies is the occurrence of underground inhomogeneities.

Some indications are shown by the results of additional geophysical measurements, especially in electrical resistivity. The zone with the upper soil extends from ground surface to ca. 5 m depth and obviously has a discontinuously lateral



distribution. This implies that the water content and porosity may be diverse from location to location. Because of the near-surface installation, the inhomogeneity may have influences on signals.

## 6.2 Model evaluation and application

By using POEL, idealistic variations of pore pressure and tilt in homogeneous conditions can be estimated. The existence of inhomogeneities can be estimated from discrepancies between model results and observations (Bakker, 2006). Another alternative method would be to conduct additional pump tests. Using additional testing of individual screen sections and much larger quantities of pump rates, the appearance and the distribution of inhomogeneities might also be discovered.

### 6.2.1 Validation of modeling results

Numerical methods are extensively applied because of their adaptability and effectiveness to simulate underground conditions (Rai and Hoffmann, 1989; Korom et al., 1991; Vasco and Finsterle, 2004). POEL is advantageous since it can consider each source independently and also allows easy constructing of a multi-layered model (Fabian, 2004). A spatial visualization of pore pressure and ground deformation is distinctly shown from the modeling results in Chapter 5. The proximity of a location to the forcing source generally results in a stronger ground deformation. Thus, in the central source models: model (a) presents stronger variations for locations near the central pit while those in model (b) are found near the end of the screen section. In the peripheral source models, both models (c) and (d) have similar results in that stronger variations are found near the start of the screen section.

However, because of the difference in the magnitude of the source between the central pit and the screen section, the distribution of gradients in the peripheral source models is actually more similar to model (a). Therefore, a condition that the force originating from the central pit is eliminated while the influence from the screen section persists is further analyzed using models (c) and (d).

Figure 6.5 illustrates the revised results of the pore pressure and tilt variations in both models. Considering only the forcing source of the screen section, the strongest

pore pressure change occurs exactly near the screen section location. But the gradients in model (c) are relatively widespread and become similar after a radial distance of 40 m. The concept of this model is similar to model (b) but involves subtracting an additional well of a smaller radius (20 m) from the larger well (radius of 70 m). The amplitudes (with negative values) of both wells would decrease from the central pit to the radial distance. However, the distribution of the force in the smaller well is more concentrated. Its amplitudes would be larger than the bigger well at similar radial distances (when close to the central pit). Therefore, the subtracted results of pore pressure and tilt become positive near the central pit. In comparison, the results in model (d) are a closer reflection of reality. The sources are found only concentrated at a depth around 20 m and also within radial distances of 20 m to 70 m.

Besides, although the larger amplitudes of tilt variations are both close to the end the screen section, the gradient distribution of model (d) is also more reasonable. This is because the screen section is better represented as in model (b) which mimics the screen section as a central pit. Moreover, the tilt variations in model (d) develop outwards from the location of the screen section. This suggests that model (d) among the varieties considered is an optimal analytic model for the situation at the study area. (The additional 2-D and 3-D combined results of the screen section and the boundary area are shown in Appendix F).

However, omission of the central pit influence appears to be unsuitable in the final model. In model (d), the tilt variation decreases from the end of the screen section to either side in radial distance. Instead, the actual distribution seems to decrease from the central pit to its radial direction. Consequently, the influence of the central pit must be included. The extent of this interplay of influence between the central pit and the screen section can be refined again. Thus, the analytic results of gradient values can be modeled to be even closer to the in-situ results. In summary, the results of the gradient distribution can be applied. In support of this opinion, a valid case is seen again in the final results from the tiltmeters along the NE flank and is discussed in the following section.

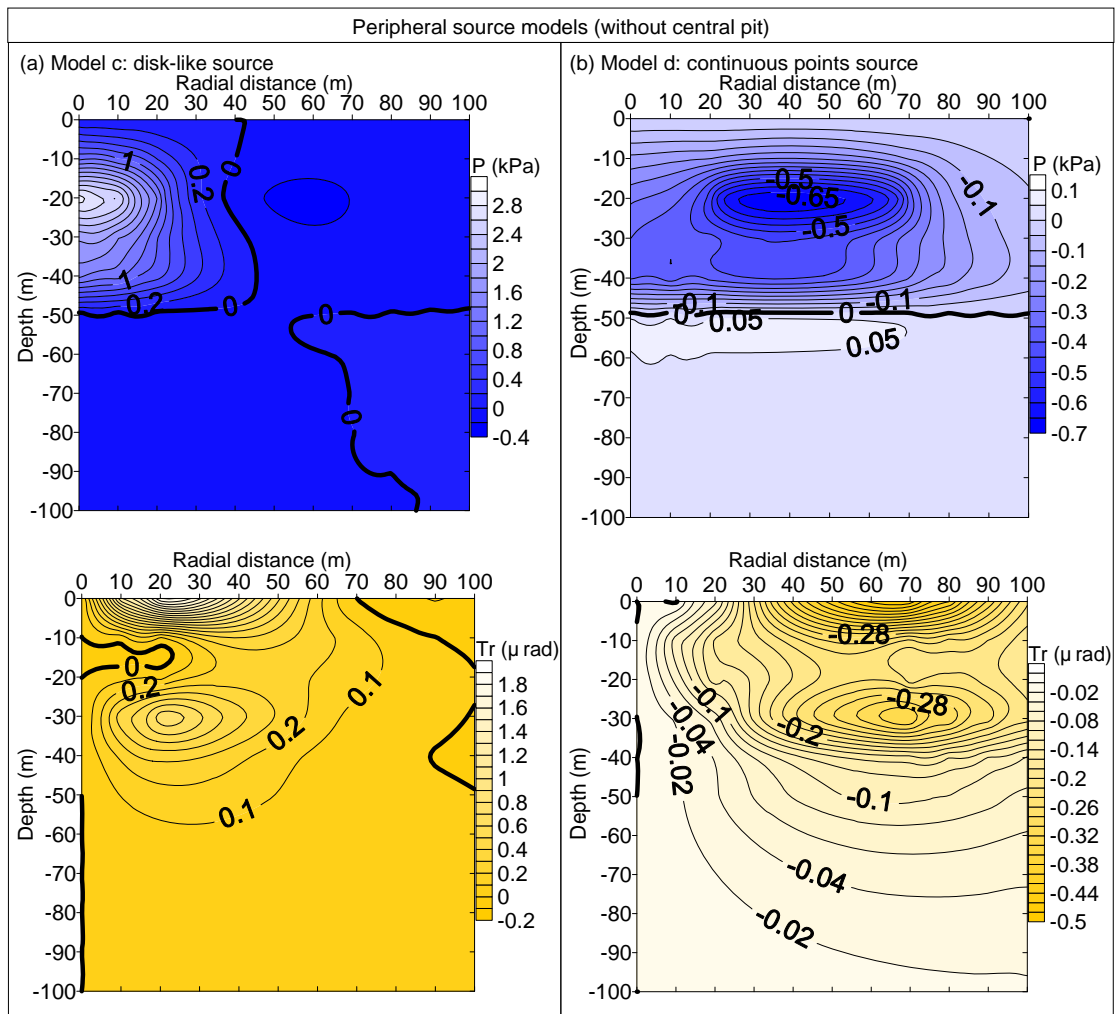


Fig. 6.5 Without the consideration of the central pit influence, the pore pressure and tilt results in (a) a disk-like source, and (b) a continuous points source.

### 6.2.2 Additional pump test of individual screen section

Pump tests have been suggested to be a non-destructive method to estimate underground parameters (Kümpel, 1997; Lecampion et al., 2005). Here, the selected pump events are associated with the water withdrawing from 8 horizontal wells to the central pit. The pore pressure change in the central pit is the result of those changes from each horizontal well. Accordingly, the pump effect from an individual screen section is masked by the pore pressure variations in the whole system. Fortunately, an opportunity to measure the effect from single screen sections arose from February to April 2008. During this period, the Water Works halted its regular pumping activities for the maintenance of the screen sections.

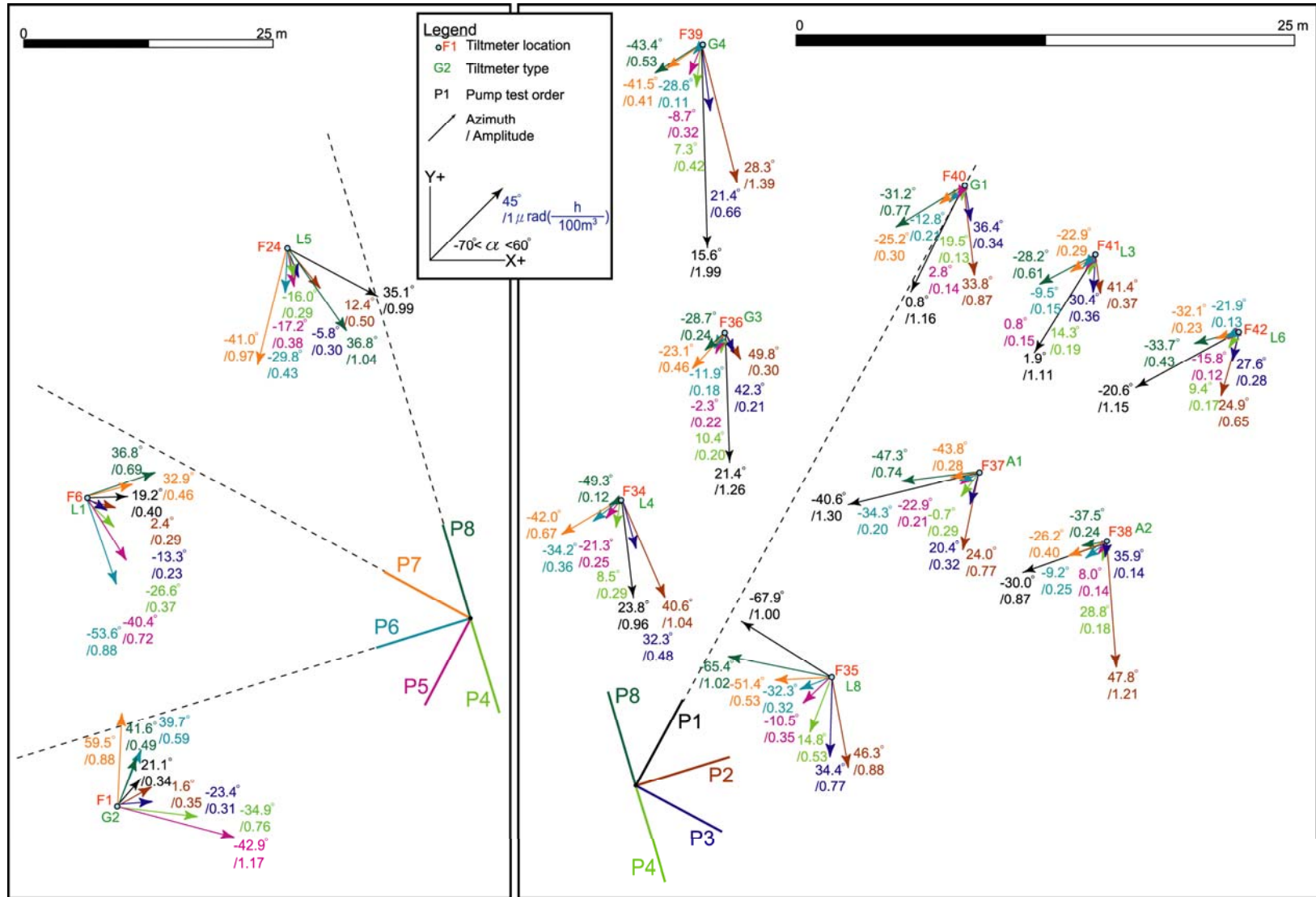


Fig. 6.6 Pump test results of P1 to P8. The results of tilt azimuths and amplitudes from locations F34 to F42 along NE flank (right diagram) and from locations F1, F6, F24, i.e. the reference tiltmeter sites (left diagram) are shown. (The scale on left diagram is halved that of the right.)

The efficiency of each screen section was tested and subsequently cleaned using a powerful flux of water. This allowed the influence from an individual horizontal well to be directly measured. The amplitude of the flux reached around 800 m<sup>3</sup>/h. The tests were conducted starting from P1 to P8 (Fig. 6.6). Results from the reference locations (F1, F6, and F24 from W, NW and E flank, respectively) are presented in more detail on the left half of the figure. The right half shows the results from locations on the NE flank (F34-F42). For better visualization, the scale of the right diagram (1:312.5) is two times larger than the left (1:625). Numbers next to the arrows indicate the azimuths and amplitudes.

Each pump test (P1-P8) is marked by a different color. The same coloring system is used to distinguish the numbers and arrows. Because the pump test starts at the NE flank (i.e. at P1), the tiltmeters positioned near this flank (F34 to F42) appear to react much stronger than the others. On its opposite flank (e.g. F1), the amplitude of the black arrow is reduced by about 1/3 (compared to F34). While the pump tests went in a counterclockwise direction, the amplitudes along this flank kept decreasing until the test series reached P6 phase and then started to increase again until P8.

The changes in the orientation of the azimuths basically follow the order of the pump test and point to the screen section where the pump test was being conducted at that particular moment. It proves the functioning and individual and degreed influence from each horizontal well - the closer the radial distance to the screen section being tested, the stronger the influence seen at that tiltmeter location.

Data from location F1 along the W flank is similar to the previous results. Ideally, the amplitude of light blue arrow (induced by P6) would be the strongest since the pump test was conducted exactly on this flank. However, the strongest signals appear at pump phase of P5 and then P7, which were the pump tests on the next two closest flanks from F1. A similar situation is observed on location F6 where the strongest amplitude did not point to the NW flank when P7 was being tested, but instead to P5, P6 and P8.

Comparing the influence of P5 and P6 on the NE flank (right side of the diagram), their results expectedly show the lowest values. But their amplitude was too much reduced such that the ratio of P5/P1 or P6/P1 became approximately 0.2 on the

NE flank, unlike the ratio on the W flank (approximately 0.5). This suggests the hydraulic conditions of each screen section may not necessarily be identical. Alternatively, some inhomogeneities may exist near locations F1 and F6, so that the hydraulic forcings from the nearest screen section do not fully reach these locations.

Another aspect regarding the occurrence of inhomogeneities comes from the final monitoring results at the NE flank (F34-F42), see Fig. 6.7. The data were measured from periods after the reactivation of regular pumping in the central pit and the 8 horizontal wells. The arrows indicate the locations with larger tilt azimuths and amplitudes. These locations are perpendicularly closer to the screen section, where the

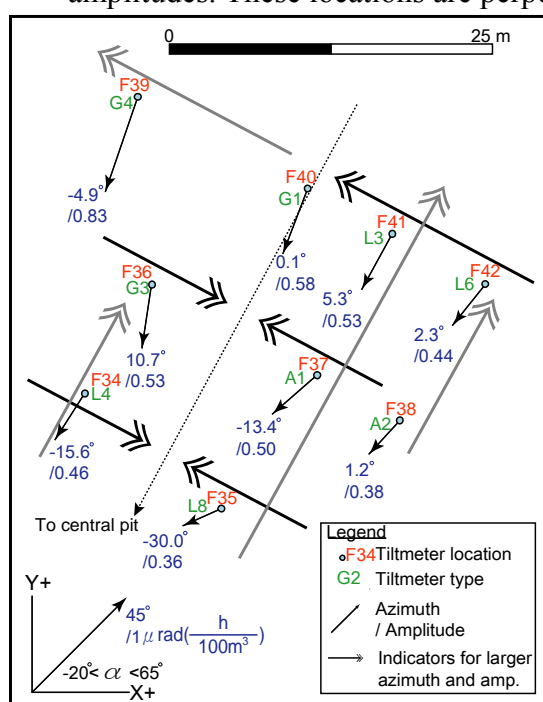


Fig. 6.7 The monitoring results at the NE flank reactivation of regular after pumping reactivated.

tilt azimuths and amplitudes are larger and subsequently decrease outwards from the screen section to the adjacent boundary area. The strongest amplitude and minimum azimuth now appear at location L6 right above the flank (F40).

But unlike the most results from the previous 3 flanks (Fig. 4.9 and Fig. 4.10), the situation here appears to be reversed. Stronger results appear near the end point of the screen section instead of near the central pit. This is more similar to the analytic result of model (d) without the consideration of the central pit influence (Fig. 6.5b). However, most tilt signals still point to the direction of the central

pit. So the central pit retains its influence but the more dominating source on this flank has become the screen section. The difference in scale of the forcing sources is reduced. Additionally, an inhomogeneous distribution definitely exists at this location since F39 has an extremely high value of tilt amplitude and the average amplitude of this flank enhances to  $0.5 \mu\text{rad} \cdot \text{h}/100 \text{m}^3$ .

## Chapter 7 Conclusion

This study illustrates an example of a successful monitoring of pump induced micro-deformation from horizontal wells. Using a large number of tiltmeters, the widespread near-surface movements induced by pumping were easily discovered. The tiltmeter arrays were positioned in a fan-shape manner along both sides of horizontal screen sections. By continuously reallocating the tiltmeters along different screen sections, the overall results can be viewed as completed half circle. According to the orientation of a flank, or the line and row, i.e. where the monitoring took place, the results can be analyzed with respect to the radial distance to the forcing source and the azimuths and amplitudes of the tilt signals.

Although the central pit is not an open well, it appears to be a source of stronger influence than the screen sections. The azimuths of induced signals mostly point to the central pit, with minor deviations to the screen section. The induced tilt amplitudes also show a larger decrease with radial distance when the location is farther (radial distance-wise) to the central pit and have smaller decreases when recorded away from the screen section.

All this suggests that while the ground water is gathered by the screen sections, these sections cause ground deformation within their neighborhood. However, simultaneously water is assembled by the central pit with an effect 8 times larger than that of a single screen section. Clearly, the amplitude of ground deformation caused by it is comparatively large. Generally, the tilt movements are influenced by both the central pit and the screen sections. From the distributions of tilt variations, the forcing source that has the larger effect in ground deformation can be identified.

As to the hydraulic flow system, the recordings of the pressure transducers suggest a rather concentric variation of the water table. For observation wells closer to the central pit, the fluctuations of water table level are larger. The average depth of the water table level is about 6 m below ground surface, which is confirmed by results from ground penetrating radar. Nevertheless, pore pressure variations from modeling data illustrate a more complicated gradient distribution. For a better resolution of the state, more pressure transducers would need to be installed in a

symmetrical manner across the screen sections.

When external factors are eliminated or reduced (such as meteorological influences and surfacial effects from topography and vegetation), the tilt signals are seen to be principally influenced by the changes in pump rate. Most induced azimuths are within  $10^\circ$  of the direction to the central pit, yet some are larger than  $20^\circ$ . The average amplitude along different flanks of the screen sections varies from 0.33 to 0.5  $\mu\text{rad}$  in response to a change in pumping rate of  $100 \text{ m}^3/\text{h}$ .

Other interesting observations were also made in the study area. For example, some inhomogeneities in the subsurface appear to exist. Occasionally, after cleaning, the screen sections became more dominating forcing sources than the central pit. Due to the uneven topography and the obstruction by vegetation, the coupling between the instruments and the ground is not optimal. The existence of inhomogeneities has also been confirmed by additional geophysical surveys, pump tests and numerical modeling. Although the results of these surveys were not as detailed as expected, some appearances of inhomogeneities are seen. A seismogram shows possible occurrences of minor structures and a DC resistivity study presents a formation with discontinuously lateral distribution at shallow surface.

Additional pump tests show good correlations between the tilt locations and its induced signals. Each pump test can be compared to model (a) where increasing proximity to the single point source (P1-P8) leads to larger azimuth and amplitude. The azimuth basically indicates the direction of the source. The appearance of deviations demonstrates the likely existence of inhomogeneous conditions. It is easy to comprehend this using the numerical modeling. The ideal variations of pore pressure and tilt in time are illustrated via gradient distributions on X-Z and X-Y planes. The models (a), (c), and (d) indicate simulated situations where the central pit is the stronger forcing source while model (b) has the screen section stronger. By partition progress of the screen section, the simulated results approach closer to the observed scenario, i.e. the model (d) is an optimal analytic solution. A decreasing tilt amplitude is obtained both with increasing radial distance to the central pit and to the screen section. However, the scale difference between the effect due to the central pit and the screen sections can still be refined. In general, the individual or dual effects



of forcing sources can be easily estimated through numerical modeling. The spatial distributions of the pore pressure changes and tilt movements are clearly seen.

- AGI (1999a). User's manual no. B-91-1004, rev. B., model 722 borehole tiltmeter. Applied Geomechanics Inc., Santa Cruz, United States.
- AGI (1999b). User's manual no. B-94-1002, rev. B., model 84208 long board signal conditioner. Applied Geomechanics Inc., Santa Cruz, United States.
- AGI (2000). User's manual no. B-92-1003, rev. B., series 755, 756 and 757 miniature tilt sensors. Applied Geomechanics Inc., Santa Cruz, United States.
- Arens, T., F. Hettlich, C. Karpfinger, U. Kockelkorn, K. Lichtenegger and H. Stachel (2008). *Mathematik*. Spektrum Akademischer Verlag, Spain, 1498.
- Astley, B. N. and A. J. Delaney (2007). GPR and DC resistivity application to discontinuous permafrost delineation, Eielson Air Force Base, Alaska. Proceedings of SAGEEP, Environmental and Engineering Geophysical Society, Denver, CO, United States, 8.
- Bakker, M. (2006). An analytic element approach for modeling polygonal inhomogeneities in multi-aquifer systems. *Advances in Water Resources*, 29(10): 1546-1555.
- Bakker, M., V. A. Kelson and K. H. Luther (2005). Multilayer analytic element modeling of radial collector wells. *Ground Water*, 43: 926-934.
- Ball, D. F. and R. Herbert (1992). The use and performance of collector wells within the regolith aquifer of Sri Lanka. *Ground Water*, 30: 683-689.
- Batayneh, A. T. (2001). Resistivity imaging for near-surface resistive dyke using two-dimensional DC resistivity techniques. *Journal of Applied Geophysics*, 48: 25.
- Best, A. I., J. Sothcott and C. McCann (2007). A laboratory study of seismic velocity and attenuation anisotropy in near-surface sedimentary rocks. *Geophysical Prospecting*, 55(5): 609-625.
- Bilham, R. G. and R. J. Beavan (1979). Strains and tilts on crustal blocks. *Tectonophysics*, 52(1-4): 121-138.
- Boettcher, J., O. Strebel and W. H. M. Duynisveld (1985). Grundwasserstroemung und Stoffumsetzungen in dem Lockergesteinsaquifer des Fuhrberger Feldes. Ground water flow and composition in porous aquifers in Fuhrberg. Hanover, Federal Republic of Germany, 32: 27.

- Carreon-Freyre, D., M. Cerca and M. Hernandez-Marin (2003). Correlation of near-surface stratigraphy and physical properties of clayey sediments from Chalco Basin, Mexico, using ground penetrating radar. *Journal of Applied Geophysics*, 53: 121.
- Chambers, J. E., O. Kuras, P. I. Meldrum, R. D. Ogilvy and J. Hollands (2006). Electrical resistivity tomography applied to geologic, hydrogeologic, and engineering investigations at a former waste disposal site. *Geophysics*, 71: B231.
- Chambers, J. E., R. D. Ogilvy, O. Kuras, J. C. Cripps and P. I. Meldrum (2002). 3D electrical imaging of known targets at a controlled environmental test site. *Environmental Geology Berlin*, 41: 690.
- Chesnaux, R., J. W. Molson and R. P. Chapuis (2005). An analytical solution for ground water transit time through unconfined aquifers. *Ground Water*, 43: 511-517.
- Chourak, M., V. Corchete, J. Badal, F. Seron and F. Gomez (2003). Imaging of the near-surface shear-wave velocity structure of the Granada Basin (southern Spain). *Bulletin of the Seismological Society of America*, 93: 430.
- Dal Moro, G. and M. Zadro (1999). Remarkable tilt-strain anomalies preceding two seismic events in Friuli (NE Italy); their interpretation as precursors. *Earth and Planetary Science Letters*, 170: 119.
- Dasios, A., C. McCann, T. R. Astin, D. M. McCann and P. Fenning (1999). Seismic imaging of the shallow subsurface; shear-wave case histories. *Geophysical Prospecting, European Association of Exploration Geophysicists, The Hague, Netherlands*, 47: 565.
- Devlin, J. F. and C. D. McElwee (2007). Effects of measurement error on horizontal hydraulic gradient estimates. *Ground Water*, 45(1): 62-73.
- d'Oreye, N. F. and W. Zürn (2005). Very high resolution long-baseline water-tube tiltmeter to record small signals from Earth free oscillations up to secular tilts. *Review of Scientific Instruments*, 76: 024501.
- Evans, K. (1983). On the development of shallow hydraulic fractures as viewed through the surface deformation field; Part 1, Principles. *Journal of Petroleum Technology*, 35: 406.
- Evans, K. and G. Holzhausen (1983). On the development of shallow hydraulic fractures as viewed through the surface deformation field; Part 2, Case histories. *Journal of Petroleum Technology*, 35: 411.

- Fabian, M. (2004). Near surface tilt and pore pressure changes induced by pumping in multi-layered poroelastic half-spaces. *Berichte aus der Geowissenschaft, Universitaet Bremen*, 111.
- Fabian, M. and H.-J. Kumpel (2003). Poroelasticity; observations of anomalous near surface tilt induced by ground water pumping. *Journal of Hydrology*, 281: 187.
- Fabian, M. and H. Villinger (2007). The Bremen ocean bottom tiltmeter (OBT) a technical article on a new instrument to monitor deep sea floor deformation and seismicity level. *Marine Geophysical Researches*, 28(1): 13-26.
- Furman, A., T. P. A. Ferre and G. L. Heath (2007). Spatial focusing of electrical resistivity surveys considering geologic and hydrologic layering. *Geophysics*, 72: F65.
- Galvin, R. J., B. Gurevich and C. M. Sayers (2007). Fluid-dependent shear-wave splitting in a poroelastic medium with conjugate fracture sets. *Geophysical Prospecting*, 55: 333.
- Gazonas, G. A., C. A. Wright and M. D. Wood (1988). Tiltmeter mapping and monitoring of hydraulic fracture propagation in coal; a case study in the Warrior Basin, Alabama. *Rocky Mt. Assoc. Geol., Denver, CO, United States*, 159.
- Haines, S. S., B. L. Burton and L. E. Hunter (2007). Seismic shear wave reflection imaging at the former Fort Ord, Monterey, California. *Open-File Report, U. S. Geological Survey, Reston, VA, United States, 2007-1068*: 13
- Harris, J. B. and J. L. Sorrells (2003). Shear-wave seismic reflection imaging of the Big Creek escarpment near Helena Arkansas; evidence for a tectonic origin. *Abstracts with Programs - Geological Society of America, Geological Society of America (GSA), Boulder, CO, United States*, 35: 21.
- Harrison, J. C. (1976a). Cavity and topographic effects in tilt and strain measurement. *Journal of Geophysical Research*, 81: 319.
- Harrison, J. C. (1976b). Tilt observations in the Poorman Mine near Boulder. Colorado. *Journal of Geophysical Research*, 81: 329.
- Herbert, R. and D. F. Ball (1992). The use and performance of collector wells within the regolith aquifer of Sri Lanka. *Ground Water*, 30: 683.
- Holzhausen, G. R., M. D. Wood, J. M. Raisbeck and C. C. Card (1980). Results of deformation monitoring during steam stimulation during a single-well test. *Applied Oil Sands Geoscience Conference, Edmonton, Canada*, 11-13.

- Hubbard, S. S., J. E. Peterson, Jr., E. L. Majer, P. T. Zawislanski, K. H. Williams, J. Roberts and F. Wobber (1997). Estimation of permeable pathways and water content using tomographic radar data. *Leading Edge Tulsa, OK*, 16: 1623.
- Karasaki, K., B. Freifeld, A. Cohen, K. Grossenbacher, P. Cook and D. Vasco (2000). A multidisciplinary fractured rock characterization study at Raymond field site, Raymond, CA. *Journal of Hydrology*, 236: 17.
- Kawecki, M. W. and H. N. Al-Subaikhy (2005). Unconfined linear flow to a horizontal well. *Ground Water*, 43: 606-610.
- Kelson, V. A., M. Bakker and K. H. Luther (2005). Bessel analytic element system and method for collector well placement, WHPA, Inc.
- Kim, J. M. (1997). Numerical simulation of the Noordbergum effect resulting from groundwater pumping in a layered aquifer system. *Journal of Hydrology*, 202: 231.
- Korom, S. F., J. Boettcher, O. Strebel, W. H. M. Duynisveld and E. O. Frind (1991). Modeling of multicomponent transport with microbial transformation in groundwater; the Fuhrberg case; discussion and reply. *Water Resources Research*, 27: 3271.
- Kümpel, H.-J. (1982). Tilt measurements; what do they tell us? *Terra Cognita*, European Union of Geosciences, Strasbourg, France, 2: 391.
- Kümpel, H.-J. (1986). Model calculations for rainfall induced tilt and strain anomalies. *Proceedings - International Symposium on Earth Tides*, 10: 889.
- Kümpel, H.-J. (1989). *Verformungen in der Umgebung von Brunnen*. Berichte aus der Geowissenschaft, Universitaet Kiel.
- Kümpel, H.-J. (1991). Poroelasticity; parameters reviewed. *Geophysical Journal International*, 105: 783.
- Kümpel, H.-J., P. Varga, K. Lehmann and G. Menten (1996). Ground tilt induced by pumping- preliminary results from the Nagycenk test site, Hungary. *Acta Geodaetica et Geophysica Hungarica*, Akademiai Kiado, Budapest, Hungary, 31: 67.
- Kümpel, H.-J. (1997). In-situ deformation measurements for evaluation of hydraulic rock parameters. *Proceedings of the International Geological Congress*, Beijing, 23: 481.

- Kümpel, H.-J. (1998). Well tides in an area of high reservoir induced seismicity. H. K. Gupta, I. Radhakrishna, R. K. Chadha and G. Grecksch. In Proc. 13th Int. Symp. Earth Tides, Ducarme, B. and Paquet, P. (eds.), Brussels, 125.
- Kümpel, H.-J., G. Grecksch, K. Lehmann, D. Rebscher and K. C. Schulze (1999). Studies of in-situ pore pressure fluctuations at various scales. *Oil & Gas Science and Technology-Review IFP*, 54: 679.
- Kümpel, H.-J. (2001). Point stability at shallow depths: experience from tilt measurements in the Lower Rhine Embayment, Germany, and implications for high-resolution GPS and gravity recordings. *Geophysical Journal International*, 146: 699.
- Kümpel, H.-J. and M. Fabian (2003). Tilt monitoring to assess the stability of geodetic reference points in permafrost environment. *Physics and Chemistry of the Earth*, 28: 1249.
- Kümpel, H.-J. (2004). Coupled mechanical phenomena in deformable porous media. *Modelling coupled phenomena in saturated porous materials*. Institute of Fundamental Technological Research, Warsaw, Poland, 20: 351-416.
- Kümpel, H.-J., G. Lohr and R. Wang (1986). Tilt measurements at various depths in the same borehole. *Proceedings - International Symposium on Earth Tides*, 10: 271.
- Lacy, L. L. (1987). Comparison of hydraulic-fracture orientation techniques. *SPE Drilling & Completion*. Society of Petroleum Engineers of the American Institute of Mining, Metallurgical and Petroleum Engineers (AIME), Richardson, TX, United States, 2: 66.
- Lang, H. D. (1981). *Geologische Karte von Niedersachsen 1 : 25000 - Erläuterungen zu Blatt Nr. 3324 Lindwedel*. Deutschland, Dieterische Universitaets-Buchdruckerei W. Fr. Kaestner, Rosdorf ueber Goettingen, 127.
- Lecampion, B., R. Jeffrey and E. Detournay (2005). Resolving the Geometry of Hydraulic Fractures from Tilt Measurements. *Pure and Applied Geophysics*, 162: 2433-2452.
- Lecampion, B. and A. Constantinescu (2005). Sensitivity analysis for parameter identification in quasi-static poroelasticity. *International Journal for Numerical and Analytical Methods in Geomechanics*, 29: 163.
- Lehmann, K. (2001). Porendruckindizierte Neigungssignale in geringen Tiefen und ihre Modellierung im homogenen Halbraum. *Berichte aus der Geowissenschaft*, Shaker Verlag, Aachen, 6-10.

- Long, M. and S. Donohue (2007). In situ shear wave velocity from multichannel analysis of surface waves (MASW) tests at eight Norwegian research sites. *Canadian Geotechnical Journal = Revue Canadienne de Geotechnique*, 44: 533.
- Malkowski, M. A., D. H. Jayawickreme, R. L. Van Dam and D. W. Hyndman (2007). Monitoring seasonal changes in soil moisture across a forest-grassland boundary using electrical resistivity soundings. *Abstracts with Programs - Geological Society of America*, 39: 61.
- Maruyama, T. (1994). Fluid pressure responses of a water-saturated porous elastic multi-layer half-space to water pumping and atmospheric loading. *Journal of Physics of the Earth*, 42: 331.
- Mentes, G. (2004). Investigation of the stability of borehole tiltmeters working in unpacked boreholes inundated with ground water. *Acta Geodaetica et Geophysica Hungarica, Akademiai Kiado, Budapest, Hungary*, 39: 49.
- Mentes, G., K. Lehmann, P. Varga and H. J. Kumpel (1996). Some calibration of the Applied Geomechanics Inc. borehole tiltmeter model 722. *Acta Geodaetica et Geophysica Hungarica, Akademiai Kiado, Budapest, Hungary*, 31: 79.
- Moore, J. E. (2003). IAH congress; groundwater; past achievements and future challenges. *Environmental Geology Berlin*, 44: 85.
- Munroe, J. S., J. A. Doolittle, M. Z. Kanevskiy, K. M. Hinkel, F. E. Nelson, B. M. Jones, Y. Shur and J. M. Kimble (2007). Application of ground-penetrating radar imagery for three-dimensional visualisation of near-surface structures in ice-rich permafrost, Barrow, Alaska. *Permafrost and Periglacial Processes*, 18: 309.
- Muralidharan, D., R. Rangarajan, J. V. S. Murthy and Y. Prabhakar Rao (2005). Mapping of hydrodynamic changes around radial arms of collector well by streaming potential survey. *Current Science, National Geophysical Research Institute, Hyderabad, India*, 88: 1901.
- Okada, Y. (1992). Internal deformation due to shear and tensile faults in a half-space. *Bulletin of the Seismological Society of America*, 82: 1018.
- Park, Y.-H., S.-J. Doh and S.-T. Yun (2007). Geoelectric resistivity sounding of riverside alluvial aquifer in an agricultural area at Buyeo, Geum River watershed, Korea; an application to groundwater contamination study. *Environmental Geology Berlin*, 53: 849.
- Pessoa, M. C. and J. M. Travassos (2007). A GPR analysis of a Quaternary stratigraphy at the coast of Rio de Janeiro. *Leading Edge Tulsa, OK*, 26: 1000.

- Pesti, G., W. E. Kelly and I. Bogardi (1994). Observation network design for selecting locations for water supply wells. *Environmetrics*, 5(2): 91-110.
- Priest, J. A., A. I. Best and C. R. I. Clayton (2006). Attenuation of seismic waves in methane gas hydrate-bearing sand. *Geophysical Journal International*, 164(1): 149-159.
- Rai, S. N. and B. Hoffmann (1989). Numerical simulation of groundwater flow in Fuhrberg Field, Hanover. Oxford and IBH Publ. Co., New Delhi, India, 595.
- Rebscher, D., M. Westerhaus, W. Welle and I. G. M. A. Nandaka (2000). Monitoring ground deformation at the decade volcano Gunung Merapi, Indonesia. *Physics and Chemistry of the Earth, Part A: Solid Earth and Geodesy*, 25(9-11): 755-757.
- Reynolds, J. M. (1997). An introduction to applied and environmental geophysics. England, John Wiley & Sons Ltd, Baffins Lane, Chichester, West Sussex PO 19 1UD, England, 796.
- Rice, J. R. (1976). Some basic stress diffusion solutions for fluid-saturated elastic porous media with compressible constituents. *Reviews of Geophysics and Space Physics*, 14: 227-241.
- Rifai, H., S. Grüneberg, H. C. Chen and H.-J. Kümpel (2007). Einsatz von Neigungsmessern in Schwarmstedt. Hannover, GGA.
- Rifai, H., G. Zoth and W. Kessels (2004). Bericht ueber die Durchfuehrung hoch aufloesender Wasserspiegelmessungen im Grossraum Cuxhaven. Hannover, GGA.
- Roeloffs, E. A. (2006). Evidence for aseismic deformation rate changes prior to earthquakes. *Annual Review of Earth and Planetary Sciences*, 34: 591.
- Roeloffs, E. A. and B (1988). Fault stability changes induced beneath a reservoir with cyclic variations in water level. *Journal of Geophysical Research*, 93: 2107.
- Roeloffs, E. A. and B (1989). Hydrologic effects on water level changes associated with episodic fault creep near Parkfield, California. *Journal of Geophysical Research*, 94: 12,387.
- Roeloffs, E. A. and B (1998). Persistent water level changes in a well near Parkfield, California, due to local and distant earthquakes. *Journal of Geophysical Research*, 103: 869.
- Roeloffs, E. A. and J. Langbein (1994). The earthquake prediction experiment at Parkfield, California. *Reviews of Geophysics*, 32: 315.



- Sato, M. and H. Hamaguchi (2006). Weak long-lived ground deformation related to Iwate volcanism revealed by Bayesian decomposition of strain, tilt and positioning data. *Journal of Volcanology and Geothermal Research*, 155(3-4): 244-262.
- Schafer, D. C. (1996). Determining 3D capture zones in homogeneous, anisotropic aquifers. *Ground Water*, 34: 628.
- Senosy, M. M. and S. Riad (1998). An electrical resistivity study to determine characteristics of near-surface layers in the present and the new proposed sites of Hibis Temple, New Valley, Egypt. *Bulletin of the Faculty of Science. F, Geology, Assiut University, Egypt*, 27: 73.
- Skempton, A. W. (1954). The pore-pressure coefficients A and B. *Geotechnique*, 4: 143-147.
- Takemoto, S., M. Lee, C.-Y. Chen, M.-C. Kao, A. Mukai, T. Ikawa, T. Kuroda and T. Abe (2006). Tidal strain observations in Chu-Chie, Taiwan. *Journal of Geodynamics*, 41(1-3): 198-204.
- Teufel, L. W. and N. R. Warpinski (1984). Determination of in situ stress from anelastic strain recovery measurements of oriented core; comparison to hydraulic fracture stress measurements in the Rollins Sandstone, Piceance Basin, Colorado. *Proceedings - Symposium on Rock Mechanics*, 25: 176.
- Turesson, A. (2007). Comparative analysis of the multi-offset ground-penetrating radar and shear-wave reflection methods. *Journal of Environmental & Engineering Geophysics*, 12: 163.
- Van Berk, W. and C. Hansen (2006). *Prozessorientierte Geosystemerkundung. Hydrogeochemische Stoffflussmodelle*, Springer: 19-47.
- Vasco, D. W. (2004). Estimation of flow properties using surface deformation and head data; a trajectory-based approach. *Water Resources Research*, 40.
- Vasco, D. W. and S. A. Finsterle (2004). Numerical trajectory calculations for the efficient inversion of transient flow and tracer observations. *Water Resources Research*, 40.
- Vasco, D. W., K. Karasaki and O. Nakagome (2002). Monitoring production using surface deformation: the Hijiori test site and the Okuaizu geothermal field, Japan. *Geothermics*, 31(3): 303-342.
- Verruijt, A. (1969). Elastic storage of aquifers. In: De Wiest, R. (ed.), *Flow through porous media*. New York, Academic Press, 331.

Wang, H. F. (2000). Theory of linear poroelasticity. Princeton, New Jersey, U.S.A, Princeton University Press.

Wang, R. and H.-J. Kämpel (2003). Poroelasticity; efficient modeling of strongly coupled, slow deformation processes in a multilayered half-space. *Geophysics*, 68: 705.

## Appendix A: Events from monitoring schedule

**An, Gn, Ln:** tiltmeter type; **Fn:** tiltmeter location; **Wn:** observation well (numbers in preceding line indicate the serial numbers of pressure transducers)

**Abbreviation:** **b:** battery change; **d:** data problem; **dl:** data box problem; **e:** DC resistivity survey; **E:** end; **g:** GPS survey; **I:** electric contact gauge measuring; **m:** memory empty; **p:** additional pump test; **pp:** P-wave survey; **r:** read out data; **R:** GPR survey; **s:** start monitoring; **ss:** S-wave survey; **tp:** temperature problem

**Filled color:** **green:** on; **red:** off; **yellow:** instrument adjustment; **orange:** dryer tube attached

	G2	G4	L3	L4			G1	A1	A2	L1	L6	L8	L5	G3			19	67	77	75	80
	F1	F2	F3	F4	F5	F6	F7	F8	F9	F10	F11	F12	F13	F14	F15	F16	W1	W2	W3	W4	W5
15.05.06																			s		
17.05.06																	s			s	
	G2	G4	L3	L4			G1	A1	A2	L1	L6	L8	L5	G3			27	67	77	75	80
	F1	F2	F3	F4	F5	F6	F7	F8	F9	F10	F11	F12	F13	F14	F15	F16	W1	W2	W5	W3	W4
22.05.06																	r		r	r	
23.05.06																		s			s
24.05.06	s		s				s			s							r	rb	r	r	r
30.05.06									s		s	s					r	r	r	r	r
02.06.06								s					s	s							
06.06.06				s																	
07.06.06		s																			
	G2	G4	L3	L4			G1	A1	L8	L1	L6	L8	L5	G3			27	67	77	75	80
	F1	F2	F3	F4	F5	F6	F7	F8	F9	F10	F11	F12	F13	F14	F15	F16	W1	W2	W3	W4	W5
07.11.06	b	b	b	b			dl	b	s	b	b		b	b							
	G2	G4	L3	L4			G1	A1	L8	L1	L6	A1	L5	G3			27	67	77	75	80
	F1	F2	F3	F4	F5	F6	F7	F8	F9	F10	F11	F12	F13	F14	F15	F16	W1	W2	W3	W4	W5
08.11.06												s									
	G2	G4	L3	L4			G1		L8	L1	L6	A1	A2	G3			27	67	77	75	80
	F1	F2	F3	F4	F5	F6	F7	F8	F9	F10	F11	F12	F13	F14	F15	F16	W1	W2	W3	W4	W5
10.11.06													s				rl	r	rl	rl	rl
	G2	G4	L3	L4			G1	L5	L8	L1	L6	A1	A2	G3			27	67	77	75	80
	F1	F2	F3	F4	F5	F6	F7	F8	F9	F10	F11	F12	F13	F14	F15	F16	W1	W2	W3	W4	W5
20.11.06								s													
	G2	G4	L3	L4			G1	L5	L8	L1	L6	A1	A2	G3			27	67	77	75	20
	F1	F2	F3	F4	F5	F6	F7	F8	F9	F10	F11	F12	F13	F14	F15	F16	W1	W2	W3	W4	W5
24.11.06																	rml	rml	rml	rml	srm
13.12.06ss	b	b	b	b			b	b	b	b	b	b					r	r	r	r	r
19.12.06e																					

	G2	G4	L3	L4			G1	L5	L8	L1	L6	A1	A2	G3			27	67	77	75	64	
	F1	F2	F3	F4	F5	F6	F7	F8	F9	F10	F11	F12	F13	F14	F15	F16	W1	W2	W3	W4	W5	
17.01.07	b	b	b	b			b	b	b	b	b	b	b				r	rm	rbm	<del>rbm</del>	sml	
	G2	G4	L3	L4	G3		G1	L5	L8	L1	L6	A1	A2	G3			27	67	77	75	64	
	F1	F2	F3	F4	F5		F7	F8	F9	F10	F11	F12	F13	F14			W1	W2	W3	W4	W5	
01.02.07					s																	
	G2	G4	L3	L4	G3	L1	G1	L5	L8	L1	L6	A1	A2		L5		27	67	77	75	64	
	F1	F2	F3	F4	F5	F6	F7	F8	F9	F10	F11	F12	F13		F15		W1	W2	W3	W4	W5	
02.02.07						s									s							
	G2	G4	L3	L4	G3	L1	G1	L8	L6	A1	A2				L5	L8	27	67	77	75	64	
	F1	F2	F3	F4	F5	F6	F7	F9	F11	F12	F13				F15	F16	W1	W2	W3	W4	W5	
05.02.07																s						
	G2	G4	L3	L4	G3	L1	G1	L6	A1	A2					L5	L8	L6	27	67	77	75	64
	F1	F2	F3	F4	F5	F6	F7	F11	F12	F13					F15	F16	F17	W1	W2	W3	W4	W5
27.03.07																s						
	G2	G4	L3	L4	G3	L1	G1	A1	A2					L5	L8	L6	A1	27	67	77	75	64
	F1	F2	F3	F4	F5	F6	F7	F12	F13					F15	F16	F17	F18	W1	W2	W3	W4	W5
28.03.07R	b	b	b	b	b	b	b							s	s		s					
	G2	G4	L3	L4	G3	L1	G1	A2			L5	L8	L6	A1	A2	G1	27	67	77	75	64	
	F1	F2	F3	F4	F5	F6	F7	F13			F15	F16	F17	F18	F19	F20	W1	W2	W3	W4	W5	
29.03.07															s	s						
	G2	G4	L3	L4			G3	L1	L5	L8	L6	A1	A2	G1	L3	L4	27	67	77	75	64	
	F1	F2	F3	F4			F5	F6	F15	F16	F17	F18	F19	F20	F22	F23	W1	W2	W3	W4	W5	
30.03.07															s	s						
	G2	G4	G3	L1	L5	L8	L6	A1	A2	G1	G4	L3	L4				27	67	77	75	64	
	F1	F2	F5	F6	F15	F16	F17	F18	F19	F20	F21	F22	F23				W1	W2	W3	W4	W5	
02.04.07											s											
	G2		G3	L1	L5	L8	L6	A1	A2	G1	G4	L3	L4				27	68	77	75	64	
	F1		F5	F6	F15	F16	F17	F18	F19	F20	F21	F22	F23				W1	W2	W3	W4	W5	
25.05.07											tp							sml				
	G2		G3	L1	L5	L8	L6	A1	A2	G1	G4	L3	L4			L5	27	68	77	75	64	
	F1		F5	F6	F15	F16	F17	F18	F19	F20	F21	F22	F23		F24		W1	W2	W3	W4	W5	
11.07.07	b			b		b	b	b	b		b	b	b			s						
	G2		G3	L1	L8	L6	A1	A2	G1	G4	L3	L4		L5	G3	G1	27	68	77	75	64	
	F1		F5	F6	F16	F17	F18	F19	F20	F21	F22	F23		F24	F26	F29	W1	W2	W3	W4	W5	
12.07.07												d			s	s						
	G2	L1	L8	L6	A1	A2	G4	L3	L4					L5	G3	G1	G4	27	68	77	75	64

	F1	F6	F16	F17	F18	F19	F21	F22	F23				F24	F26	F29	F30	W1	W2	W3	W4	W5
13.07.07									d							s					
	G2	L1	L8	L6	A1	A2	L3	L4			L5	G3	A1	A2	G1	G4	27	68	77	75	64
	F1	F6	F16	F17	F18	F19	F22	F23			F24	F26	F27	F28	F29	F30	W1	W2	W3	W4	W5
16.07.07								d					s	s							
	G2	L1	L8	L6			L3	L4			L5	G3	A1	A2	G1	G4	27	68	77	75	64
	F1	F6	F16	F17			F22	F23			F24	F26	F27	F28	F29	F30	W1	W2	W3	W4	W5
18.07.07	b	b									b	b			b	b	rb	rm	rm	<del>rm</del>	r
	G2	L1	L8	L6	L3	L4	L5	L8	G3	A1	A2	G1	G4	L3	L4	L6	27	68	77	75	64
	F1	F6	F16	F17	F22	F23	F24	F25	F26	F27	F28	F29	F30	F31	F32	F33	W1	W2	W3	W4	W5
19.07.07								b					tp	s	s	s					
	G2	L1					L5	L8	G3	A1	A2	G1	G4	L3	L4	L6	27	68	77	75	14
	F1	F6					F24	F25	F26	F27	F28	F29	F30	F31	F32	F33	W1	W2	W3	W4	W5
23.07.07																	rl	rl	rbml	rl	sml
	G2	L1					L5	L8	G3	A1	A2	G1	G4	L3	L4	L6	73	68	77	75	14
	F1	F6					F24	F25	F26	F27	F28	F29	F30	F31	F32	F33	W1	W2	W3	W4	W5
28.11.07	b	b					b	b	b	b	b	b	b	b	b	b	srml	rl	rl	rl	rl
	G2	L1	L5	L8	G3	A1	A2	G1	G4	L3	L4	L6				G4	73	68	77	75	14
	F1	F6	F24	F25	F26	F27	F28	F29	F30	F31	F32	F33				F39	W1	W2	W3	W4	W5
14.01.08	d															s					
	G2	L1	L5	L8	G3	A1	A2	G1	L3	L4	L6			G3	G4	G1	73	68	77	75	14
	F1	F6	F24	F25	F26	F27	F28	F29	F30	F31	F32	F33				F36	W1	W2	W3	W4	W5
15.01.08	d															s					
	G2	L1	L5	L8	A1	A2	L3	L4	L6		G3	A1	A2	G4	G1	L3	73	68	77	75	14
	F1	F6	F24	F25	F27	F28	F31	F32	F33		F36	F37	F38	F39	F40	F41	W1	W2	W3	W4	W5
16.01.08	d											s	s			s	rm	rm	rbm	rm	r
	G2	L1	L5	L8	L4	L6			L4	L8	G3	A1	A2	G4	G1	L3	73	68	77	75	14
	F1	F6	F24	F25	F32	F33			F34	F35	F36	F37	F38	F39	F40	F41	W1	W2	W3	W4	W5
17.01.08	d								s	s											
	G2	L1	L5	L6				L4	L8	G3	A1	A2	G4	G1	L3	L6	73	68	77	75	14
	F1	F6	F24	F33				F34	F35	F36	F37	F38	F39	F40	F41	F42	W1	W2	W3	W4	W5
21.01.08																s					
20.02.08e	bd	b	b					b	b	b	b	b	b	b	b	b	rb	r	r	rb	r
27.02.08g	b	b	b					b	b	b	b	b	b	b	b	b	rml	rml	rml	rml	rml
	G2	L1	L5					L4	L8	G3	A1	A2	G4	G1	L3	L6	73	68	77	75	88
	F1	F6	F24					F34	F35	F36	F37	F38	F39	F40	F41	F42	W1	W2	W3	W4	W5
09.04.08	bd	b	b					b	b	b	b	b	bd	bd	b	b	r	r	rb	r	r

	G2	L1	L5					L4	L8	G3	A1	A2	G4	G1	L3	L6	73	89	77	75	88
	F1	F6	F24					F34	F35	F36	F37	F38	F39	F40	F41	F42	W1	W2	W3	W4	W5
21.04.08																	rm	r	rm	rm	rm
06.05.08pp																					
	G2	L1	L5					L4	L8	G3	A1	A2	G4	G1	L3	L6	65	89	77	75	88
	F1	F6	F24					F34	F35	F36	F37	F38	F39	F40	F41	F42	W1	W2	W3	W4	W5
04.06.08	b	b	b					b	b	b	b	b	b	b	b	b	sl	r	r	r	r
13.08.08	E	E	E					E	E	E	E	E	E	E	E	E	E	E	E	E	E

Table A.1 Events related to instrument adjustments and other operations within the monitoring schedule.

## Appendix B: GPS coordinates of locations

Location	X (m)	Y (m)	Elevation (m)	Location	X (m)	Y (m)	Elevation (m)				
W	F1	3546536.91	5833007.61	35.09	N	F24	3546554.10	5833064.06	34.39		
	F2	3546531.68	5833022.26	35.04		F25	3546565.10	5833069.50	34.81		
	F3	3546520.57	5833018.03	35.05		F26	3546550.31	5833074.61	35.38		
	F4	3546518.12	5833025.38	35.07		F27	3546564.46	5833079.30	35.29		
	F7	3546525.00	5833004.11	34.77		F28	3546572.33	5833082.82	35.26		
	F8	3546518.95	5832978.74	34.87		F29	3546539.96	5833083.61	35.07		
	F9	3546514.92	5832993.31	34.74		F30	3546553.64	5833088.50	34.78		
	F10	3546510.46	5833007.18	34.86		F31	3546560.52	5833091.53	34.85		
	F11	3546508.64	5833014.51	34.86		F32	3546567.62	5833093.76	34.69		
	F12	3546506.13	5833021.74	35.30		F33	3546574.78	5833094.72	34.75		
	F13	3546504.19	5833029.41	34.53		F34	3546586.13	5833067.82	34.19		
	F14	3546501.61	5833036.50	34.44		F35	3546596.73	5833058.90	34.28		
	NW	F5	3546530.34	5833032.09		35.20	NE	F36	3546591.48	5833076.30	34.30
		F6	3546533.87	5833038.70		34.95		F37	3546604.14	5833069.28	34.13
F15		3546541	5833052.8	34.42	F38	3546610.65		5833065.75	33.98		
F16		3546545.9	5833058.8	34.24	F39	3546590.20		5833090.95	35.27		
F17		3546522.07	5833046.14	34.42	F40	3546603.40		5833083.82	35.08		
F18		3546529.90	5833057.85	34.65	F41	3546610.01		5833080.32	34.41		
F19		3546533.51	5833064.62	35.73	F42	3546617.16		5833076.38	34.12		
F20		3546507.55	5833043.92	34.37	Observation Well	W1		3546572.39	5833005.46	35.47	
F21		3546515.33	5833056.68	35.63		W2		3546522.12	5833026.46	35.50	
F22		3546518.97	5833063.38	35.48		W3		3546572.87	5833105.94	35.41	
F23	3546522.33	5833070.43	35.11	W4		3546585.70	5832927.06	34.64			
				W5		3546643.45	5833133.28	34.48			

Table B.1 Tiltmeter locations along 4 screen sections and observation wells.

loc.	A-A' Profile			B-B' Profile		
	X (354-)	Y (583-)	Elv.	X (354-)	Y (583-)	Elv.
1	6541.08	2944.13	34.24	6649.02	3088.02	34.53
2	6540.90	2945.18	34.24	6648.02	3087.85	35.14
3	6540.72	2946.10	34.40	6647.06	3087.54	35.42
4	6540.56	2947.11	34.32	6646.06	3087.31	35.42
5	6540.37	2948.09	34.26	6645.08	3087.09	35.53
6	6540.21	2949.07	34.34	6644.13	3086.83	35.55
7	6539.98	2950.01	34.39	6643.16	3086.58	35.65
8	6539.76	2951.02	34.25	6642.19	3086.34	35.67
9	6539.57	2951.99	34.26	6641.23	3086.13	35.78
10	6539.23	2952.96	34.42	6640.24	3085.88	35.73
11	6539.01	2955.92	34.41	6639.28	3085.61	35.68
12	6538.84	2956.91	34.32	6638.29	3085.38	35.61
13	6538.63	2957.92	34.34	6637.30	3085.15	35.46
14	6538.48	2958.87	34.40	6636.36	3084.88	35.35
15	6538.29	2959.87	34.47	6635.39	3084.62	35.22
16	6538.11	2960.83	34.49	6634.34	3084.43	35.16
17	6537.92	2961.80	34.53	6633.39	3084.08	35.01
18	6537.74	2962.79	34.53	6632.51	3083.88	34.89
19	6537.57	2963.80	34.59	6631.51	3083.62	34.80
20	6537.42	2964.76	34.58	6630.54	3083.39	34.66
21	6537.24	2965.76	34.46	6629.59	3083.15	34.57
22	6537.10	2966.74	34.58	6628.54	3082.83	34.51
23	6536.90	2967.72	34.68	6627.67	3082.59	34.51
24	6536.72	2968.70	34.75	6626.70	3082.28	34.43
25	6536.54	2969.69	34.67	6625.75	3082.12	34.42
26	6536.37	2970.65	34.63	6624.75	3081.84	34.37
27	6536.19	2971.63	34.57	6623.81	3081.62	34.39
28	6535.94	2972.63	34.64	6622.87	3081.37	34.32
29	6535.73	2973.60	34.78	6621.85	3081.16	34.35
30	6535.66	2974.58	34.90	6620.88	3080.89	34.31
31	6535.48	2975.58	34.84	6619.88	3080.66	34.33
32	6535.31	2976.55	34.83	6618.95	3080.42	34.29
33	6535.13	2977.53	35.01	6617.99	3080.18	34.38
34	6534.95	2978.49	35.00	6617.01	3079.92	34.32
35	6534.77	2979.49	35.03	6616.04	3079.63	34.23

loc.	A-A' Profile			B-B' Profile		
	X (354-)	Y (583-)	Elv.	X (354-)	Y (583-)	Elv.
36	6534.60	2980.47	34.92	6615.04	3079.36	34.29
37	6534.44	2981.43	34.84	6614.17	3079.14	34.24
38	6534.22	2982.43	34.78	6613.12	3078.95	34.38
39	6534.11	2983.37	34.94	6612.16	3078.61	34.34
40	6533.91	2984.41	34.98	6611.22	3078.42	34.29
41	6533.75	2985.37	34.93	6610.21	3078.16	34.27
42	6533.56	2986.32	34.92	6609.25	3077.85	34.32
43	6533.30	2987.29	34.94	6608.31	3077.66	34.22
44	6533.09	2988.30	34.84	6607.38	3077.39	34.21
45	6532.96	2989.24	34.78	6606.37	3077.17	34.32
46	6532.78	2990.23	34.93	6605.33	3076.87	34.25
47	6532.62	2991.21	34.92	6604.34	3076.61	34.26
48	6532.45	2992.17	34.83	6603.42	3076.32	34.22
49	6532.21	2993.21	34.90	6602.46	3076.09	34.24
50	6532.03	2994.20	34.83	6601.44	3075.85	34.18
51	6531.92	2995.17	34.93	6600.49	3075.59	34.26
52	6531.71	2996.13	34.86	6599.42	3075.35	34.15
53	6531.60	2997.09	34.97	6598.46	3075.15	34.18
54	6531.46	2998.07	34.94	6597.56	3074.87	34.18
55	6531.29	2999.13	34.80	6596.60	3074.63	34.24
56	6531.07	3000.12	34.78	6595.61	3074.42	34.24
57	6530.90	3001.07	34.73	6594.83	3073.98	34.24
58	6530.82	3002.06	34.79	6593.82	3073.71	34.22
59	6530.69	3003.02	34.87	6592.83	3073.47	34.17
60	6530.58	3004.01	34.96	6591.87	3073.25	34.19
61	6530.49	3005.02	34.97	6590.91	3073.04	34.22
62	6530.40	3005.99	35.00	6589.93	3072.73	34.23
63	6530.19	3006.94	34.95	6588.94	3072.50	34.15
64	6529.93	3007.96	34.79	6587.98	3072.26	34.19
65	6529.78	3008.95	34.59	6587.05	3072.03	34.17
66	6529.64	3009.90	34.48	6586.00	3071.78	34.28
67	6529.46	3010.88	34.42	6585.06	3071.51	34.49
68	6529.33	3011.87	34.39	6584.07	3071.26	34.44
69	6529.19	3012.83	34.45	6583.12	3071.02	34.48
70	6529.02	3013.83	34.44	6582.16	3070.79	34.59

loc.	A-A' Profile			B-B' Profile		
	X (354-)	Y (583-)	Elv.	X (354-)	Y (583-)	Elv.
71	6528.78	3014.80	34.48	6581.23	3070.52	34.54
72	6528.63	3015.78	34.56	6580.20	3070.31	34.56
73	6528.49	3016.76	34.74	6579.23	3070.07	34.56
74	6528.35	3017.71	34.92	6578.23	3069.80	34.52
75	6528.18	3018.67	35.09	6577.28	3069.59	34.58
76	6527.95	3019.66	35.06	6576.35	3069.31	34.65
77	6527.73	3020.63	35.07	6575.40	3069.12	34.70
78	6527.49	3021.63	35.03	6574.44	3068.88	34.79
79	6527.29	3022.59	35.00	6573.44	3068.62	34.82
80	6527.16	3023.56	34.94	6572.47	3068.38	34.84
81	6527.00	3024.48	34.94	6571.53	3068.11	34.83
82	6526.82	3025.50	35.01	6570.50	3067.93	34.81
83	6526.56	3026.49	35.03	6569.55	3067.70	34.83
84	6526.45	3027.49	35.05	6568.57	3067.47	34.90
85	6526.26	3028.46	35.17	6567.60	3067.24	34.89
86	6526.07	3029.46	35.31	6566.62	3066.97	34.71
87	6525.84	3030.40	35.32	6565.65	3066.69	34.48
88	6525.69	3031.40	35.30	6564.67	3066.44	34.38
89	6525.48	3032.37	35.26	6563.69	3066.25	34.33
90	6525.28	3033.35	35.28	6562.75	3065.98	34.36
91	6525.16	3034.35	35.21	6561.75	3065.71	34.35
92	6525.00	3035.32	35.08	6560.85	3065.48	34.40
93	6524.88	3036.33	35.10	6559.91	3065.25	34.47
94	6524.73	3037.29	35.11	6558.94	3064.99	34.44
95	6524.58	3038.28	35.15	6557.97	3064.75	34.43
96	6524.52	3039.33	35.12	6556.95	3064.52	34.37
97	6524.35	3040.22	35.00	6556.01	3064.29	34.39
98	6524.17	3041.18	34.98	6555.04	3064.04	34.34
99	6524.01	3042.19	35.19	6554.09	3063.83	34.39
100	6523.84	3043.19	35.42	6553.08	3063.61	34.37
101	6523.68	3044.18	35.29	6552.12	3063.30	34.35
102	6523.48	3045.09	34.94	6551.15	3063.13	34.37
103	6523.32	3046.11	34.57	6550.17	3062.91	34.38
104	6523.12	3047.07	34.36	6549.19	3062.66	34.35
105	6522.85	3048.07	34.26	6548.24	3062.44	34.40

loc.	A-A' Profile			B-B' Profile		
	X (354-)	Y (583-)	Elv.	X (354-)	Y (583-)	Elv.
106	6522.68	3049.02	34.22	6547.25	3062.14	34.42
107	6522.55	3050.00	34.31	6546.31	3061.94	34.42
108	6522.42	3050.99	34.29	6545.34	3061.68	34.45
109	6522.27	3051.97	34.29	6544.33	3061.41	34.47
110	6522.10	3052.97	34.30	6543.36	3061.15	34.48
111	6522.05	3053.96	34.37	6542.41	3060.89	34.52
112	6521.89	3054.94	34.57	6541.43	3060.69	34.37
113	6521.74	3055.91	34.80	6540.46	3060.48	34.40
114	6521.57	3056.82	35.11	6539.48	3060.19	34.43
115	6521.40	3057.80	35.35	6538.56	3059.96	34.44
116	6521.20	3058.72	35.60	6537.58	3059.70	34.43
117	6521.04	3059.70	35.82	6536.61	3059.49	34.57
118	6520.82	3060.69	35.72	6535.60	3059.24	34.58
119	6520.62	3061.62	35.59	6534.59	3058.99	34.58
120	6520.38	3062.62	35.53	6533.58	3058.75	34.58
121	6520.16	3063.59	35.51	6532.58	3058.54	34.63
122	6519.94	3064.57	35.41	6531.63	3058.28	34.67
123	6519.76	3065.54	35.35	6530.64	3057.98	34.64
124	6519.58	3066.53	35.36	6529.66	3057.88	34.65
125	6519.42	3067.51	35.28	6528.70	3057.55	34.73
126	6519.13	3068.46	35.20	6527.76	3057.31	34.66
127	6518.99	3069.49	35.09	6526.77	3057.04	34.60
128	6518.88	3070.51	35.14	6525.82	3056.84	34.71
129	6518.62	3071.48	35.07	6524.86	3056.56	34.59
130	6518.46	3072.51	35.08	6523.88	3056.31	34.65
131	6518.27	3073.44	35.09	6522.88	3056.06	34.76
132	6518.13	3074.39	35.19	6521.94	3055.84	34.82
133	6517.92	3075.40	35.20	6521.01	3055.61	34.79
134	6517.76	3076.39	35.11	6520.00	3055.38	34.79
135	6517.68	3077.36	35.13	6519.02	3055.13	34.91
136	6517.57	3078.32	35.07	6518.07	3054.86	34.95
137	6517.45	3079.32	35.12	6517.11	3054.60	34.94
138	6517.29	3080.28	35.09	6516.14	3054.40	34.86
139	6517.13	3081.29	35.20	6515.15	3054.12	34.91
140	6517.04	3082.25	35.01	6514.21	3053.84	34.89



		A-A' Profile			B-B' Profile		
loc.	X (354-)	Y (583-)	Elv.	X (354-)	Y (583-)	Elv.	
141	6516.88	3083.27	35.10	6513.24	3053.56	34.84	
142	6516.70	3084.32	35.08	6512.25	3053.35	34.94	
143	6516.63	3085.23	35.11	6511.30	3053.12	34.94	
144	6516.32	3086.24	35.10	6510.30	3052.87	34.98	
145	6516.45	3087.26	35.12	6509.29	3052.64	35.07	
146	6516.25	3088.18	35.00	6508.33	3052.42	35.19	
147	6516.13	3089.20	34.97	6507.37	3052.17	35.23	
148	6515.96	3090.17	35.02	6506.43	3051.95	35.25	

		A-A' Profile			B-B' Profile		
loc.	X (354-)	Y (583-)	Elv.	X (354-)	Y (583-)	Elv.	
149	6515.80	3091.17	35.01	6505.46	3051.69	35.31	
150	6515.78	3092.14	35.03	6504.45	3051.44	35.33	
151	6515.58	3093.11	34.87	6503.50	3051.15	35.39	
152	6515.40	3094.07	35.10	6502.55	3050.88	35.42	
153	6515.28	3095.17	35.03	6501.64	3050.65	35.35	
154	6515.26	3096.05	35.05	6500.64	3050.39	35.46	
155	6515.22	3097.07	34.95	6499.69	3050.17	35.29	
156				6498.81	3049.93	35.04	

Table B.2 Coordinates of profile points along transects A-A' and B-B' of additional geophysical surveys.

### Appendix C: Additional P-wave seismic survey

To verify the existence of lateral heterogeneities, a P-wave seismic survey has been applied on transect B-B' (as in Fig. 3.7). The specific parameters, the processing flow, and the seismogram are shown in Table C.1, Table C.2, and Fig. C.1. Strong continuous reflection signals are seen between the depth of 5 m and 10 m. This possibly indicates the presence of the water table. A steep angle zone of disrupted reflections appearing at a distance of 120 m is probably due to static problems. However, another sharp discontinuity inclining from profile distance 100 m to 45 m at depths from 15 m to 30 m gives evidence of inhomogeneous conditions at this depth.

Recording system	Geometrics Geode
Receiver type	Single geophones SM6 100 Hz
Number of recording stations	145
Number of blows	152
Geophone spacing	1 m
Shot spacing	1 m
Line length	155 m
Source type	Sledgehammer, 1kg, 4 times of stacking
Record length	500 ms
Number of recording channels	72
Sample rate	0.25 ms
CMP spacing	0.5 m

Table C.1 Specific parameters for P-wave reflection survey.

Processing step	Purpose
Geometry editing	Definition of locations for subsequent calculations
Vertical stack	Enhancement of signal-to-noise ratio
Geometry information copying into seismic data header	Data arrangement by reflection point
Refraction statics calculating	Static corrections for the transect
Band pass filtering	Enhancement of signal energy
Stacking velocity picking	Determination of stacking velocity
Normal moveout with stacking velocity and stack	Reflectors flattened for stacking and noise reduction
Depth conversion	Convert vertical axis from time to depth
Setting of the data to final datum	Elevation modification to in-situ condition

Table C.2 Processing flow for P-wave data.

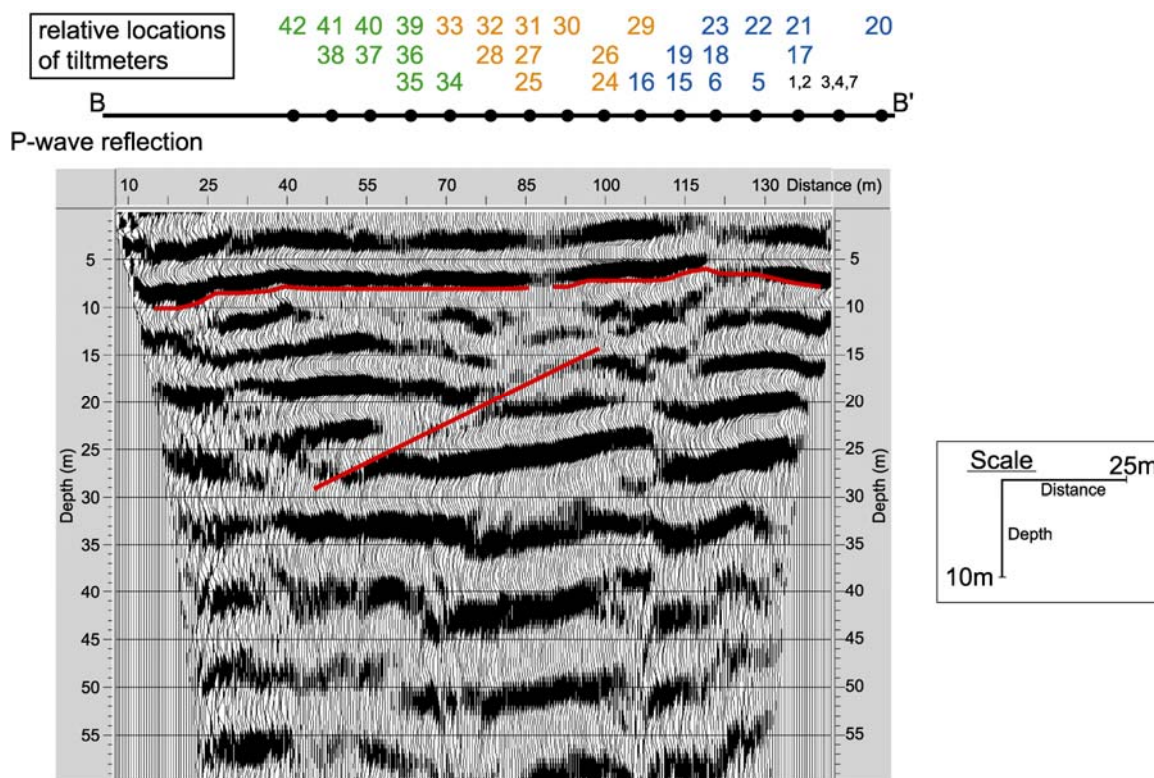


Fig. C.1 The seismogram of P-wave reflection survey.

## Appendix D: General migrating signals and hodograms at locations along NE flank

The general migrating tilt signals (X-, Y-axis and instrument temperature) from locations F34 to F42 (NE flank), the reference location F1 (W flank), F6 (NW flank), and F24 (N flank) are seen in Fig. D.1. Numbers to the left of the diagrams indicate full range in  $\mu\text{rad}$  or  $^{\circ}\text{C}$  (as in Fig. 4.2). The spikes in the 1<sup>st</sup> shaded zone are the signals induced by the additional pump tests. Because pumped water was mostly discharged to the ground surface near the location F1, frequent spike-like signals are seen in X- and Y-axis at F1. A ladder-like signal as seen at F24 was also induced by water discharge but the influence was much stronger and caused larger deviations in tilt signals and even in instrument temperature. The spikes in the 2<sup>nd</sup> shaded zone (of TX and TY) indicate an earthquake event (M = 8.0 at Sichuan, China). Spikes in the 3<sup>rd</sup> shaded zone are of a meteorological origin.

The hodograms displaying the overall drifting variations are shown (Fig. D.2). The scale bar for all locations is 250  $\mu\text{rad}$  for both X- and Y-axis (as in Fig. 4.4) except for location F24 (500  $\mu\text{rad}$ ). The sequence of monitoring months, the amplitude and the orientation of the migrating signals are shown. Most orientations are in the NW-SE direction. Variations in tilt amplitude are smaller than 10  $\mu\text{rad}/\text{month}$ .

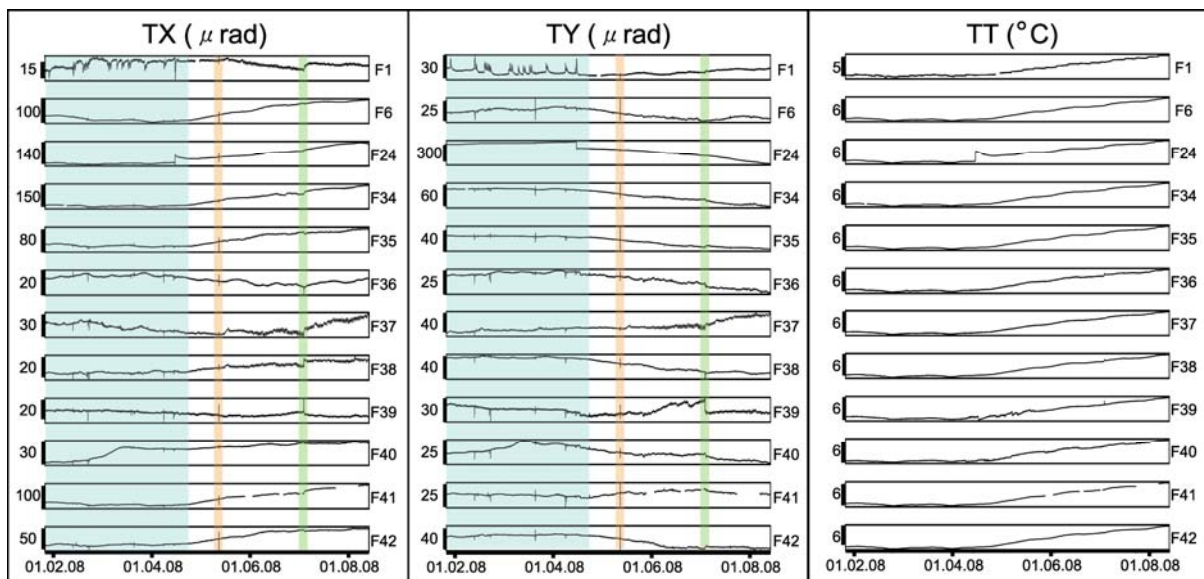


Fig. D.1 The general migrating tilt signals (X-, Y-axis and instrument temperature) at F1, F6, F24, and F34-F42

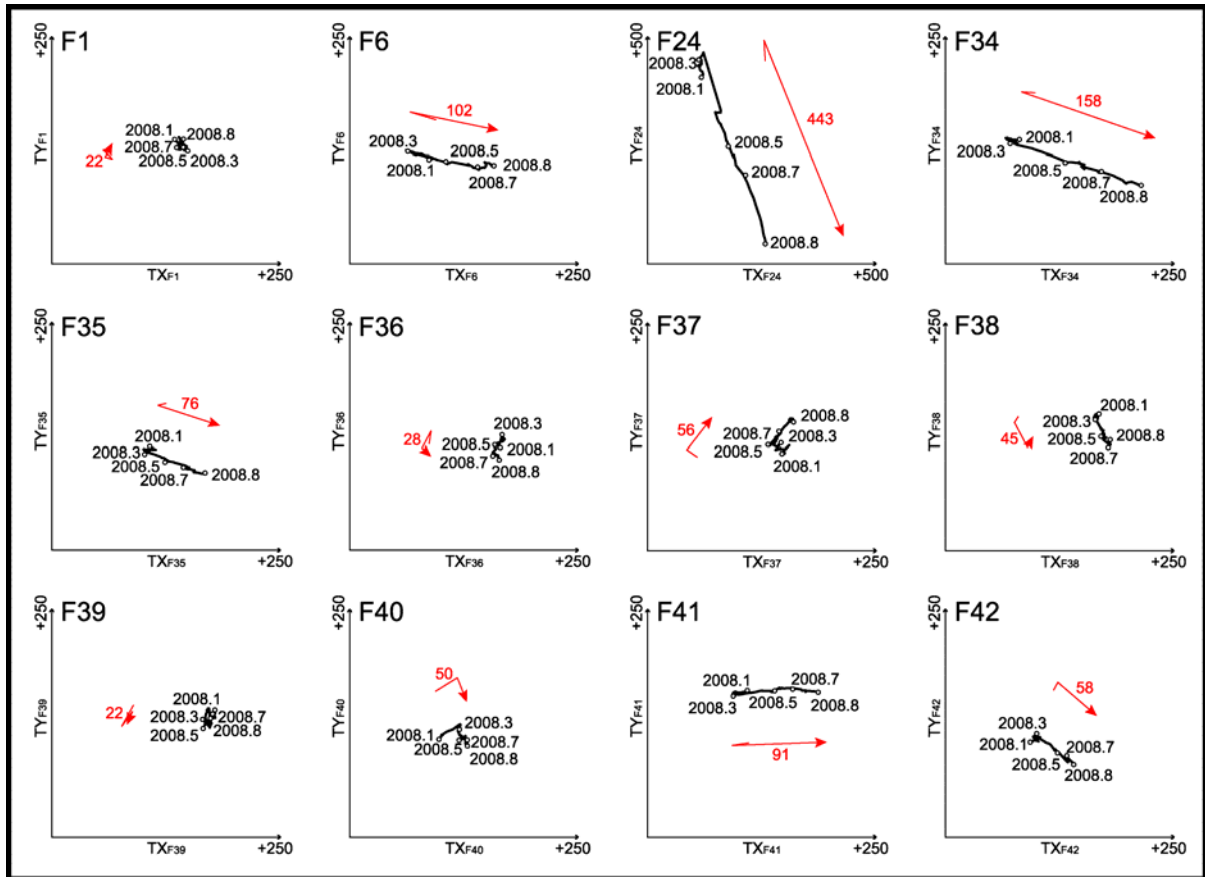


Fig. D.2 The tilt hodograms for locations F1, F6, F24, and F34-F42.

## Appendix E: Water table level after April 2008

Figure E.1 shows the supplementary data of water table level from 5 observation wells (W1-W5) continuing the time sequences in Fig. 4.5. The average water table level was reduced to an average of 29.75 m above sea level after regular pumping in the central pit was reactivated. Results from the 5 observation wells exhibit a consistent trend.

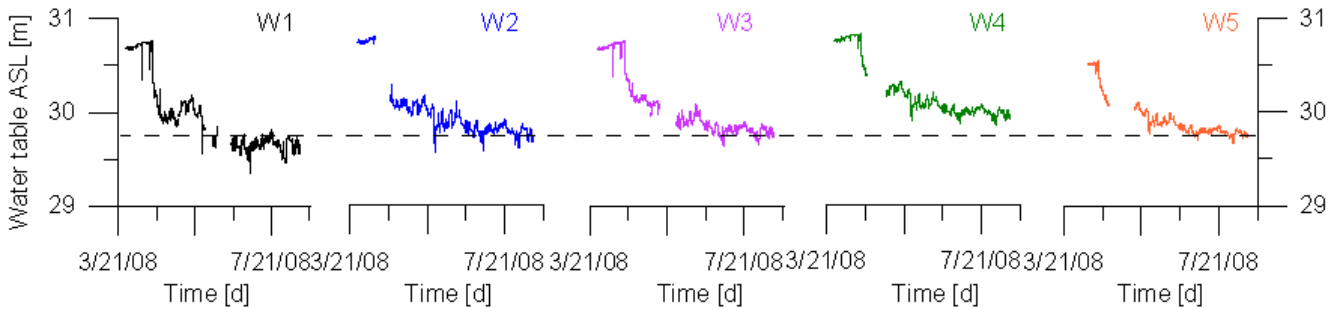


Fig. E.1 Changes in water table level from 5 observation wells for period 1 April till 13 August 2008.

## Appendix F: When the central pit is not considered for model (d)

When the influence of the central pit is eliminated in model (d) (as in Section 6.2.1), induced pore pressure and tilt signals plot as given for plane at  $z = 10$  m near steady status (3600 s) in Fig. F.1 (to be compared with Fig. 5.9). The pore pressure decreases from the screen section to the boundary area, and also with increasing radial distance from the screen section. The maximum tilt occurs at ca. 60 m radial distance and decreases on either side. Besides, the tilt amplitudes decrease from the boundary area (small circle-like pattern) to the screen sections.

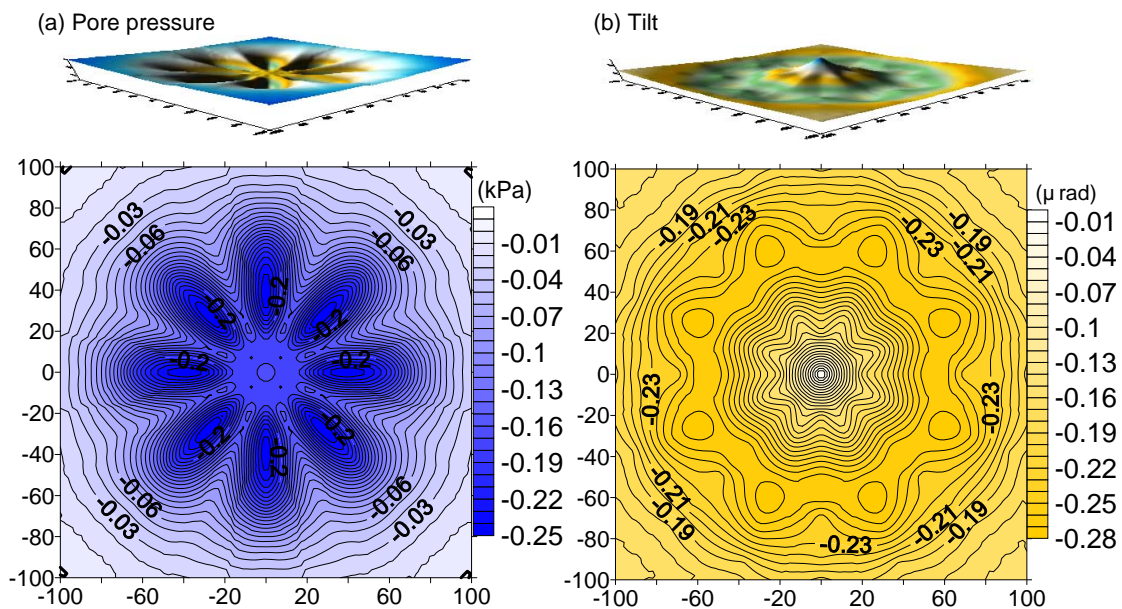


Fig. F.1 Computational results of (a) pore pressure and (b) tilt from the screen sections and boundary area (at depth  $z = 10$  m and 3600 s after onset of pumping) on X-Y and X-Z planes without considering the influence of the central pit.



## Erklärung zur Dissertation

Hierdurch erkläre ich, dass die Dissertation Pump induced tilt and pore pressure variations at Fuhrberg, north of Hanover and their modeling in layered half space

selbstständig verfasst und alle benutzten Hilfsmittel sowie evtl. zur Hilfeleistung herangezogene Institutionen vollständig angegeben wurden.

Die Dissertation wurde nicht schon als Diplom- oder ähnliche Prüfungsarbeit verwendet.

Hannover, den

29.12'08  


---

(Unterschrift)

Name: Hsiao-Chih Chen





# Acknowledgements

I'm very fortunate to have Professor Kümpel to be my supervisor. As my mentor, he is always patient, encouraging and inspiring. I'm deeply grateful for everything he has taught me and for giving me the chance to be educated at the GGA institute.

I'm honored to have Professor Winsemann and Professor Yaramanci as my committee members. It's very kind of them to find time from the tight schedule and to offer helpful advice for my thesis.

Many thanks to the colleagues from S1 group of the GGA institute. You've provided a comfortable working atmosphere and for your generous support: Prof. Krawczyk, it's a pleasure to work under you; Detlef Vogel for GPS measurement; Hermann Bunes, Thies Beilecke, Stefan Cramm, Walter Rode and Eckhardt Grossmann for providing excellent seismic measurement resources. For help with DC resistivity and GPR measurement, thanks go to Regine Ziekur, Michael Grinat, Wolfgang Südekum and Thomas Grelle from S2 who are always generous with help and advice. Of course, special thanks go to Haifa and Sigi. You've accompanied me through three memorable years with fun, laughter, and especially for your sincere opinions and immense support. I'd also like to thank Dr. Wang from GFZ and Dr. Fabian from Bremen University for helpful discussions and Hanover waterworks for their cooperation.

Last, to John, thanks for standing by me through the difficult times and for my emotional support. And to my dearest family in Taiwan, thanks for your understanding and being supportive for my study. Without you, the thesis can not be completed successfully!!!

在此, 感謝每一位幫助我與支持我的朋友, 您們的溫情我將永遠謹記在心!!!



# Curriculum Vitae

## **Personal particular**

Name                    Hsiao-Chih Chen  
Date of Birth         31<sup>st</sup> December, 1978  
Nationality           Taiwanese

## **Education and scientific experience**

- 2005-2008     PhD study, Geosciences, Leibniz Universität Hannover / GGA Institute
- 2003-2005     Research Assistant, Geosciences, National Taiwan University
- 2002             M.Sc., Geosciences, National Taiwan University
- 2000             B.Sc., Geosciences, National Taiwan University

## **Awards**

- 2005-2008     DAAD-Leibniz Scholarship
- 2002             Geology Youth Forum Award
- Fall 2001       Sinotech Engineering Consultants, Inc. Scholarship
- Spring 2001    Sinotech Engineering Consultants, Inc. Scholarship
- 1999             National Taiwan University President Award

## **Publications**

- 2008 H. Rifai, S. Grüneberg, H. C. Chen, H.-J. Kümpel, Einsatz von Neigungsmessern in Schwarmstedt (2. Teil). Project report, GGA.
- 2008 H. C. Chen, S. Grüneberg, H. Rifai, H.-J. Kümpel, Monitoring near surface movements and recognizing hydrological characteristics induced by an asteriated distributed pump well in Fuhrberger Feld, Lower Saxony: *Annual Meeting Geophysical Society of Germany (Deutschen Geophysikalischen Gesellschaft)*, p.140.
- 2007 H. Rifai, S. Grüneberg, H. C. Chen, H.-J. Kümpel, Einsatz von Neigungsmessern in Schwarmstedt. Project report, GGA.
- 2004 H. C Chen and S. R. Song, On-site measurements of TCDP, *Rock deformation, Gordon Research Conferences*.
- 2002 H. C. Chen, The study of the engineering properties and the slope stability of the lava flow in Kuishanhu, Chinshan area of Taipei County. Master thesis, Geosciences Dept., National Taiwan University.
- 2002 H. C. Chen and Hongey Chen, The study case of the slope failure in Kuishanhu, Chinshan area of Taipei County and the relevant engineering properties of the lava flow: *Annual Meeting Geological Society of China*, p.350-352.
- 2002 H. C. Chen and Hongey Chen, The engineering properties of the lava flow and its slope stability in Kuishanhu, Chinshan area of Taipei County.: *4th Geology Forum of Young Geoscientists*, p.22-24.

